UNIVERSIDAD CARLOS III DE MADRID

MASTER THESIS

# Computational Aspects of Sensor Fusion for GNSS Outlier Mitigation in Navigation

*Author:*
Daniel ARIAS MEDINA

*Supervisors:*
Jesús GARCIA HERRERO,
Ralf ZIEBOLD

*A thesis submitted in fulfillment of the requirements*
*for the degree of Master in Computer Science and Technology*

*in the*

Nautical Systems Department, Institute of Communication and Navigation
German Aerospace Center (DLR)

February 5, 2016


Universidad
Carlos III de Madrid

# Declaration of Authorship

I, Daniel ARIAS MEDINA, declare that this thesis titled, "Computational Aspects of Sensor Fusion for GNSS Outlier Mitigation in Navigation" and the work presented in it are my own. I confirm that:

- This work was done wholly or mainly while in candidature for a research degree at this University.
- Where any part of this thesis has previously been submitted for a degree or any other qualification at this University or any other institution, this has been clearly stated.
- Where I have consulted the published work of others, this is always clearly attributed.
- Where I have quoted from the work of others, the source is always given. With the exception of such quotations, this thesis is entirely my own work.
- I have acknowledged all main sources of help.
- Where the thesis is based on work done by myself jointly with others, I have made clear exactly what was done by others and what I have contributed myself.

Signed:

Date:

# *Abstract*

As the Global Navigation Satellite Systems (GNSS) are intensively used as main source of Position, Navigation and Timing (PNT) information for maritime and inland water navigation, it becomes increasingly important to ensure the reliability of GNSS-based navigation solutions for challenging environments. Although an intensive work has been done in developing GNSS Receiver Autonomous Integrity Monitoring (RAIM) algorithms, a reliable procedure to mitigate multiple simultaneous outliers is still lacking.

The presented work evaluates the performance of several methods for multiple outlier mitigation based on robust estimation framework and compares them to the performance of state-of-the-art methods. The relevant methods include M-estimation, S-estimation, Least Median of Squares LMS-based approaches as well as corresponding modifications for C/N0-based weighting schemes. The snapshot positioning methods are also tested within the quaternion-based Unscented Kalman filter for integrated inertial/GNSS solution.

The proposed schemes are evaluated using real measurement data from challenging inland water scenarios with multiple bridges and a waterway lock. The initial results are encouraging and clearly indicate the potential of the discussed methods both for classical snapshot solutions as well for the methods with complementary sensors.

*Keywords - Integrated Navigation Systems; Robust Estimation; Global Navigation Satellite System GNSS; Kalman Filtering; Inertial Sensing.*

# *Resumen*

A medida que el Sistema Global de Navegación por Satélite se ha convertido en fuente principal de información para la posición, navegación y temporarización en aplicaciones marítimas y continentales, se vuelve cada vez más importante garantizar la fiabilidad de la navegación en entornos más exigentes. A pesar del empeño puesto por la la comunidad científica en el desarrollo de algoritmos para la Monitorización de la Integridad en la localización, aún se carece de un sistema que permite mitigar el efecto de múltiples señales erróneas simultáneamente.

Este trabajo evalúa el funcionamiento de numerosos métodos, catalogados como robustos, frente a la presencia de señales de los satélites con grandes errores, y compara su rendimiento frente a los algoritmos del Estado del Arte. Entre los métodos presentados se encuentran los estimadores M, S y LMS. Además, estos métodos se modificarán para incluir información de la intensidad de las señales recibidas. Todas estas técnicas carecen de memoria, empleando únicamente la información de los satélites recibida en ese preciso instante. Para paliar esta falta de memoria, la navegación por satélite se combinará con navegación inercial por medio de un Filtro de Kalman.

Los métodos desarrollados han sido evaluados en campañas de medición reales, con escenarios en los que las señales de los satélites se encontraban severamente afectadas por su reflexión en estructuras. Los resultados obtenidos son alentadores, e indican que hay claramente un gran potencial en la aplicación de estimación robusta en la navegación por satélite.

*Palabras clave - Sistemas de Navegación Integrada; Estimación Robusta; Sistema Global de Navegación por Satélite; Filtro de Kalman; Sistemas inerciales.*

# *Acknowledgements*

This work would not have been possible without the support and guidance of several individuals who, one way or another, contributed and assisted me through the preparation and accomplishment of this study.
Firstly, I would sincerely express my gratitude to the Nautical Systems Department, Institute of Communication and Navigation, German Aerospace Center (DLR) for trusting in my skills and grant me all the support and expertise I would need in the development of this work.
Besides, I thank my colleagues Dr. Frank Heymann, M.Sc. Iván Herrera-Pinzón, M.Sc. Gregor Siegert and the rest of DLR colleagues for the stimulating discussions and weekly meetings.
I would like to thank Dr. Ralf Ziebold and Prof. Dr. Jesús Herrero García for their steady support and guidance to complete this study.
I owe my utmost acknowledgement to M.Sc. Michailas Romanovas for devoting all his patience and encouragement, as well as joining me for innumerable coffees during my stay in DLR.
Finally, I thank my friends and family for cheering and relieving me throughout my experience in Germany.

# Contents

# List of Figures

# List of Tables

# List of Abbreviations

| | |
|---|---|
| **CDF** | Cumulative Distribution Function |
| **CN0** | Carrier-to-noise ratio |
| **DLR** | German Aerospace Center |
| **DOP** | Dilution of Precision |
| **DOY** | Day Of Year |
| **DVL** | Doppler Velocity Log |
| **ECEF** | Earth-Centered Earth-Fixed Coordinate System |
| **ECI** | Earth-Centered Inertial Coordinate System |
| **EKF** | Extended Kalman Filter |
| **FOG** | Fiber Optic Gyro |
| **GA** | Ground Antennas |
| **GDOP** | Geometric Dilution of Precision |
| **GLONASS** | Global Navigation Satellite System |
| **GNSS** | Global Navigation Satellite Systems |
| **GPS** | Global Positioning System |
| **HDOP** | Horizontal Dilution of Precision |
| **HPE** | Horizontal Position Error |
| **IMO** | International Maritime Organization |
| **IMU** | Inertial Measurement Unit |
| **INS** | Inertial Navigation System |
| **IRLS** | Iteratively Reweighted Least Squares |
| **KF** | Kalman Filter |
| **LC** | Loosely Coupled |
| **LKF** | Linear Kalman Filter |
| **LMS** | Least Median of Squares |
| **LOS** | Line-of-sight |
| **LS** | Least Squares |
| **LTS** | Least Trimmed Squares |
| **MAD** | Median Absolute Deviation |
| **MCS** | Master Control Station |
| **MEMS** | Micro-Electro-Mechanical Systems |
| **MMM** | Multi-constellation, Multi-frequency, Multi-antenna |
| **MS** | Monitoring Stations |
| **NED** | North-East-Down Coordinate System |
| **NLOS** | Non-line-of-sight |
| **PDOP** | Position Dilution of Precision |
| **PNTI** | Positioning, Navigation, Timing and Integrity |
| **PNT** | Positioning, Navigation and Timing |
| **PPP** | Precise Point Positioning |

| | |
|---|---|
| **PRN** | Pseudorange |
| **PVT** | Position, Velocity and Timing |
| **RBE** | Recursive Bayesian Estimation |
| **RAIM** | Receiver Autonomous Integrity Monitoring |
| **RANSAC** | Random Sample Consensus |
| **RANCO** | Range Consensus |
| **RMSE** | Root Mean Square Error |
| **RMS** | Root Mean Square |
| **RR** | Pseudorange Rate |
| **RTK** | Real Time Kinematics |
| **SBAS** | Satellite-Based Augmentation Systems |
| **SPP** | Single Point Positioning |
| **SRN** | Signal-to-noise ratio |
| **TC** | Tightly Coupled |
| **TDOP** | Time Dilution of Precision |
| **TOA** | Time Of Arrival |
| **UKF** | Unscented Kalman Filter |
| **UTC** | Coordinated Universal Time |
| **VDOP** | Vertical Dilution of Precision |
| **WLS** | Weighted Least Squares |
| **WSSE** | Weighted Sum of the Squared Errors |

# Lista de Acrónimos

| | |
|---|---|
| **CDF** | Función de Distribución Acumulada |
| **CN0** | Ratio Ruido al Portador |
| **DLR** | Agencia Aeroespacial Alemana |
| **DOP** | Dilución de la Precisión |
| **DOY** | Día del Año |
| **DVL** | Log de la Velocidad |
| **ECEF** | Sistema de Coordenadas Centrado y Sujeto a la Tierra |
| **ECI** | Sistema de Coordenadas Inercial Centrado en la Tierra |
| **EKF** | Filtro de Kalman Extendido |
| **FOG** | Giroscopio de Fibra Óptica |
| **GA** | Antenas en Tierra |
| **GDOP** | Dilución de la Precisión Geométrica |
| **GLONASS** | Global Navigation Satellite System |
| **GNSS** | Sistema Global de Navegación por Satélite (diseñado por Rusia) |
| **GPS** | Sistema Global de Navegación por Satélite |
| **HDOP** | Dilución de la Precisión Horizontal |
| **HPE** | Error en la Posición Horizontal |
| **IMO** | Organización Marítima Internacional |
| **IMU** | Unidad de Medición Inercial |
| **INS** | Sistema de Navegación Inercial |
| **IRLS** | Mínimos Cuadrados Iterativamente Ponderados |
| **KF** | Filtro de Kalman |
| **LC** | Holgadamente Anexo |
| **LKF** | Filtro de Kalman Lineal |
| **LMS** | Mínimos Cuadrados Promedio |
| **LOS** | En línea de visión |
| **LS** | Mínimos Cuadrados |
| **LTS** | Mínimos Cuadrados Ajustados |
| **MAD** | Deviación Absoluta de la Mediana |
| **MCS** | Estación de Control Maestra |
| **MEMS** | Sistemas Electromecánicos |
| **MMM** | Multi-constelación, Multi-frecuencia, Multi-antena |
| **MS** | Estaciones de Control |
| **NED** | Sistema de Coordenadas Norte-Este-Abajo |
| **NLOS** | Sin línea de visión |
| **PDOP** | Dilución de la Precisión de la Posición |
| **PNTI** | Localización, Navegación, Temporización e Integridad |
| **PNT** | Localización, Navegación y Temporización |
| **PPP** | Localización Precisa |

| | |
|---|---|
| **PRN** | Pseudorango |
| **PVT** | Localización, Velocidad y Temporarización |
| **RBE** | Estimación Recursiva Bayesiana |
| **RAIM** | Monitorización de la Integridad Autónoma por el Receptor |
| **RANSAC** | Consenso Muestra Aleatoria |
| **RANCO** | Consenso en el Rango |
| **RMSE** | Raíz Cuadrada del Error Cuadrático Medio |
| **RMS** | Valor Cuadrático medio |
| **RR** | Velocidad del Pseudorango |
| **RTK** | Cinemática en Tiempo Real |
| **SBAS** | Sistema de Aumento Basado en Satélite |
| **SPP** | Localización Sencilla |
| **SRN** | Relación Señal/Ruido |
| **TC** | Estrechamente Anexo |
| **TDOP** | Dilución de la Precisión de la Temporarización |
| **TOA** | Tiempo de Llegada |
| **UKF** | Filtro de Kalman Unscented |
| **UTC** | Tiempo Universal Coordinado |
| **VDOP** | Dilución de la Precisión de la Vertical |
| **WLS** | Mínimos Cuadrados Ponderados |
| **WSSE** | Suma Ponderada de los Errores al Cuadrado |

Chapter 1

# Introduction

Global Navigation Satellite Systems (GNSS) are the cornerstone and the main information source for Positioning, Navigation and Timing (PNT) data in maritime and inland water navigation systems. However, the performance of the system can be disturbed due to space weather events, multipath, jamming or overall system failures. The International Maritime Organization (IMO) has stated that resilient PNT is essential for safer and more efficient shipping and the European Commission has defined the carriage of goods through inland waterways as climate-friendly and energy-efficient mean of transportation, encouraging more companies to make use of this mode of transport. However, this proposal results in far more challenging scenarios when compared to maritime applications, making redundant and complementary information for different sensors indispensable to bridge possible GNSS outages and compensate for the presence of multipath and non-line-of-sight (NLOS) signals.

Every year, there is a large amount of marine accidents and casualties. According to the statistical summary of the Transportation Safety Board of Canada, more than 300 accidents were reported during the last year for vessels registered in this country. In a report released by the Baltic Marine Environment Protection Commission [40], more than 50% of the marine accidents are caused by navigation causes - inaccurate nautical data, misinterpretation of navigational data or incomplete situation awareness among others -. This is a clear indicator that the navigation for maritime applications needs to be improved in terms of accuracy and detection of failures for the navigation solution.

The classical code-based positioning using an iterated Least Squares (LS) method lacks robustness as even a single outlier can introduce a gross error in the final position solution. This issue becomes even more prominent as high sensitivity receivers are increasingly used to ensure sufficient GNSS availability. To address this problem, several approaches have been proposed. Classical Receiver Autonomous Integrity Monitoring (RAIM) techniques have been designed to perform fault detection and exclusion. The RAIM procedures are usually based on a single fault assumption and still could fail when there are multiple simultaneous outliers [68]. Although modifications have been suggested to reject multiple failures sequentially, the methods could fail due to correlations in test statistics and lead to wrong identification of the outliers.

The robust estimation methods provide an alternative view to the problem of multiple GNSS faults. Although some authors have already applied robust regression methods to improve the performance of GNSS positioning in non-favorable environments, a systematic review and comparison of robust methods for positioning applications is still missing. Most of the authors have compared separate robust schemes against classical LS positioning, but not against competing robust methods. A few comparisons of robust methods were performed (e.g., [26]), but only simulated data have been used. This work addresses a weak

point of the related by using real measurement data from a challenging highly dynamical scenario, where not artificially induced outliers of known statistics are applied, but real faults caused by true multipath effects and NLOS signals.

The developed schemes are evaluated using a challenging inland waterways scenario with several bridges and a waterway lock. An importance of this scenario has been noticed as an evaluation of accidents involving vessels reveals that there is still a rather significant number of bridge collisions (approximately 20-30 per year) which result both in heavy damage to the vessel and potential injuries to the persons onboard the vessel [18]. Furthermore, such collisions could also damage light bridge structures and have a tremendous effect for inland water traffic due to a ban of shipping along the river for a longer period of time. Moreover, due to multipath and NLOS effects, similar scenarios result in extremely challenging conditions for a pure GNSS-based navigation and can be effectively used to benchmark the performance of GNSS-based positioning.

In order to increase the reliability of the PNT solution, it is indispensable to integrate additional sensors whose error patterns are independent from those of GNSS. A typical complementary sensing modality is the inertial sensing. These sensors are immune to jamming and can track fast and subtle motion and are able to bridge short GNSS outages and smooth the noise of code-based GNSS solutions. The information from the Inertial Measurement Unit (IMU) and the GNSS receiver can be integrated synergistically by combining an excellent short term performance of the IMU and long term stability of the GNSS solution within the hybrid navigation system. The presented work assesses the impact of the proposed robust positioning schemes in integrated navigation solutions by fusing the output of the robust GNSS positioning with the data from the onboard IMU employing an Unscented Kalman Filter (UKF) with quaternion attitude parametrization.

## 1.1 Objectives

The aim of this thesis is to study and improve the performance of different approaches to automatically detect, mitigate and exclude the effects of faulty GNSS signals, responsible for large errors in the position estimation. This work is composed by the following tasks:

1. Systematic evaluation of the most promising techniques for outlier detection, including novelty methods in RANdom SAmple Consensus (RANSAC) and recent advances on Recursive Bayesian Estimation (RBE).

2. Address snapshot (memoryless) techniques for robust positioning.

3. Integration of the robust techniques in a system which fuses satellite and inertial-based navigation.

4. Test of the performance of the developed algorithms on challenging scenarios presenting multiple simultaneous outliers, using real data.

The development of this work has been financed and supported by the department of Nautical Systems, which is part of the Institute of Communication and Navigation of the German Aerospace Center (DLR) for a period of seven months. The initial schedule established in order to fulfil all the proposed tasks evolved as new techniques were investigated and some other were considered as a dead-end. The time invested for each of the phases of this work can be seen in the next Fig. 1.1.

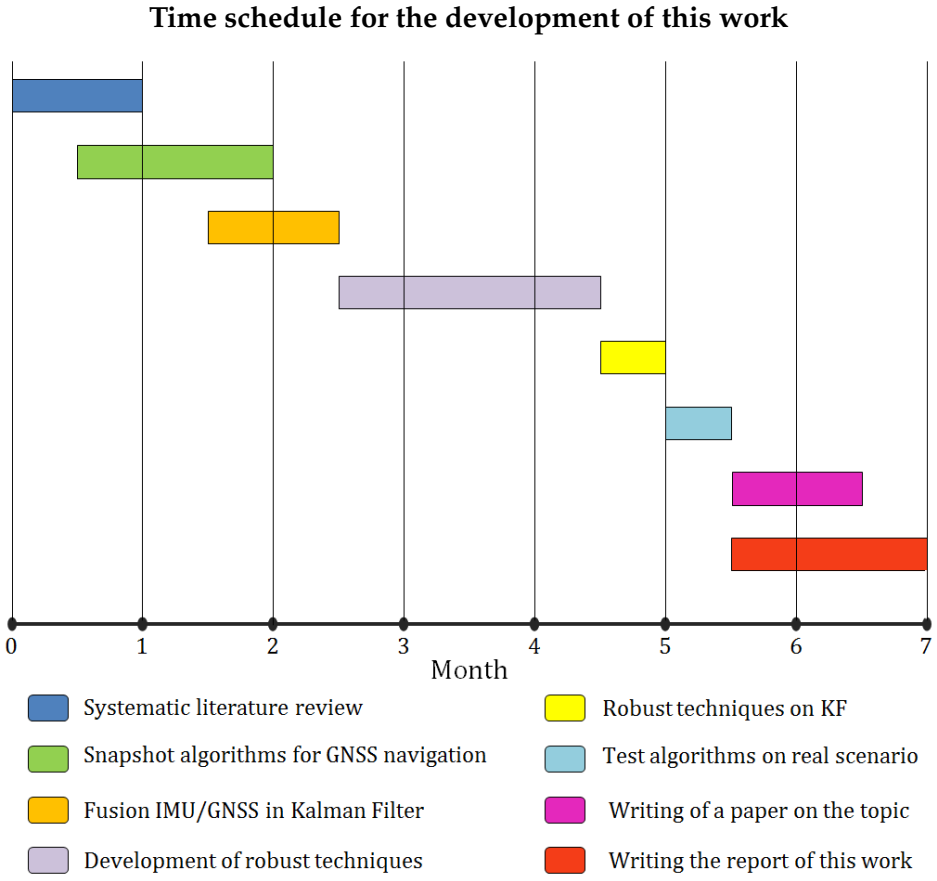


FIGURE 1.1: Time invested for each of the tasks during the development of this work.

The algorithms have been built in MATLAB, as it is convenient for fast prototyping, as well as presenting several advantages such as its large database of statistical functions, the capability to work with matrices or its appealing debugging process. Nonetheless, the data from the GNSS and IMU recorded during the measurement campaigns is extracted from a C++ software framework developed during the last years in the Nautical Systems department at DLR. This real-time framework operates with high rate GNSS data, and contains the implementation of several algorithms for GNSS positioning for subsequent research and project work, as well as live demonstrators. After prototyping the proposed algorithms in MATLAB, the next step within this work is the migration of those to the C++ real-time framework.

## 1.2 Thesis Outline

The rest of this work is organized as follows: next chapter provides a discussion on the state of the art of robust estimation for GNSS navigation and the related work. Then, chapters 3 to 5 constitute the methodology and the basics of satellite-based navigation, inertial navigation and robust estimation respectively. Chapter 6 presents the experimental setup of the vessels and the scenarios in which the algorithms will be tested. Chapters 7 and 8 discuss the results on the snapshot positioning using robust methods and on the fusion of the IMU and GNSS information in KF. Finally, in the last chapter the conclusions and future work of this study are presented.

Chapter 2

# Related Work

Classical methods of LS estimation are known to be rather susceptible to outliers or extreme observations, responsible for gross and unexpected errors in GNSS positioning. These large errors in the position solution constitute a serious concern for the community, especially for transport safety critical applications in domains such as aviation, maritime, railway or road. In the said domains, degradation in the navigation system performance without a notice within the specified time to alert would endanger lives.

In order to find a solution which is less affected by the outliers, a number of robust estimation schemes had been developed [26]. These methods are mainly based on checking the consistency of the observations where the influence of the measurements not fitting the underlying functional or stochastic model is reduced compared to those which fit well [69].

The methods of robust regression have a relatively long history with numerous reported applications for general data analysis as [38]. The usage of similar methods for robust GNSS positioning had also recently attracted an attention due to the advent of multi-constellation multi-frequency receivers, which allow to exploit an inherent redundancy of the observables. For example, mitigation of multiple outliers for GNSS positioning has been reported in [68] using M-estimation and the authors confirmed superior performance of the scheme over classical LS solution for the scenarios with multiple outliers. A modified Danish method using correlated phase observations for double difference phase approach had been presented in [69], although the test data have been taken only for the static scenario.

Although some attempts to benchmark different robust estimation schemes have been recently reported, the works either considered only few methods for general linear regression (e.g. non-positioning application) problem [61] or used simulated GNSS faults [26]. Although an extensive analysis had been provided in [26] with a representative set of methods covered, the authors used the data with multiple simulated outliers of significant amplitude, and, therefore, the performance of the approaches in real environment with less prominent faults is still not clear. Moreover, highly practical extensions of the methods for $C/N_0$ leveraged GNSS observations (weighting schemes) were not considered in this work. Some reports have addressed a problem of developing robust schemes exclusively for challenging GNSS positioning applications. For example, in a series of works [55, 57] the authors suggested to employ RANSAC-like strategies using minimum observation subset for GNSS outlier mitigation. Although the methods showed promising performance on the simulated data, no comparison to the performance of alternative robust schemes has been provided. Interestingly, similar consistency checking approach based on the measurement subset comparison as reported in [15] was equally likely to improve or degrade the positioning accuracy. According to [15], this effect could be partially explained as removal of a poor measurement can result in adverse signal geometry and, subsequently, degraded position accuracy. Some previous works of the same group also showed that although conventional sequential

testing approaches can successfully eliminate NLOS and multipath-contaminated signals in environments where the majority of signals are LOS, in environments with multiple NLOS and multipath signals, the sequential testing approaches (i.e., RAIM-like) are prone to eliminating wrong signals. Still, the overall results as reported in [15] were neutral, and, as only one specific robust scheme had been evaluated, can hardly be generalised for other robust schemes.

In 2008, [56] presented the Range Consensus (RANCO) algorithm which follows a strategy similar to the one in some classical robust estimators: the selection of the "best" subset of satellites to get a position solution, rather than use all satellites in view. The novelty of this work is that it includes an exclusion and ranking of the subsets based on the quality of the geometry of the satellites conforming those subsets. Additional satellite measurements can be labelled as inliers and take part in the position solution of a subset if their residuals pass certain threshold based on range comparison. Fig. 2.1 illustrates the flow diagram of the RANCO algorithm ($WSSE$ stands for Weighted Sum of the Squared Errors). As drawback, one could mention that this technique relies too heavily on the geometry of the satellites within a subset and it lacks a statistical meaning justifying its robustness.

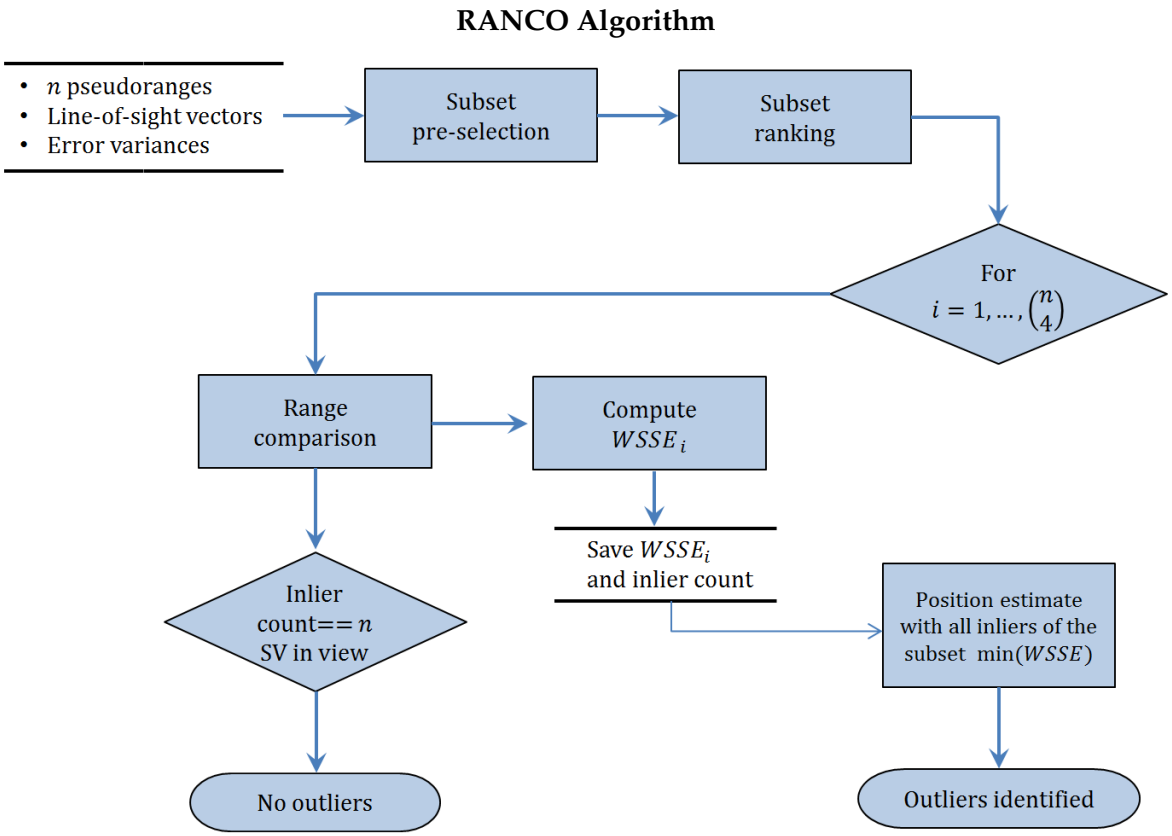


FIGURE 2.1: Data flow diagram for the RANCO algorithm. Image adapted from [56].

A typical approach to cope with the deficiencies of pure GNSS positioning is to augment the system with auxiliary sensors, such as inertial ones. Among clear advantages of the inertial sensors one could mention that they are completely self-contained, immune to interference, highly dynamical, small size and relatively lightweight. Unfortunately, the inertial sensors provide only incremental information and the integration output drifts over time when no external reference is provided. However, inertial sensors have complementary properties to those of GNSS and both sensors are often integrated to improve navigation robustness resulting both in highly dynamical and drift-free system. IMU utilization allows to bridge short-term GNSS outages caused by signal blockage or antenna shadowing and

even to support navigation in jammed environments especially if tight or even deep integration of GNSS raw data and inertial outputs is used. Finally, the accuracy of the combined system usually exceeds the specified accuracy of the GNSS alone and allows less than four satellites to play a role in the final navigation solution when tightly-coupled architectures are employed.

Augmentation of GNSS with inertial sensors in order to mitigate intentional or unintentional GNSS signal interference has been reported by several authors [34, 9]. Such systems are able to deliver position and velocity information at rapid update rate while preserving a low noise content due to the smoothing behavior of inertial integration. Increasingly, commercial systems [12] are becoming available which provide an integration of GNSS and Micro-Eletro-Mechanical Systems (MEMS) IMUs. The navigation systems for maritime applications have also a relatively long history of integration using Extended KF (EKF) such as [39], where early GPS, speed log and Loran-C have been combined. The seminal work [41] also tried to assess the possibility to replace more expensive Fiber Optic Gyro (FOG) IMU with lower cost MEMS IMU in hybrid navigation systems and assessed the performance of the system under presence of GNSS faults in maritime scenarios. In our recent work [70] it is have evaluated the impact of inertial sensor quality on the performance of hybrid IMU/GNSS system in maritime applications. The obtained results confirmed that the quality of the inertial sensor mainly affect the GNSS outage bridging (both position and heading), while the performance of Fault Detection and Exclusion functionality (part of Integrity Monitoring in RAIM) as well as the accuracy (smoothing of GNSS noise) remained almost not affected by the quality of IMU.

Chapter 3

# Satellite-based Navigation



This chapter will present the basics of the methodology for satellite-based navigation. This chapter is divided into seven sections: the first one will be dedicated to the different coordinate frames used for navigation purposes and the relationships between them. The second is devoted to the explanation of the GNSS architecture. In the next section, one finds a characterization of the sources of error for the satellite signal. Finally, the last sections are devoted to the description of the estimation of position, velocity and attitude of the target.

## 3.1 Coordinate Frames and Transformations

In navigation, we face the problem of dealing with multiple coordinate systems. On one hand, inertial sensors measure their motion with respect to an inertial or body frame. On the other hand, GNSS measures the position and velocity of a receiver's antenna with respect to a constellation of satellites. However, the user wants to know their position with respect to the Earth, and these coordinates have to be represented in some understandable format for him (e.g. coordinates within the local navigation area).

For accurate navigation, the relationship between the different coordinate frames must be properly modelled. In this section, it is presented the coordinate systems in positioning:

**Geodetic Coordinate System.** The geodetic coordinate system is widely used in GNSS-based navigation. A point near the Earth's surface is characterized in terms of longitude, latitude, and height (or altitude), which are respectively denoted by $\lambda, \varphi$, and $h$. The longitude measures the rotational angle (ranging from $-180^\circ$ to $180^\circ$) between the Prime Meridian and the measured point. The latitude measures the angle (ranging from $-90^\circ$ to $90^\circ$) between the equatorial plane and the normal of the reference ellipsoid that passes through the measured point. The height (or altitude) is the local vertical distance between the measured point and the reference ellipsoid.

**Earth-Centered Inertial Coordinate System.** The ECI coordinate system locates its origin at the center of gravity of the Earth. Its z-axis $Z_i$ is aligned with the spin axis of the Earth, the x-axis $X_i$ points towards the vernal equinox, and the y-axis $Y_i$ completes the right hand orthogonal coordinate system.

**Earth-Centered Earth-Fixed Coordinate System.** The ECEF coordinate system is similar to the ECI frame, except that all axes remain fixed with respect to the Earth. The z-axis $Z_e$ is along the spin axis of the Earth, pointing to the North Pole, The x-axis $X_e$ points from the center to the intersection of the equator with the Prime meridian (which defines the $0^\circ$ longitude), The y-axis $Y_e$ is orthogonal to the z and x axis with the usual right-hand rule, going from the origin to the intersection between the equator and the $90^\circ$ degrees

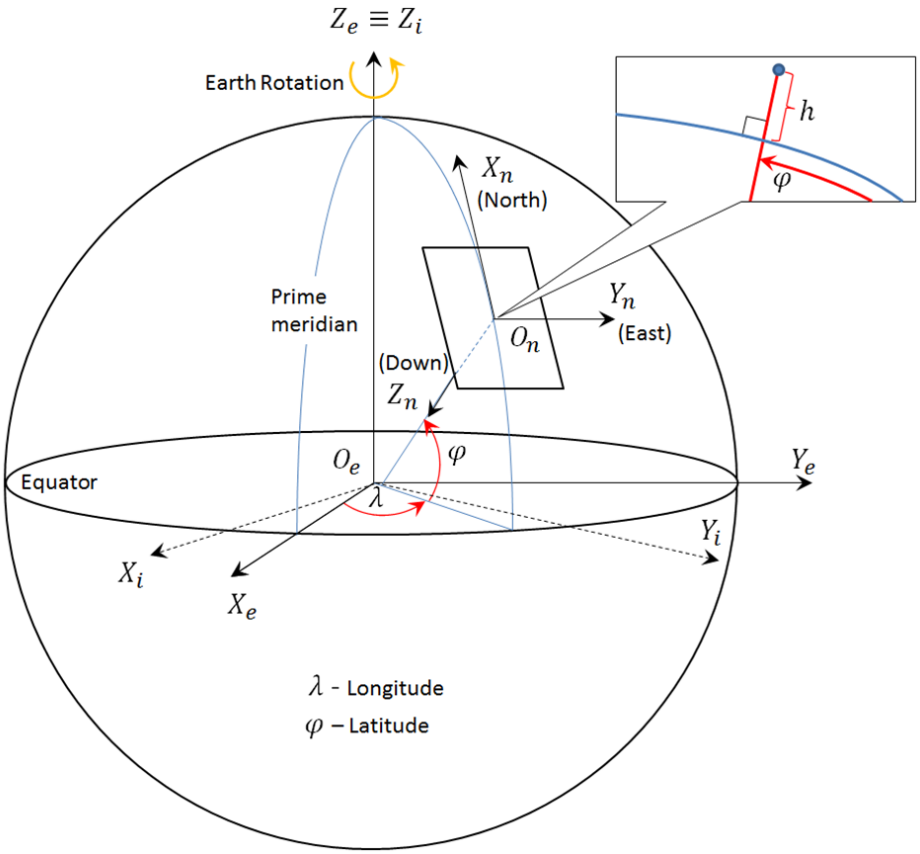


FIGURE 3.1: Coordinate systems: Geodetic $\{\lambda, \varphi, h\}$, ECI $\{X_i, Y_i, Z_i\}$, ECEF $\{X_e, Y_e, Z_e\}$ and NED $\{X_n, Y_n, Z_n\}$ represented. Image adapted from [4].

east meridian. It is commonly used as the reference frame, as well as the resolving frame, as the user wants to know their position relative to the Earth.

**Local North-East-Down Coordinate System.** The local NED coordinate system is also known as a navigation or ground coordinate system. The local NED frame plays a very important role in flight control and navigation. It is a coordinate frame fixed to the earth's surface. Based on the WGS84 ellipsoid model, with its origin and axes defined as following:

1. The origin $O_n$ is arbitrarily fixed to a point on the earth's surface.
2. The X-axis (denoted by $X_n$ ) points toward the ellipsoid north (geodetic north).
3. The Y-axis (denoted by $Y_n$ ) points toward the ellipsoid east (geodetic east).
4. The Z-axis (denoted by $Z_n$ ) points downward along the ellipsoid normal.

**Body Coordinate System.** The body frame, sometimes known as the vehicle frame, comprises the origin and orientation of the object for which a navigation solution is sought [14]. The origin is coincident with that of the local navigation frame, but the axes remain fixed with respect to the body and are generally defined as $x =$ forward (i.e., the usual direction of travel), $z =$ down (i.e., the usual direction of gravity), and $y =$ right, completing the orthogonal set. For angular motion, the x-axis is the roll axis, the y-axis is the pitch axis, and the z-axis is the yaw axis. Hence, the axes of the body frame are sometimes known as roll, pitch, and yaw. In reality, there is still a practical difference between the body of the tracked vehicle and the actually the body of the measured sensors, due to technical reasons the position and the axis of the sensors (accelerometers, gyroscopes, magnetometers, etc.) are not co-aligned with the rest of the body,

meaning that a level arm compensation is always required when the information from the inertial measurements is fused with the satellite navigation.

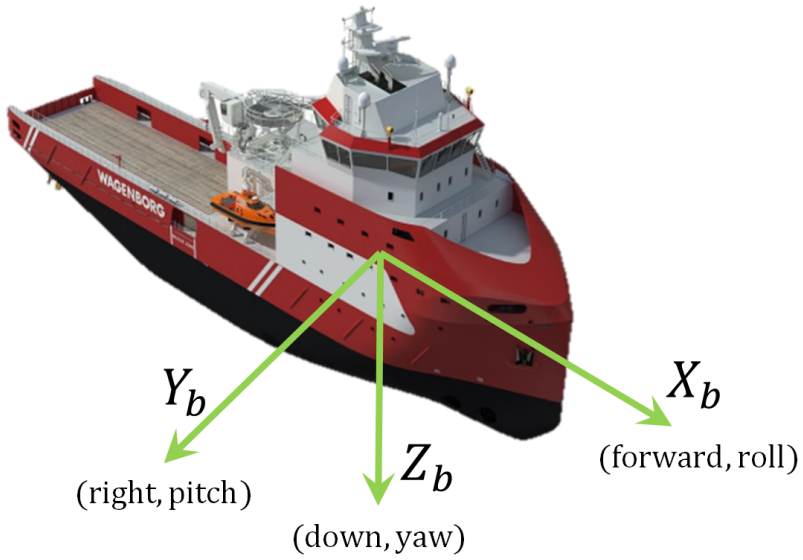


FIGURE 3.2: An example of body coordinate system.



## 3.2 GNSS Architecture

Global Navigation Satellite Systems consist of a set of satellites, called constellation, orbiting around the Earth, constantly transmitting signals with the primary purpose of enabling the users to determine their position. Its development started in 1973 and with its first prototype satellite launched in 1978, the American Global Positioning System (GPS) was the only fully operation GNSS providing global coverage. The Russian GLObal NAvigation Satellite System (Glonass) was restored to full operation in December 2011, while the European positioning system Galileo is still under development by the European Union [14]. Additionally, there are regional systems being developed by China, India and Japan.

The satellite-based positioning principle is based on the time-of-arrival of the signal received by the from the satellites. The transmitted signal encodes its time of emission from the satellite, therefore the user can subtract the time of arrival minus the time of emission and, multiplying by the speed of light, obtain the distance between satellite and receiver. As the position of the satellite is also part of the navigation message, solving the positioning problem of the receiver simply consists on solving a geometric problem. At least four satellite signals are needed to compute the position of the target, as the clock offset of the receiver must be estimated simultaneously with the position.

GNSS offers a basic radial positioning accuracy of 1.0–3.9m in the horizontal plane and 1.6–6.3m in the vertical axis, although this highly depends on the type of service, the quality of the receiver and the geometry of the satellites with respect to the target. Differential techniques can improve this to within a meter by making use of base stations at known locations to calibrate some of the errors. Carrier-phase positioning can give centimeter accuracy for real-time navigation and millimetre accuracy for surveying and geodetic applications [14].

A GNSS basically consists of three main segments: the space segment, which comprises the satellites; the control segment (also referred to as the ground segment), which is responsible for the proper operation of the system; and the user segment, which includes the GNSS receivers providing positioning, velocity and precise timing to users (see Fig. 3.3).

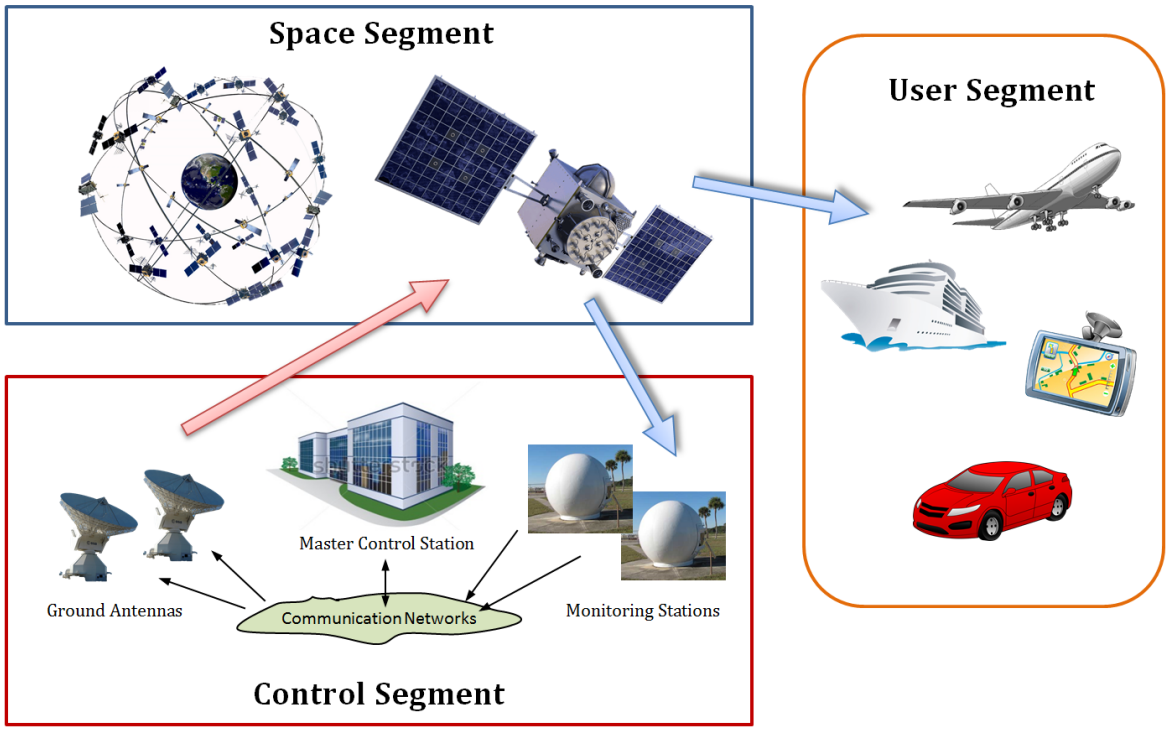


FIGURE 3.3: GNSS architecture.

### Space Segment

The GNSS space segment is constituted by satellite constellations, having enough satellites to assure a visibility of at least four satellites simultaneously from any point of the surface of the Earth. The space segment is in charge of the generation and transmission of code and carrier phase signals, as well as the navigation message. The satellites are equipped with highly stable atomic clocks (generally using atoms of rubidium, caesium or hydrogen) in order to provide an accurate measure of the timing.

Satellites have various structures and mechanisms to keep them in orbit, communicate with the control segment and broadcast signals to receivers. The satellite clocks are one of the critical components of GNSSs. For this reason, satellites are equipped with high-stability atomic clocks (rubidium and caesium).

GNSS satellites continuously transmit navigation signals at two or more radio frequencies. These signals contain ranging codes and navigation data to allow users to compute both the travel time from the satellite to the receiver and the satellite coordinates at any epoch. The main signal components are described as follows:

- *Ranging code:* Sequences of zeros and ones which allow the receiver to determine the travel time of the radio signal from the satellite to the receiver. They are called PRN sequences or PRN codes.
- *Carrier:* Radio frequency sinusoidal signal at a given frequency measuring the range between a satellite and receiver expressed in units of cycles of the carrier frequency. This measurement can be made with very high precision (of the order of millimeters), but the whole number of cycles between satellite and receiver is not measurable [44].
- *Navigation data:* A binary-coded message providing information on the satellite ephemeris (pseudo-Keplerian elements or satellite position and velocity), clock bias parameters, almanac (with a reduced-accuracy ephemeris data set), satellite health status and other complementary information.

GPS signals are transmitted on two radio frequencies in the L band, referred to as Link 1 (L1) and Link 2 (L2), or L1 and L2 bands of 1575.420 and 1227.600 MHz respectively. The GPS signal modernisation includes an additional Link 5 (L5) frequency and several new ranging codes on the different carrier frequencies. They are referred to as the civil signals L2C, L5C and L1C and the military M code. Specifically, L2C was designed to meet commercial needs, allowing the development of low-cost, dual-frequency civil GPS receivers and it will be subject of study in this work. Two services are available in the current GPS system:

**SPP:** The Single Point Positioning is an open service, free of charge for worldwide users. It is a single-frequency service in the frequency band L1.

**PPP:** The Precise Point Positioning is restricted by cryptographic techniques to military and authorised users. Two navigation signals are provided in two different frequency bands, L1 and L2.

Additionally, the positioning services can be further improved with the use satellite-based augmentation systems (SBAS). These systems are constituted by multiple strategically located ground stations, receiving the measurements from the satellites providing differential corrections, service and integrity alerts [14] that are directly broadcasted to the end users.



### Control segment

The control or ground segment is responsible for the proper operation of the GNSS. It is responsible for the following functions:

- to control and maintain the status and configuration of the satellite constellation;
- to predict ephemeris and satellite clock evolution;
- to keep the corresponding GNSS time scale (through atomic clocks);
- to update the navigation messages for all the satellites.

For the GPS, the ground segment is formed by a network of Monitoring Stations (MS), a Master Control Station (MCS) and the Ground Antennas (GA). The Master Control Station, located in Colorado Springs, USA, is the core of the control segment. It is responsible for operating the system and providing command, control and maintenance services to the space segment. The Monitoring Stations are distributed around the world, are equipped with standard atomic clocks and GPS receivers to collect GPS data continuously for all the satellites in view from their locations. The collected data are sent to the Master Control Station where they are processed to estimate satellite orbits (ephemerides) and clock errors, among other parameters, and to generate the navigation message.

Finally, the Ground Antennas uplink data to the satellites via S-band radio signals. These data include ephemerides and clock correction information transmitted within the navigation message, as well as command telemetry from the MCS [54].

### User segment

Despite being generally denoted as GNSS receiver, the user segments comprises several modules whose function will be briefly described next. On first place, the antenna converts the incoming GNSS radio signals to electrical signals, which in turn, are the inputs for the receiver. The receiver demodulates the signals using a reference oscillator (generally using a quartz crystal oscillator) made of to provide a time reference. Then, the ranging processor uses acquisition and tracking algorithms to determine the range from the antenna to each of the satellites used from the receiver outputs. It also controls the receiver and decodes the

navigation messages. Finally, the navigation processor uses the ranging measurements to compute a position, velocity, and time (PVT) solution. For further information on the user's hardware, refer to [14].

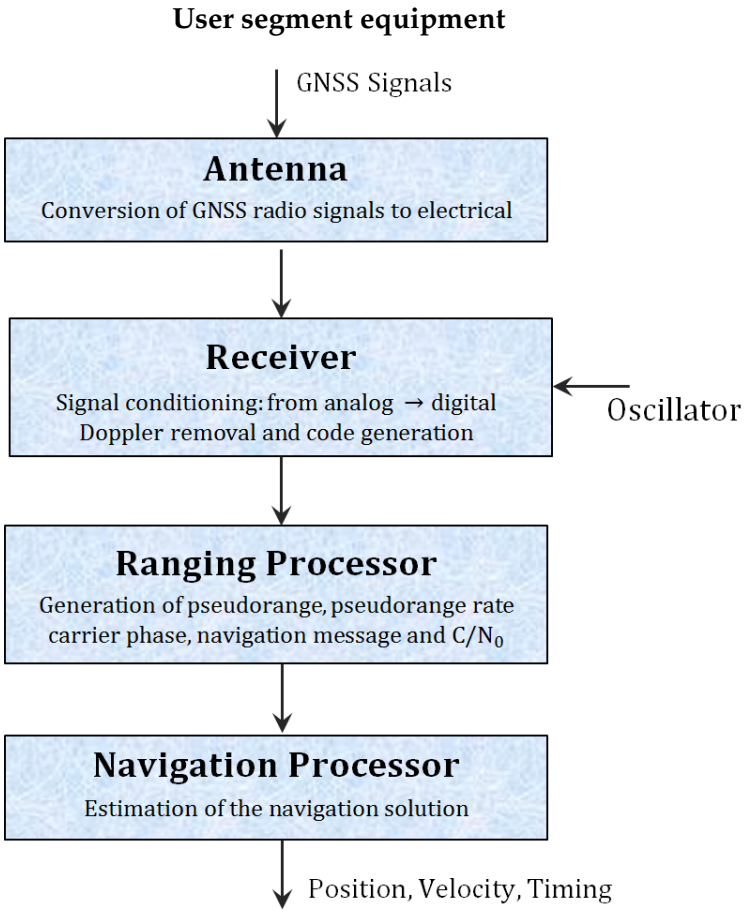


FIGURE 3.4: Diagram with the hardware related to the GNSS user segment.

## 3.3 Error sources

Errors in satellited-based navigation are grouped into three categories based on their source:

**Satellite-based errors** Despite being constantly monitored by the ground stations, satellites are eventually the source of error for positioning errors. Mostly, these errors are due to the delays in the satellite clock error update for the users or ephemerides errors. It must be taken into account the time elapsed between the emission and the reception of the navigation message, as the exact position of the satellite will have slightly changed from the coordinates provided from the ephemerides.

**Receiver-based errors** In this case, the errors are due to noise in the reception of the signal, as well as small errors coming from the inter-channel biases and errors in the antenna [31].

**Signal propagation errors** They include delays associated to passing through the ionosphere and troposphere layers of the atmosphere, as well as intentional jamming and spoofing of the signals and the errors related to multipath and non-line-of-sight effects.

The accuracy of the Position, Velocity and Timing (PVT) solution highly depends on the capability to detect and mitigate all these measurement errors. Fig. 3.5 provides an insight

on rough estimations on how much impact each of the error sources might have in the pseudorange measurement. In this work, signal propagation errors are specially considered, as they are the only ones that could potentially be detected and mitigated by a regular user.

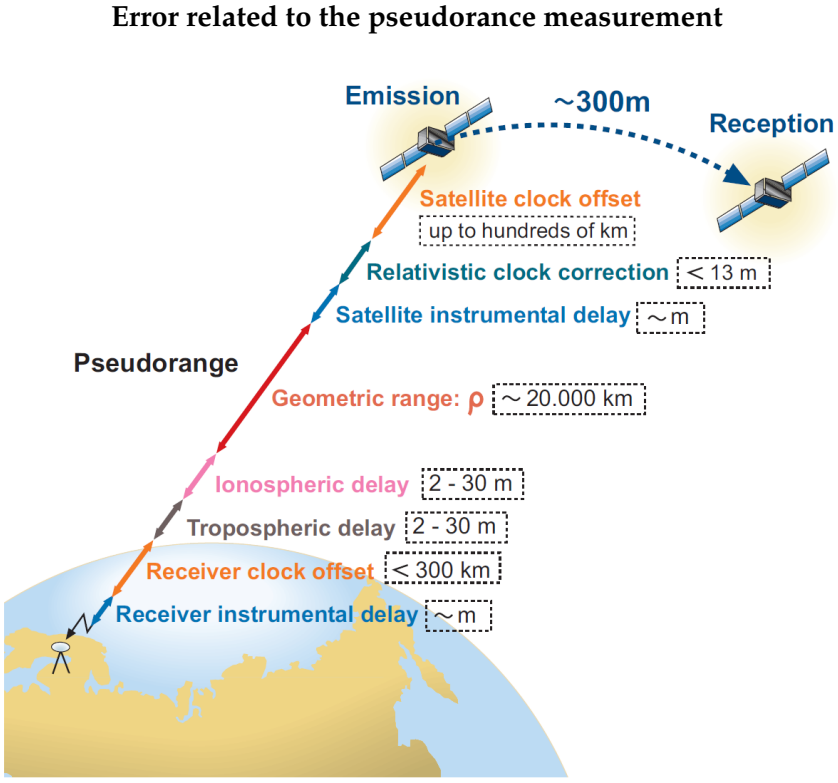


FIGURE 3.5: Pseudorange measurement contents. Image from [54].

In the rest of this section, the source of errors related to signal propagation will be described.

### Ionosphere errors

The ionosphere is a region of Earth's upper atmosphere, from about 60 km to 1,000 km altitude. The propagation speed of the GNSS signals is affected by the presence of electrical charge in the ionosphere [54]. The influence of the ionosphere varies with the solar activity and the geomagnetic field. Hence, ionospheric refraction varies with frequency, geographic location, and time. The resulting range error, for GPS frequencies, can vary from less than 1 m to more than 100 m. This dependence on the signal frequency allows us to remove the first-order effects using two-frequency measurements through a linear combination of code measurements:

$$R_{iono-free} = \frac{f_1^2 R_1 - f_2^2 R_2}{f_1^2 - f_2^2} \tag{3.1}$$

Single-frequency receivers need to apply a model to remove the ionospheric refraction, which can reach up to few tens of metres, depending on the elevation of rays and the ionospheric conditions. The most well known models for GPS are Klobuchar and NeQuick Model, which use an approximation of the latitude and longitude of the user position, as well as the elevation angle and azimuth of the corresponding satellite. An example on the values for the ionosphere corrections are provided in Fig. 3.6, belonging to the NeQuick2 model. In this work, the ionosphere corrections are taken from the Klobuchar model. Despite this model generally provides the ionospheric delay in the GPS L1 signals, it can also

be used to estimate the ionospheric time delay in other frequency signals or for the Glonass and Galileo signals, as well. Indeed, taking into account that the ionospheric delay is inversely proportional to the square of the signal frequency, the delay for any GNSS signal transmitted on frequency $f_k$ is given by:

$$I_k = \left(\frac{f_1}{f_k}\right)^2 I_1 \tag{3.2}$$

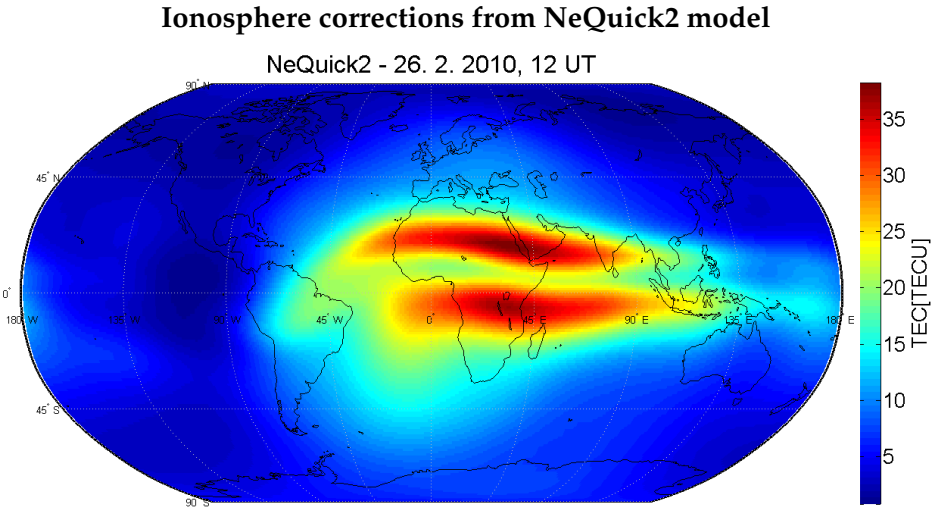


FIGURE 3.6: Global ionospheric map of 26th February 2010, 12 UT modeled by the NeQuick 2 model. Image from [42].

In Fig. 3.7, it is shown an example of the values for the ionosphere corrections obtained from the Klobuchar model for the observed satellites during two hours of measurement campaign in Koblenz (Germany). The magnitude of the ionospheric corrections varies within time, changing from around 11m to almost 26m for one of the satellites signals.

### Troposphere errors

The troposphere is the atmospheric layer between Earth's surface and an altitude of about 60 km. It consists of dry gases and water vapour, causing the GNSS signals to be refracted and delayed. This delay, frequency independent, depends on the temperature, pressure and humidity as well as the transmitter and receiver antenna locations, and therefore it is hard to model troposphere errors accurately using global general models.

It is difficult to separate error components stemming from the radial orbital errors, signal propagation errors, clock errors, antenna phase center variation, and errors in the station height. In this work, the troposphere effects are corrected using the Saastamoinen model [2]. In Fig. 3.8, it is shown the magnitude of the troposphere corrections from Saastamoinen model. This example is taken during the two hours and in Koblenz, as it is shown previously for the ionosphere corrections. As it was observed for the ionosphere, troposphere corrections fluctuate from 3 to 23 meters depending on the satellite, although most of the satellites have their tropospheric corrections steady between 3 and 5m.

### Multipath Errors

The multipath is the phenomenon resulting in a radio signal reaching the receiving antenna by two o more paths. For land applications, signals are generally reflected off the ground, buildings, or trees, while for aircraft and ships, reflections off the host-vehicle body are more

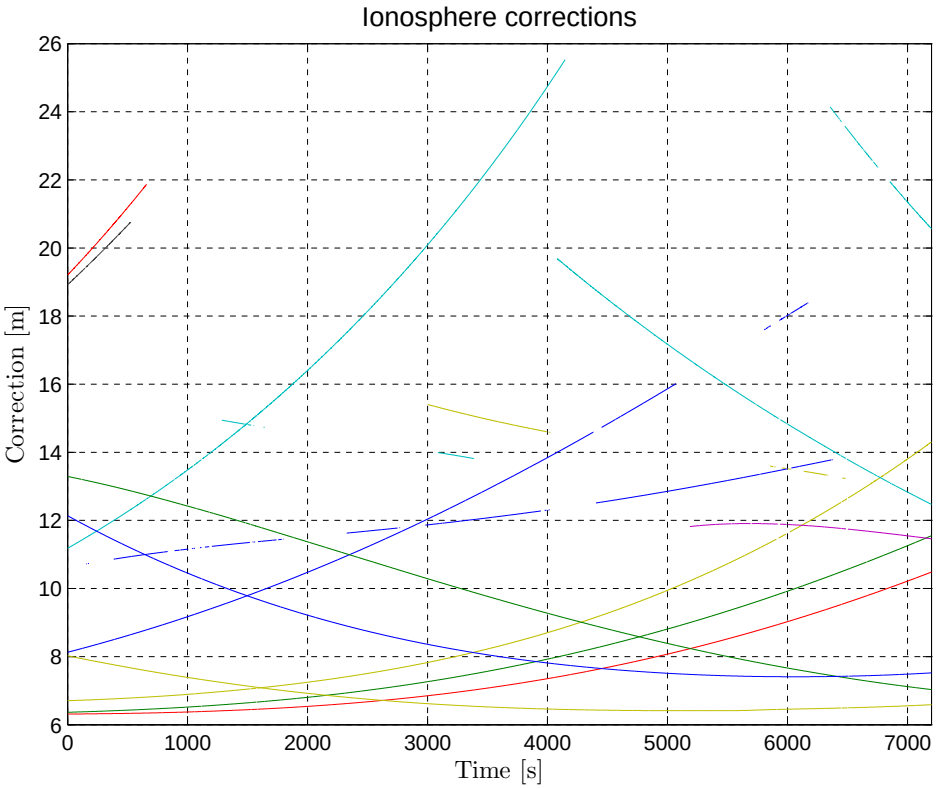


FIGURE 3.7: Ionosphere corrections for the available satellites during a measurement campaign in Koblenz, on the $25^{th}$ March, 2014.

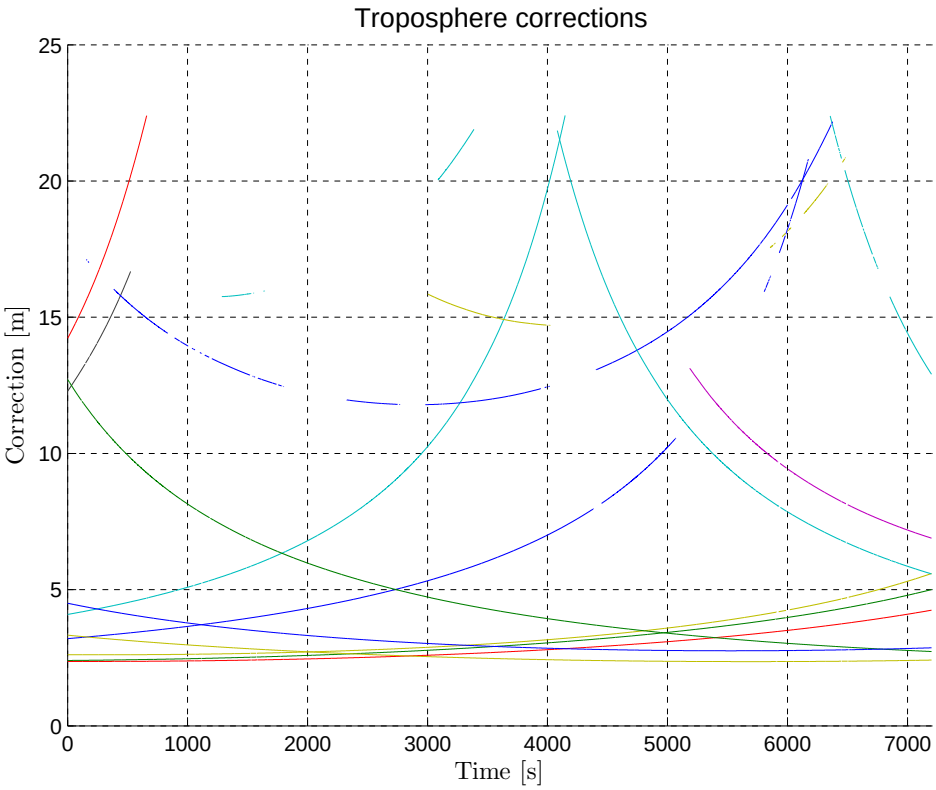


FIGURE 3.8: Troposphere corrections for the available satellites during a measurement campaign in Koblenz, on the $25^{th}$ March, 2014.

common. Interference can also occur from diffracted signals. The reflected and diffracted signals are always delayed with respect to the direct signals and have a lower amplitude unless the direct signals are attenuated (e.g., by a building or foliage). Low-elevation-angle signals are usually subject to the greatest multipath interference. Specially in urban scenarios, with numerous canyons interfering in the signals, The receiver gets a mixture of non-line-of-sight (NLOS), multipath contaminated and clean line-of-sight (LOS) signals, as shown as an example in figure 3.9.

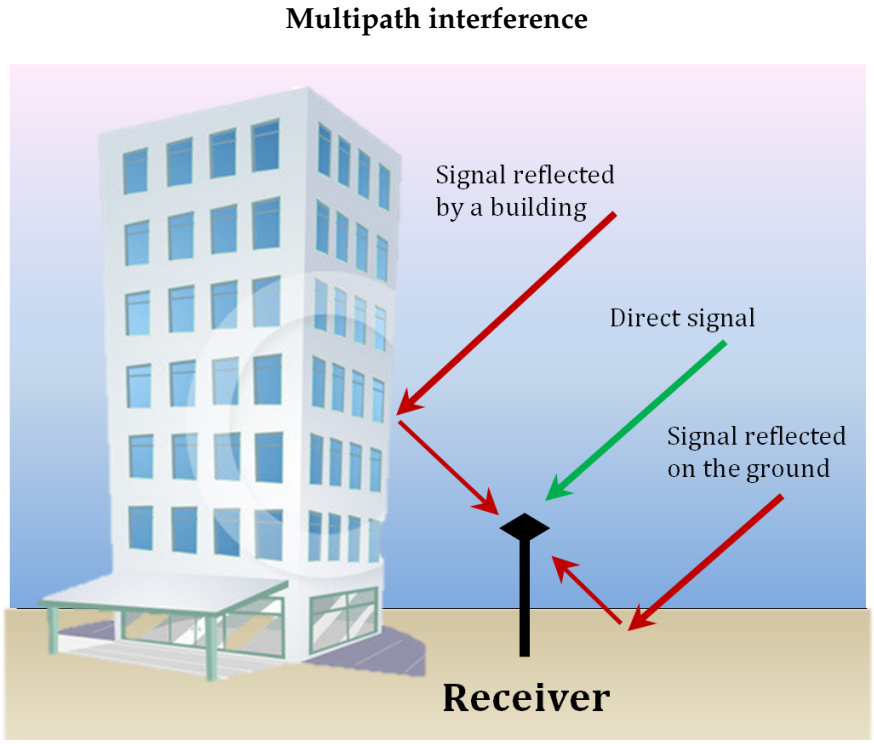


FIGURE 3.9: Example of multipath signal: the receiver gets a mixture of clean LOS signal and reflected signals from the same satellite.

This error is different for different frequencies. It affects the phase measurements, as well as the code measurements. In the case of the code, it can reach a theoretical value of 1.5 times the wavelength of the signal. This means, for instance, that multipath in the GPS L1 code can reach up to 450m, although higher values than 15m are difficult to observe [54]. A powerful means for the detection of diffracted signals is inspection of the signal-to-noise ratio (SNR) or of the carrier-to-noise ratio ($C/N_0$). A proper weighting of the observables, based on the SNR or $C/N_0$ values, can be used for minimizing the diffraction effect on coordinate estimates [16]. However, this is not a definitive solution as NLOS signals can be nearly as strong as the directly received signals [22], but also notably weak, making high-sensitivity receivers even more susceptible to be affected by this phenomenon.

### NLOS Signal Reception

NLOS reception occurs where the direct line-of-sight signal is blocked and the signal is received only via reflections, as illustrated with an example in Fig. 3.10. This results in a pseudo-range measurement error equal to the path delay, which is the difference between length of the path taken by the reflected signal and the (blocked) direct path between satellite and receiver. This error is always positive and, although typically tens of metres, is potentially unlimited [16]. Signals received via distant tall buildings can exhibit errors of more than a kilometre.

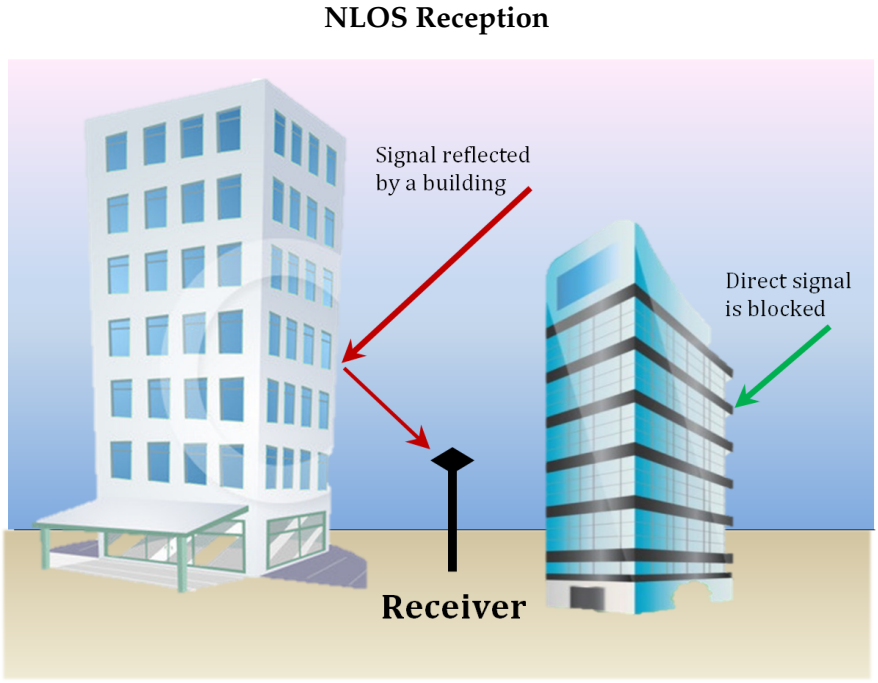


FIGURE 3.10: Example of reception of a non-line-of-sight signal, the direct signal gets blocked by an obstacle.



## 3.4 Position Estimation

GPS utilizes the concept of TOA (Time of Arrival) ranging to determine the receiver position $\mathbf{p} = (x, y, z)$ and clock offset $c\delta t$ from pseudorange measurements $R$ of at least four satellites in view. The positioning principle is based on solving a geometric problem from the measured ranges to the satellites, with known coordinates. The code pseudorange measurements $R_j$ for each of the satellites is expressed as:

$$R^j = \rho^j + c\delta t^j + Tr^j + \tilde{\alpha}_1 I^j + \mathcal{M}^j + \varepsilon^j, \quad j = 1, \ldots, n \tag{3.3}$$

where:

- $\rho^j = c\left(t^j - t\right)$ is the product of the speed of light and the difference between the time of the signal emission from the $j$ satellite and the time from the receiver's clock at the reception time.
- $c\delta t^j$ is the clock offset of the $j^{th}$ satellite,
- $Tr^j$ is the troposphere correction,
- $\tilde{\alpha}_1 I^j$ is the first order ionosphere correction,
- $\mathcal{M}^j$ is the signal error from possible multipath effects,
- $\varepsilon^j$ represents the receiver noise terms, and
- $n$ is the number of satellites observed.

The pseudorange can be reformulated, after neglecting the multipath and receiver noise terms, as the geometric distance between the $j$ satellite and the receiver as:

$$R^j - D^j \approx \sqrt{(x^j - x)^2 + (y^j - y)^2 + (z^j - z)^2} + c\delta t, \quad j = 1, ..., n \tag{3.4}$$

where the left-hand side containts the measurements $R^j$ and all modelled terms $D^j = -c\delta t^j + Tr^j + \tilde{\alpha}_1 I^j$. The right-hand side contains the four unknown parameters: the receiver coordinates $(x, y, z)$ and the receiver clock offset $c\delta t$.

Equation 3.4 defines a nonlinear system, whose usual solution technique consists of linearising the geometric range $\rho$ in the neighbourhood of a point $(x_0, y_0, z_0)$ corresponding to the approximate solution of the receiver, as seen in the Fig. 3.11:

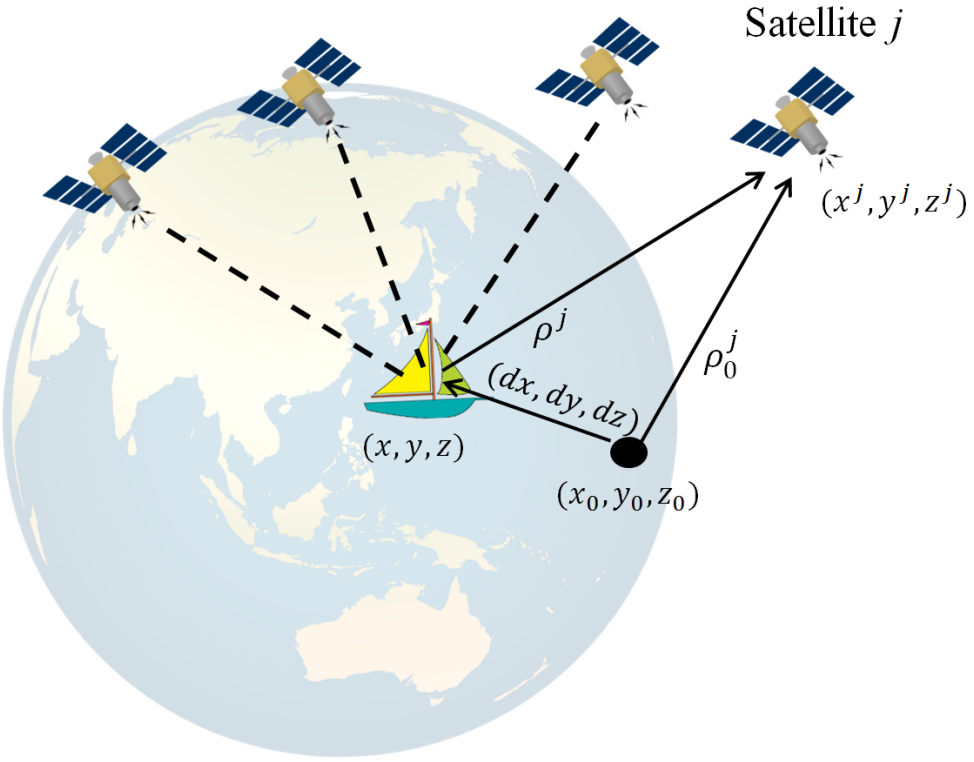


FIGURE 3.11: Geometric concept of GNSS positioning: equations are linearised about the approximate receiver coordinates $(x_0, y_0, z_0)$. The correction $(dx, dy, dz)$ is estimated with a least squares adjustment.

Then, linearising the satellite-receiver geometric range $\rho^j$

$$\rho^j (x, y, z) = \sqrt{(x^j - x)^2 + (y^j - y)^2 + (z^j - z)^2} \tag{3.5}$$

gives, for the approximate solution $\mathbf{p}_0 = (x_0, y_0, z_0)$,

$$\rho^j \approx \rho^j + \frac{x_0 - x^j}{\rho^j} dx + \frac{y_0 - y^j}{\rho^j} dy + \frac{z_0 - z^j}{\rho^j} dz \tag{3.6}$$

with $dx = x - x_0, dy = y - y_0, dz = z - z_0$.

Rewriting the measurements as a linear system, where the unknowns are $dx, dy, dz$ and $c\delta t$, we obtain:

$$R^j - \rho_0^j - D^j = \frac{x_0 - x^j}{\rho_0^j} dx + \frac{y_0 - y^j}{\rho_0^j} dy + \frac{z_0 - z^j}{\rho_0^j} dz + c\delta t, \quad j = 1, \ldots, n \tag{3.7}$$

which can be expressed using matrix notation as:

$$\underbrace{\begin{bmatrix} R^1 - \rho_0^1 - D^1 \\ \vdots \\ R^n - \rho_0^n - D^n \end{bmatrix}}_{\mathbf{y}} = \underbrace{\begin{pmatrix} \frac{x_0 - x^1}{\rho_0^j} & \frac{y_0 - y^1}{\rho_0^j} & \frac{z_0 - z^1}{\rho_0^j} & 1 \\ \vdots & \vdots & \vdots & \\ \frac{x_0 - x^n}{\rho_0^n} & \frac{y_0 - y^n}{\rho_0^n} & \frac{z_0 - z^n}{\rho_0^n} & 1 \end{pmatrix}}_{G} \underbrace{\begin{bmatrix} dx \\ dy \\ dz \\ c\delta t \end{bmatrix}}_{\mathbf{x}} \tag{3.8}$$

where **y** is a $(n \times 1)$ vector containing the residuals between the measured and predicted pseudoranges; $G$ is the geometry matrix of size $(n \times 4)$, containing the receiver-satellite geometry, whose three first elements of each row are unit vector; and **x** is a $(4 \times 1)$ vector containing the difference between the true and approximate coordinates and the receiver clock offset $c\delta t$.

After solving the equation system 3.8, the estimate of the receiver coordinates is:

$$\begin{pmatrix} x \\ y \\ z \end{pmatrix} = \begin{pmatrix} x_0 \\ y_0 \\ z_0 \end{pmatrix} + \begin{pmatrix} dx \\ dy \\ dz \end{pmatrix} \tag{3.9}$$

Equation 3.4 can be linearised again about the estimation of the receiver's position. This iterative process continues until thee change between two consecutive iterations is below a given threshold. Typically, this process converges quickly, in a few iterations, even if starting with $(x_0, y_0, z_0) = (0, 0, 0)$, that is Earth's centre.

In general, eq. (3.8) is an over-determined system (for $n > 4$). As mentioned before, there are errors related to multipath and receiver noise which were neglected, and for that reason there is not a "exact" solution fulfilling the system. The parameters' solution can be taken as the vector **x** that minimises the discrepancy in the equation system. That is, the vector **x** provides the "best fit" of $\mathbf{y} \approx G\mathbf{x}$. The standard criterion in satellite navigation is the use of *least squares* adjustment. Least squares is an approach used in regression analysis to estimate the solution of overdetermined systems, for which the sum of the squares of the errors is minimized:

$$\min \|\mathbf{y} - G\mathbf{x}\|^2 = \min_x \sum_{i=1}^{n} (y_i - g_i\, x_i)^2 \tag{3.10}$$

with $g_i$ as the $i$th row of the $G$ matrix. The solution fulfilling such requirements is given by:

$$\mathbf{x} = \left(G^T G\right)^{-1} G^T \mathbf{y} \tag{3.11}$$

The discrepancy between the measurements (the difference between the pseudoranges and the geometric distances between satellites and the receiver) and the solution is the *residual* vector, calculated as follows:

$$\mathbf{r} = \left[I - G\left(G^T G\right)^{-1} G^T\right] \mathbf{y} = S\mathbf{y} \tag{3.12}$$

In order to calculate the error covariance matrix $P$ asociated to the estimated solution, it is assumed uncorrelated values of the measurements with the same variance $\sigma_\rho^2$. Taking $R = \mathrm{E} = \left[\varepsilon\, \varepsilon^T\right] = \sigma^2 I$, then:

$$P = \sigma_\rho^2 \left(G^T\, G\right)^{-1} = \begin{pmatrix} \sigma_N^2 & P_{N,E} & P_{N,V} & P_{N,t} \\ P_{E,N} & \sigma_E^2 & P_{T,V} & P_{T,t} \\ P_{V,N} & P_{V,E} & \sigma_V^2 & P_{V,t} \\ P_{t,N} & P_{t,E} & P_{t,V} & \sigma_t^2 \end{pmatrix} \tag{3.13}$$

Nevertheless, measurements are often not equally weighted but leveraged on the strength of the received signal or the elevation of the satellite. The quality of a measurement can be introduced into the least squares adjustment with a symmetric, positive-defined weighting matrix $W$. The solution using weighted measurements and the corresponding error covariance matrix are given by:

$$\mathbf{x} = \left(G^T W G\right)^{-1} G^T W \mathbf{y} \tag{3.14}$$

$$P = \left(G^T W G\right)^{-1} G^T W R W G \left(G^T W G\right)^{-1} \tag{3.15}$$

The weight matrix $W$ mentioned previously can be defined in whatever manner to account for the leverage of the measurement. However, if $W$ corresponds to the inverse of the covariance matrix $R$ of the measurements $W = R^{-1}$, then the covariance matrix becomes:

$$P = \left(G^T W G\right)^{-1} \tag{3.16}$$

The solution from a Weighted Least Squares (WLS) can be considered as the Best Linear Unbiased Estimate, which means that the solution presents the lowest estimation error among all linear estimators [28].

### 3.4.1 Dilution of precision

The quality of the user position estimate depends not only on the quality of the range measurements but also on the user-satellite observation geometry. The Dilution of Precision (DOP) concept provides a simple measure of the geometrical strength of the user-satellite configuration [24]. Poor geometry may have the effect of amplifying random errors and biases and, therefore, produce large position errors. Fig. 3.12 illustrates an example of good geometry for a simple two-dimensional ranging solution. In case of bad geometry, the rhombus representing the uncertainty regions would be way more elongated. The arcs show the mean and error bounds for each ranging measurement, while the shaded areas show the uncertainty bounds for the position solution and the arrows show the line-of-sight vectors from the user to the transmitters. The overall position error for a given ranging accuracy is minimized where the line-of-sight vectors are perpendicular.

The position information along a given axis obtainable from a given ranging signal is maximized when the angle between that axis and the signal line of sight is minimized. Therefore, the horizontal GNSS positioning accuracy is optimized where signals from low-elevation satellites are available and the line-of-sight vectors are evenly distributed in azimuth. Vertical accuracy is optimized where signals from higher elevation satellites are available [14].

The DOP parameters are obtained from the elements of the $Q$ matrix, also called *cofactor matrix*:

$$Q \equiv \left(G^T G\right)^{-1} = \begin{bmatrix} q_{xx} & q_{xy} & q_{xz} & q_{xt} \\ q_{yx} & q_{yy} & q_{yz} & q_{yt} \\ q_{zx} & q_{zy} & q_{zz} & q_{zt} \\ q_{tx} & q_{ty} & q_{tz} & q_{tt} \end{bmatrix} \tag{3.17}$$

from the previous matrix, the parameters are estimated as:

- Geometric Dilution of Precision:

$$GDOP = \sqrt{q_{xx} + q_{yy} + q_{zz} + q_{tt}} \tag{3.18}$$

- Position Dilution of Precision:

$$PDOP = \sqrt{q_{xx} + q_{yy} + q_{zz}} \tag{3.19}$$

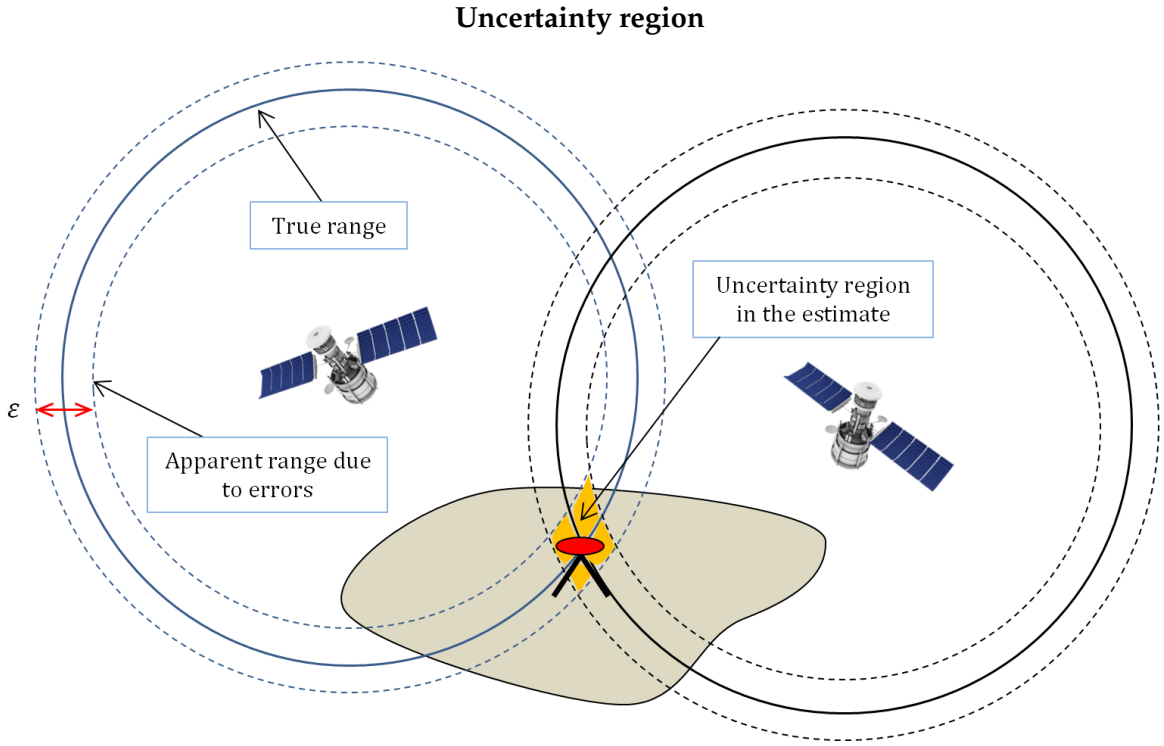


FIGURE 3.12: The measurement noise $\varepsilon$ is translated to the position estimation as an uncertainty region.

- Time Dilution of Precision:

$$TDOP = \sqrt{q_{tt}} \tag{3.20}$$

The previous DOP values are expressed in the equatorial system. When the local NED coordinate system is used, the matrix $Q$ must be transformed into the matrix $Q_n$. Denoting now as $Q_{n,p}$ that part of the matrix that contains only the geometrical components (disregarding the time-correlated components), as:

$$Q_{n,p} = R_e^n Q_x R_e^{nT} = \begin{bmatrix} q_{nn} & q_{ne} & q_{nd} \\ q_{ne} & q_{ee} & q_{ed} \\ q_{nd} & q_{ed} & q_{dd} \end{bmatrix} \tag{3.21}$$

where the rotation matrix $R_e^n$ contains the axes coordinate system [19]. Having this new $Q_n$, it is possible to obtain two additional DOP values for the horizontal and vertical position components:

- Horizontal Dilution of Precision:

$$HDOP = \sqrt{q_{nn} + q_{ee}} \tag{3.22}$$

- Vertical Dilution of Precision:

$$VDOP = \sqrt{q_{dd}} \tag{3.23}$$

Dilution of Precision is a geometrical interpretation of the timing and positioning accuracy. However, it is not an ultimate indication of the quality of the estimated solution. As can be seen in figure 3.13, despite having an excellent geometry of satellites, the signals that reach the receiver may be affected by severe multipath or reflection effects, obtaining a final position estimation with a gross error.

**Examples of geometries for the position solution**

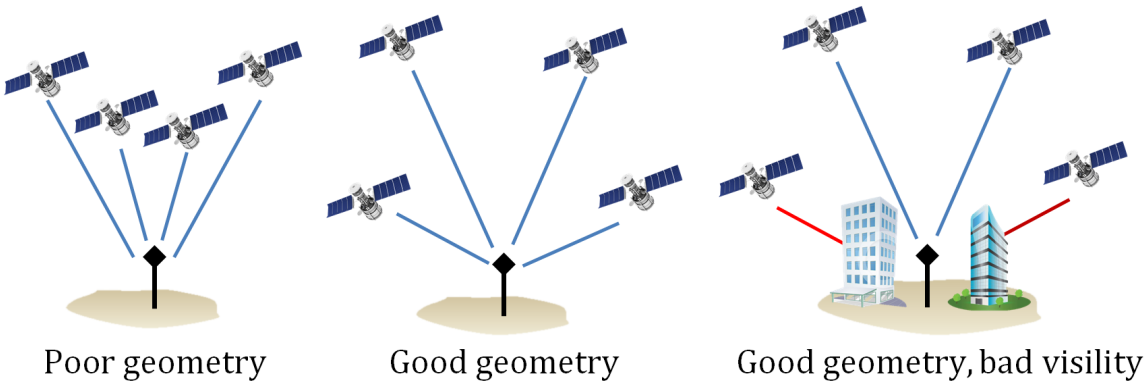


FIGURE 3.13: This figure exemplifies how the Dilution of Precision is not always a proper indicator of the quality of the position solution: even with a good geometry, the visibility from the receiver to the satellites might not be direct.

## 3.5 Velocity Estimation

In navigation, velocity over the ground can be obtained by using the Doppler effect. This effect denotes the difference between the frequency of the radiation received at a point and the frequency of the radiation at its source, when observer and source are moving with respect to each other. This value is known from GNSS specification, being denoted as Doppler shift. The Doppler equation for an electromagnetic wave can be written as:

$$f_r = \left(\frac{c+v}{c+v^j}\right) f_0 \tag{3.24}$$

where $c$ is the speed of light (m/s), $f_r$ is the received frequency (Hz), $f_0$ is the transmitted frequency (Hz), and $v, v^j$ are the speed of the receiver and the $j$th satellite respectively. note that this equation is only for 1D problem, as the equation assumes all the velocities to be along the LOS vector.

Given that the speeds of receiver and satellite are small compared to the speed of light, it can be proven that eq. 3.24 is approximately:

$$\Delta f = \frac{\Delta v}{c} f_0 \tag{3.25}$$

being $\Delta f = f_r - f_0$ the observed Doppler shift, and $\Delta v = v - v^j$ is the velocity of the receiver relative to the $j$th satellite. On the other hand, the receiver velocity can expressed using the pseudorange rate observation as:

$$\dot{\rho}^j = \left(\mathbf{v}^j - \mathbf{v}\right) \cdot \frac{\mathbf{p}^j - \mathbf{p}}{\|\mathbf{p}^j - \mathbf{p}\|} + c\dot{\delta}t + \dot{\varepsilon}^j \tag{3.26}$$

where:

- $\dot{\rho}^j$ is the pseudorange rate for the $j$th satellite,
- $\mathbf{v}^j$ is the velocity vector for the $j$th satellite,
- $\mathbf{v}$ represents the receiver's vector velocity,
- $c\dot{\delta}t$ is the rate of change of the receiver's clock offset,

- $\dot{\varepsilon}^j$ is the combined error due to changes during the measurement interval in the $j$th satellite clock error, troposphere and ionosphere corrections.

Reformulating the above equation in order to have a linear system of equations that can be solved using a least squares adjustment, as done previously for the position solution:

$$\underbrace{\begin{bmatrix} v_x \\ v_y \\ v_z \\ c\dot{\delta}t \end{bmatrix}}_{\mathbf{x}} = \left(G^T G\right)^{-1} G^T \underbrace{\begin{bmatrix} \mathbf{g}^1 \cdot \begin{bmatrix} \mathbf{v}^1 \\ 0 \end{bmatrix} - \dot{\rho}^1 \\ \vdots \\ \mathbf{g}^n \cdot \begin{bmatrix} \mathbf{v}^n \\ 0 \end{bmatrix} - \dot{\rho}^n \end{bmatrix}}_{\mathbf{y}} \tag{3.27}$$

with $\mathbf{g}^j$ being the $j$th row of the geometric matrix $G$.

An important challenge related to the estimation of the velocity is its dependence on the knowledge of the receiver position. This dependence introduces cross-correlations into the velocity measurement errors. With the purpose of overpassing this correlation, Kelly [25] proposed an algorithm for the correction estimation of the velocity:

1. Given the geometry matrix $G$ and the covariance matrix of the position solution (position and clock offset rate) $P$ from 3.15, it is estimated the values for the covariance only of the position as:

$$R_{\mathbf{p}} = J_3 \, P \, J_3^T, \quad \text{where } J_3 = \begin{bmatrix} 1 & 0 & 0 & 0 \\ 0 & 1 & 0 & 0 \\ 0 & 0 & 1 & 0 \end{bmatrix} \tag{3.28}$$

2. Then the calculation the matrix $D$, as:

$$D = \begin{bmatrix} \mathbf{d}^{1T} \\ \vdots \\ \mathbf{d}^{nT} \end{bmatrix}, \quad \text{where } \mathbf{d}^j = -\frac{\mathbf{v}^j}{R^j - D^j} + \left(\mathbf{p}^j - \mathbf{p}\right) \cdot \rho^j / (R^j - D^j)^2 \tag{3.29}$$

3. Calculate the covariance of the velocity residuals $R_{\mathbf{v}}$ using the covariance matrix of the position $R_{\mathbf{p}}$ and the pseudorange rates:

$$R_{\mathbf{v}} = D \, R_{\mathbf{p}} \, D^T + \sigma_{\dot{\rho}}^2 \, I \tag{3.30}$$

4. Estimate the pseudo-inverse of the measurement matrix:

$$G^{\dagger} = \left(G^T R_{\mathbf{v}} G\right)^{-1} G^T R_{\mathbf{v}}^{-1} \tag{3.31}$$

5. Final estimation of receiver's velocity and clock offset rate by taking into account the correlation with the position uncertainty:

$$\begin{bmatrix} \mathbf{v} \\ c\dot{\delta}t \end{bmatrix} = G^{\dagger} \cdot \begin{bmatrix} \mathbf{g}^1 \cdot \begin{bmatrix} \mathbf{v}^1 \\ 0 \end{bmatrix} - \dot{\rho}^1 \\ \vdots \\ \mathbf{g}^n \cdot \begin{bmatrix} \mathbf{v}^n \\ 0 \end{bmatrix} - \dot{\rho}^n \end{bmatrix} \tag{3.32}$$

## 3.6 Attitude Determination

GNSS Compass is the mechanism to estimate the attitude of a vehicle or target based on having three spatially distributed GNSS antennas. As represented in figure 3.14, with a vehicle equipped with two or more GNSS receivers, it is possible to use the information from the estimated position solutions to obtain the host vehicle's attitude. Attitude determination has been a recurrent problem in spacecraft systems, where the two vectors are typically the unit vector to the Sun and the Earth's magnetic field vector for coarse "sun-mag" attitude determination or unit vectors to two stars tracked by two star trackers for fine attitude determination [37].

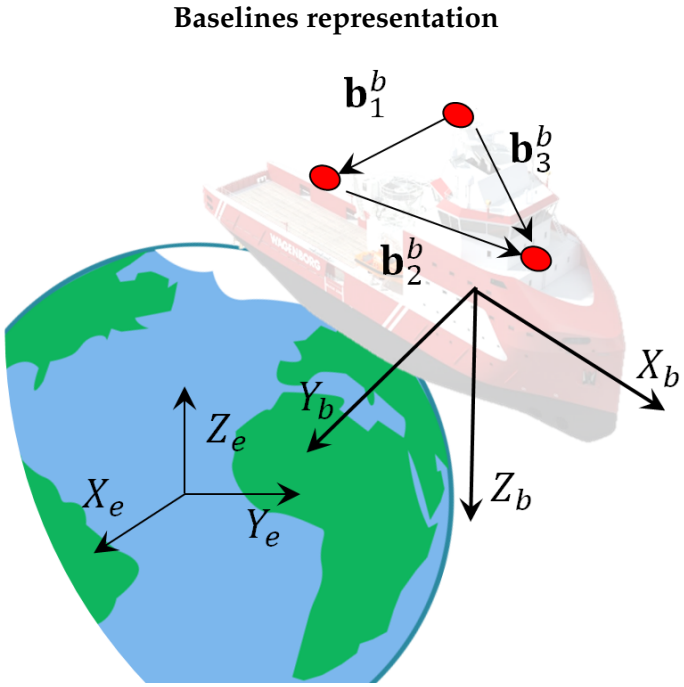


FIGURE 3.14: GNSS compass arrangement with 3x GNSS antennas for attitude determination: the baseline $\mathbf{b}_i^b$ defines the vector with the position differences between the antennas for the body frame. With the estimation of the antennas' position using satellite navigation, it is constructed the baselines in the ECEF frame $\mathbf{b}_i^e$.

Most of the algorithms for estimating attitude from vector measurements look for the miminization of the loss function proposed by Grace Wahba [66] in 1965:

$$J(R) = \frac{1}{2}\sum_{k=1}^{N} w_k \|\mathbf{b}_k^e - R_b^e\, \mathbf{b}_k^b\|^2 \tag{3.33}$$

where $\{w_k\}$ are non-negative weights, $N$ is the number observations (normally mapped to the number of GNSS receivers) and $\mathbf{b}_k^b, \mathbf{b}_k^e$ are the baselines representing the unit vectors defining the directions between the receivers positions in the body and ECEF coordinate frames respectively. Such baselines are defined as:

$$\mathbf{b}_{ij} = \frac{\mathbf{p}_i - \mathbf{p}_j}{\|\mathbf{p}_i - \mathbf{p}_j\|}, \quad \text{with } i, j = 1, \ldots, N, i \neq j \tag{3.34}$$

The attitude is determined by the rotation matrix $R_b^e$. The latter can then be transformed to another attitude representation, such as Euler angles or attitude quaternion.

With regards to the weights $\{w_k\}$, they can be defined in different ways. In [36], the weights are inverse variances, $a_k = \sigma_k^{-2}$, to relate Wahba's problem to Maximum Likelihood Estimation, while other authors [59] assume the weights to be normalized to unity. In this work, we follow the approach of the inverse covariances. There is always some errors in the position estimation, which is propagated to the baselines in form of angle, as can be seen in figure 3.15. The angular error $\delta\alpha$ can be estimated using geometry:

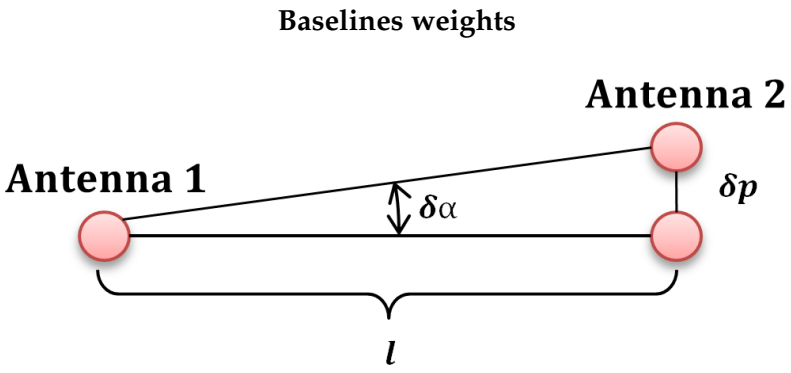


FIGURE 3.15: The weight assigned to the baseline corresponding to two antennas is proportional to the distance between them, as the closer they are to each other the higher the attitude error may result.

$$\sin(\delta\alpha) = \frac{\delta p}{\sqrt{l^2 + \delta p^2}}, \quad \text{as } l \gg \delta p \Longrightarrow \sin(\delta\alpha) = \frac{\delta p}{l} \tag{3.35}$$

Assuming that the angle $\delta\alpha$ is very small, one can approximate $\sin(\delta\alpha) \approx \delta\alpha$. Then, the standard deviation of the error is:

$$\sigma_\alpha = \delta\alpha \approx \frac{\delta p}{l} \tag{3.36}$$

As said previously, in this work it is followed the approach of considering the weights for the Wahba's problem as the inverse covariances. As the distance $l$ between antennas remains constant, while the position error $\delta p$ varies over time, it can be excluded to obtain:

$$w_i = \sigma^{-2} \simeq l^2 \tag{3.37}$$

There are several explicit algorithms designed to solve the attitude estimation problem. In general, one can distinguish between the geometry-based deterministic methods, such as *Triad* (Three-Axis Attitude Determination), and the statistical methods such as Davenport's $q$-method.

*Triad* consists on constructing two triads of orthonormal unit vectors using two of the available baselines (a pair of baselines per coordinate frame) [3]. This method seeks for the relationship between the vector observation in the body frame and the reference vector in the inertial frame $\mathbf{b}^e$, which under absence of the measurement noise, should strictly satisfy the following condition:

$$[\mathbf{t}_1^e \; \mathbf{t}_2^e \; \mathbf{t}_2^e] = R_b^e \left[\mathbf{t}_1^b \; \mathbf{t}_2^b \; \mathbf{t}_2^b\right] \tag{3.38}$$

The triads are built from the two of the baselines of the system (only from two to assure the orthogonality of the resulting triad) as:

$$\mathbf{t}_1^b = \mathbf{b}_1^b, \quad \mathbf{t}_1^e = \mathbf{b}_1^e \tag{3.39}$$

$$\mathbf{t}_2^b = \frac{\mathbf{b}_1^b \times \mathbf{b}_2^b}{|\mathbf{b}_1^b \times \mathbf{b}_2^b|}, \quad \mathbf{t}_2^e = \frac{\mathbf{b}_1^e \times \mathbf{b}_2^e}{|\mathbf{b}_1^e \times \mathbf{b}_2^e|} \tag{3.40}$$

$$\mathbf{t}_3^b = \mathbf{t}_1^b \times \mathbf{t}_2^b, \quad \mathbf{t}_3^e = \mathbf{t}_1^e \times \mathbf{t}_2^e \tag{3.41}$$

The attitude is determined by the rotation matrix $R_b^e$:

$$R_b^e = [\mathbf{t}_1^e\ \mathbf{t}_2^e\ \mathbf{t}_3^e]\ \left[\mathbf{t}_1^b\ \mathbf{t}_2^b\ \mathbf{t}_3^b\right]^T \tag{3.42}$$

Then, one can convert this rotation matrix to a more efficient format, such as Euler angles or quaternions. This method has the advantage of being relatively intuitive and computationally not demanding, but also it presents some clear drawbacks. If the assumption of noise free vector observations is violated, the obtained rotation matrix $R_b^e$ will not be a valid rotation matrix. On top of that, this method only makes use of two measurements (baselines), so information is wasted in case we have more than two receivers in the system setup.

Another well-known method is the Davenport's $q$-method [58], which is based on the minimization of the loss function $J(R)$ raised from Wahba's problem. One can expand the original problem as next:

$$J(R) = \frac{1}{2}\sum_{k=1}^{N} w_k \left(\mathbf{b}_k^e - R_b^e\,\mathbf{b}_k^b\right)^T \left(\mathbf{b}_k^e - R_b^e\,\mathbf{b}_k^b\right) \tag{3.43}$$

$$= \frac{1}{2}\sum_{k=1}^{N} w_k \left(\mathbf{b}_k^{eT}\mathbf{b}_k^e + \mathbf{b}_k^{bT}\mathbf{b}_k^b - 2\mathbf{b}_k^{eT} R_b^e\,\mathbf{b}_k^b\right) \tag{3.44}$$

As the baselines are normalized, the products $\mathbf{b}_k^{eT}\mathbf{b}_k^e$ and $\mathbf{b}_k^{bT}\mathbf{b}_k^b$ are equal to unity. The loss function $J(R)$ becomes:

$$J(R) = \sum_{k=1}^{N} w_k \left(1 - \mathbf{b}_k^{eT} R_b^e\,\mathbf{b}_k^b\right) \tag{3.45}$$

So minimizing $J(R)$ is equivalent to maximize $g(R) = \sum_{k=1}^{N} w_k \mathbf{b}_k^{eT} R_b^e\,\mathbf{b}_k^b$. It has been shown in [36] that the optimization problem can be rewritten as:

$$g(R) = \sum_{k=1}^{N} \mathrm{tr}\left(RB^T\right) \tag{3.46}$$

where tr denotes the trace operation, and $B$ is defined as:

$$B = \sum_{k=1}^{N} w_k \mathbf{b}_k^e \mathbf{b}_k^{bT} \tag{3.47}$$

Making use of the relation between rotation matrix and quaternion from equation A.42, Eq. 3.46 can be expressed in terms of quaternion instead of the rotation matrix. Even though quaternions have four parameters, using the constraint of unity norm $q^T q = 1$, the required parameters to three can be reduced to three, leading to:

$$g(q) = q^T K q \tag{3.48}$$

where $K$ is the Davenport's matrix

$$K = \begin{bmatrix} \sigma & Z^T \\ Z & S - \sigma I_{3\times 3} \end{bmatrix} \tag{3.49}$$

with $s = \text{tr}(B)$, and $S = B + B^T$. The determination of the optimal attitude is reduced to finding the quaternion that maximizes the bilinear form 3.48, and after differentiation one obtains that

$$Kq_{opt} = \lambda_{max} q_{opt} \tag{3.50}$$

where $q_{opt}$ is the eigenvector associated to the largest eigenvalue of the Davenport matrix $\lambda_{max}$.

There are other methods, but they mostly address the computational problems and numerical accuracy rather. More insight on the topic and information about them can be found in [46].

Chapter 4

# Inertial Navigation

An inertial navigation system (INS) is based on the dead-reckoning principle. Dead reckoning measures the change in position or the velocity and add it to the previous position in order to estimate the current position. As the speed or distance travelled measured belongs to the body coordinate frame (where the sensors are mounted), an INS requires to obtain the direction of travel in the reference frame. An INS is composed by an *inertial measurement unit* (IMU), which is a set of inertial sensors: three mutually orthogonal accelerometers and, aligned with these, three gyroscopes.

Accelerometers and gyroscopes are sensors to measure acceleration and angular rate respectively, and can be found in a wide variety based on their performance, size or cost - from $100,000$ € for IMUs used in aviation to the $50$ € IMUs used in the automotive industry and $< 5$ € for those used in consumer applications. They can also be classified depending on their operating principle. In case of gyroscopes, one can distinguish between fiber optic gyros (FOG), based on the interference of light to detect mechanical rotation; based on vibrations, such as the low-cost and relatively low-performance MEMS (micro electromechanical sensor); or based on the principle of the conservation of angular momentum with a vibrating mass (i.e., gyrocompass belong to this category). On the other hand, accelerometers' technology can be based on either pendulous and vibrating beams. In general, a higher performance comes with a higher price and size (even though MEMS sensors are fastly improving in price and size).

In a strapdown INS, the accelerometers are attached to the target and so aligned to the body frame. The attitude solution obtained from the angular rate measurements is then employed to rotate the acceleration into to navigation coordinate frame. Subsequently, a gravity model is used to compensate for the gravity effects. By integrating the acceleration and adding it to the previous velocity, one gets an update of the velocity. Finally, the process is repeated integrating the velocity in order to get the estimation of the position. The position and velocity for all INS and the heading for lower-grade systems must be initialized before the INS can compute a navigation solution, as can be seen in the basic scheme of an INS in the figure 4.1.

Gyroscopes measure angular rate, which is used by the navigation processor to maintain the INS's attitude solution. The accelerometers, however, measure specific force, which is the acceleration due to all forces except for gravity. In a strapdown INS, the accelerometers are aligned with the navigating body, so the attitude solution is used to transform the specific force measurement into the resolving coordinate frame used by the navigation processor. A gravity model is then used to obtain the acceleration from the specific force using

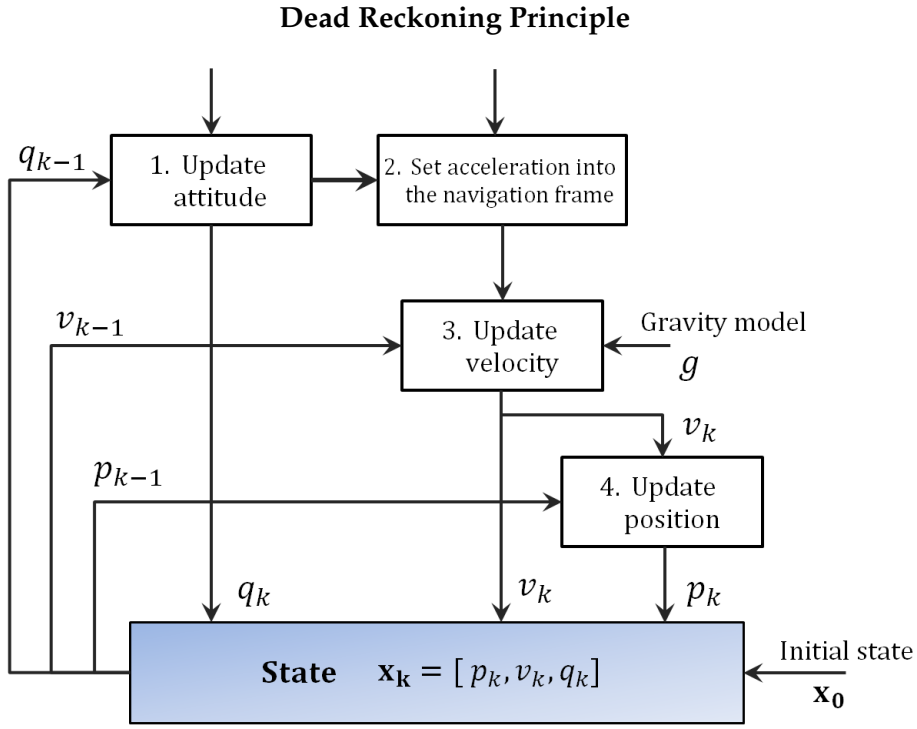


FIGURE 4.1: Basic scheme for an inertial navigation system based on dead reckoning.

the position solution. Integrating the acceleration produces the velocity solution, and integrating the velocity gives the position solution. The position and velocity for all INS and the heading for lower-grade systems must be initialized before the INS can compute a navigation solution.

### Attitude Determination

The estimation of the attitude is based on the integration of the angular rate $\omega^b_{t_k}$ read from the IMU unit. In this work, orientation is expressed using unit quaternions due to their multiple benefits compared to rotation matrices or Euler angles [29]. More information about quaternions, their use and operations can be found in Appendix A. The rotation is given by integrating the skew-symmetric matrix of the angular rate $\Omega(\omega)$:

$$\delta q_k = \int_{t_k}^{t_k+\Delta t} \frac{1}{2}\,\Omega(\omega^b_{t_k})\,dt \tag{4.1}$$

Note that the angular rates in the previous equation are corrected already for the bias and other minor effects such as Earth rotation rate. The update quaternion containing the orientation and the change from the body to the reference navigation frame (ECEF in this work) is given by:

$$q_k = \delta q_k \otimes q_{k-1} \tag{4.2}$$

### Velocity and Position Determination

Velocity is estimated as the addition of the previous velocity and the integration of the current acceleration. Once again, one faces the problem of not having the readouts from the

sensors in the navigation frame.

$$v_k^i = v_{k-1}^i + a_k^i \cdot \Delta t \tag{4.3}$$

The previously estimated quaternion is used to rotate the acceleration from the body to the navigation frame, and then it is necessary to compensate for the gravity effects:

$$a_k^i = q_{k-1} \otimes a_k^b \otimes q_{k-1}^* \; - \vec{g}^{\,i} \tag{4.4}$$

In this context, gravity is often estimated using a gravitational model, dependent on the estimated position. Given that the Earth is not a perfect sphere and the centrifugal effect of its rotation, Gravity distribution is not uniform. For instance, the gravitation effect is smaller along the Equator, where the radius of the Earth is longer, while the opposite happens in the poles.

For the gravity model in ECEF frame $\vec{g}^{\,i} = \left[g_x^i, g_y^i, g_z^i\right]$, in this work the following approximation is used:

$$g_x^i = -\frac{\mu x^i}{r^3}\left[1 - \frac{3}{2}J_2\left(\frac{R}{r}\right)^2\left(5\frac{\left(z^i\right)^2}{r^2} - 1\right)\right], \tag{4.5}$$

$$g_y^i = \frac{x^i}{y^i}g_x^i, \tag{4.6}$$

$$g_z^i = -\frac{\mu z^i}{r^3}\left[1 - \frac{3}{2}J_2\left(\frac{R}{r}\right)^2\left(5\frac{\left(z^i\right)^2}{r^2} - 1\right)\right], \tag{4.7}$$

where $r = \sqrt{(x)^2 + (y)^2 + (z)^2}$. In the expressions above $J_2 = 0.00108263$, $\mu = 398600.4418$ $km^3/s^2$ and $R = 6378.137$km are the corresponding parameters of the JGM-2 gravity field.

Finally, the position is updated by summing the integrating velocity and double integrating the acceleration to the previous estimated position:

$$p_k^i = p_{k-1}^i + v_{k-1}^i \cdot \Delta t + a_{k-1}^i \cdot \frac{\Delta t^2}{2} \tag{4.8}$$

For higher performance system, it would be necessary the use of more elaborated models which would include Coriolis effects or the Earth rotation.

## 4.1 Kalman Filtering

For applications such as tracking, in which noisy sensors create an uncertainty increasing over time, Bayes filters stands for being a great tool, dealing with the ambiguity in measurements and dynamic systems and they provide a probabilistic tool for estimation. Among Bayes filters, the Kalman filter stands out for being the most commonly used algorithm in navigation systems. Developed in 1960 by Rudolph Kalman and with the original purpose of solving the spacecraft navigation problem for the Apollo space program, KF has been applied in numerous fields such as demographic modelling, econometrics or neural network training.

In navigation systems, the Kalman filter (KF) constitutes the basis of the vast majority of estimation algorithms. It provides a smoothed navigation solution, integrates the measurements from noisy inertial sensors with GPS signals and other navigation sensors, and measures the uncertainty of the estimated solution, as it is shown as an example in figure 4.2.

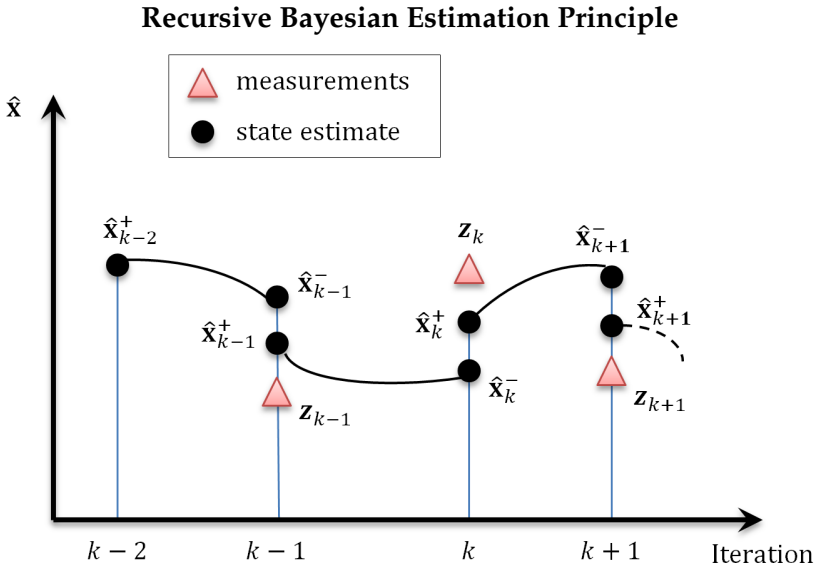


FIGURE 4.2: A simple example on the estimated state and new measurements are fused on the recursive bayesian estimation framework.

The algorithm recursively estimates a set of parameters - position, velocity, attitude, ... - denoted as state $\mathbf{x}_k$ of a dynamical system by minimizing the mean-squared estimation error given by noisy measurements. Under the assumption of white Gaussian noise, Kalman filter computes an optimal solution for a linear system and provides the uncertainty of the system in form of covariance matrix $P_k$. Kalman filter is a two steps prediction-correction method, as can be shown in 4.3:

**Prediction.** The equations of dynamic model project the predicted or *a priori* state $\hat{\mathbf{x}}_k^-$ ahead in time, from $t_{k-1}$ to $t_k$. Along with it, the prediction of the covariance $P_k^-$ is updated:

$$\hat{\mathbf{x}}_k^- = A\hat{\mathbf{x}}_{k-1}^+ + B\mathbf{u}_k \qquad P_k^- = AP_{k-1}^+A^T + Q_k \tag{4.9}$$

where $A$ and $B$ constitute the equations of the dynamical model, and $\mathbf{u}_k$ is the control input of the sensors. The noises of the measurements in the prediction model $\mathbf{v}_k$ are assumed to be independent, zero mean $E[\mathbf{v}_k\ \mathbf{v}_k] = 0$, and follow a normal distribution $\mathbf{v}_k \sim \mathcal{N}(0, Q_k)$.

**Correction.** The *a priori* state is corrected incorporating the actual measurements $\mathbf{z}_k$ and the observation or measurement model $H$. Of first place, the Kalman gain $\mathbf{K}_k$ is computed:

$$K_k = P_k^{-T}\left(H\ P_k^- H^T + R\right)^{-1} \tag{4.10}$$

where the noise of the observations $\nu_k$ are introduced in a similar way to the prediction step: $E[\nu_k\ \nu_k] = 0$, and follow a normal distribution $\nu_k \sim \mathcal{N}(0, R)$. The matrix $K_k$ is the gain that minimizes the a posteriori error covariance. The Kalman gain is proportional to the uncertainty in the state estimate and inversely proportional to the uncertainty of the measurements. In case the outputs of the sensors have a high uncertainty level and the state estimate is relatively accurate, the Kalman gain has little impact on the update of the state estimation, and the system matches the dynamic model. On the other hand, if the observations are highly reliable, the Kalman gain $K_k$ would have a big impact on the correction of the state. The *a posteriori* state $\hat{\mathbf{x}}_k^+$ and the error covariance $P_k^+$ are given by:

$$\hat{\mathbf{x}}_k^+ = \hat{\mathbf{x}}_k^- + K_k\left(\mathbf{z}_k - H\hat{\mathbf{x}}_k^-\right) \tag{4.11}$$

$$P_k^+ = (I - K_k H)\, P_k^- \tag{4.12}$$

The last equation can be ill-conditioned. As the filter converges, the cancelling of significant digits in $P_k^+$ can eventually lead to matrix asymmetry, or to a non-positive semi-definite matrix [46]. Thus, the Joseph form is often implemented as:

$$P_k^+ = (I - K_k H)\, P_k^- \,(I - K_k H)^T + K_k R K_k^T \tag{4.13}$$

which given its quadratic nature is obviously positive semi-definite.

Whenever the dynamical or the observation model is nonlinear, a different approach of the Kalman filter is applied to linearise about the current mean and covariance. Even though there are many approaches to overcome this issue, the two most widely spread versions of nonlinear KF are Extended Kalman filter (EKF) and Unscented Kalman filter (UKF), which will be described below.

### 4.1.1 Extended Kalman Filter

If the models are linear and the probabilities are Gaussian, the linear KF is an efficient and optimal solution of the estimation problem, following the well-known two steps prediction-correction structure depicted in figure 4.3. Unfortunately, most of the real-world systems are nonlinear and modifications to the linear KF (LKF) have been developed to deal with the nonlinear dynamics and/or measurement models. The extended KF (EKF) is one of the most popular nonlinear modifications of the LKF and is historically considered as a *de facto* standard within the engineering community. In EKF the nonlinear models are linearized about the current estimate using the Taylor series expansion.

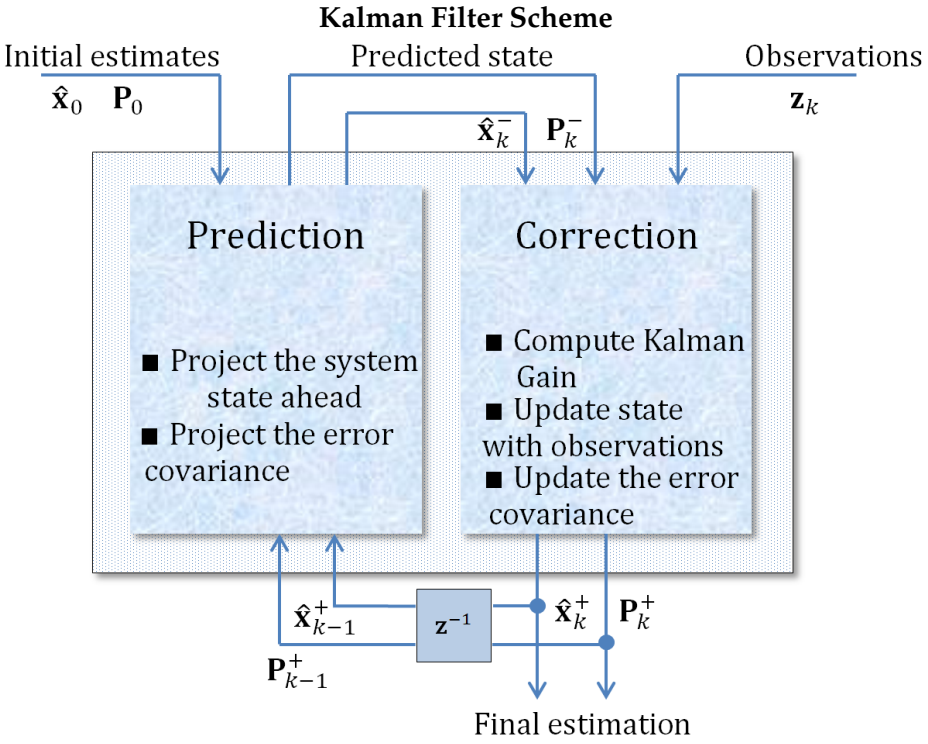


FIGURE 4.3: A prediction-correction structure of the classical Kalman filter algorithm.

In contrast to the classical linear Kalman filter, the EKF is neither the unbiased minimum mean-squared error estimator nor the minimum variance estimator of the state. Even more, the EKF is generally biased. However, the EKF is the best linear unbiased estimator of the

linearised dynamical system, which can often be a good approximation of the nonlinear system [21].

It is assumed that the process and measurement models are governed by the non-linear stochastic differential equations:

$$\mathbf{x}_k = f(\mathbf{x}_{k-1}, \mathbf{u}_k, \mathbf{v}_k), \tag{4.14}$$

$$\mathbf{z}_k = h(\mathbf{x}_{k-1}, \nu_k) \tag{4.15}$$

Such equations $f$ and $h$ can be formulated as a Taylor series expansion about the most recent estimated state, keeping only the first term and dropping the high order terms (HOT) as:

$$\mathbf{x}_k \approx \tilde{\mathbf{x}}_k J_{A,k}(\mathbf{x}_k - \hat{\mathbf{x}}^+_{k-1}) + J_{B,k}\mathbf{u}_k + J_{V,k}\mathbf{v}_k, \tag{4.16}$$

$$\mathbf{z}_k \approx \tilde{\mathbf{z}}_k + J_{H,k}(\mathbf{x}_k - \tilde{\mathbf{x}}) + J_{\nu,k}\nu_k \tag{4.17}$$

where $\mathbf{x}_k$ and $\mathbf{z}_k$ are the actual state and measurement vectors, $\tilde{\mathbf{x}}_k$ and $\tilde{\mathbf{z}}_k$ are the approximate state and measurement vectors and the Jacobians are computed as:

- $J_{A,k}$ is the Jacobian matrix of partial derivatives of the process model $f$ about the state $\mathbf{x}$:

$$J_{A,k} = \frac{\partial f}{\partial \mathbf{x}}\Big|_{\hat{\mathbf{x}}^+_{k-1}, \mathbf{u}_k, 0} \tag{4.18}$$

- $J_B$ is the Jacobian matrix of partial derivatives of $f$ with respect to $\mathbf{u}$:

$$J_{B,k} = \frac{\partial f}{\partial \mathbf{u}}\Big|_{\hat{\mathbf{x}}^+_{k-1}, \mathbf{u}_k, 0} \tag{4.19}$$

- $J_V$ is the Jacobian matrix of partial derivatives of $f$ with respect to the process model noise $\mathbf{v}$:

$$J_{V,k} = \frac{\partial f}{\partial \mathbf{v}}\Big|_{\hat{\mathbf{x}}^+_{k-1}, \mathbf{u}_k, 0} \tag{4.20}$$

- $J_H$ is the Jacobian matrix of partial derivatives of the measurement model $h$ with respect to the state:

$$J_{H,k} = \frac{\partial h}{\partial \mathbf{x}}\Big|_{\hat{\mathbf{x}}^-_k, 0} \tag{4.21}$$

- $J_H$ is the Jacobian matrix of partial derivatives of the measurement model $h$ with respect to the measurement noise:

$$J_{\nu,k} = \frac{\partial h}{\partial \nu}\Big|_{\hat{\mathbf{x}}^-_k, 0} \tag{4.22}$$

The procedure from EKF follows the two step prediction-correction. Firstly, the state is time updated by propagating it through the process model:

$$\hat{\mathbf{x}}^-_k = f\left(\hat{\mathbf{x}}^+_{k-1}, \mathbf{u}_k, 0\right) \tag{4.23}$$

projecting the covariance with the Jacobian of the matrices. Normally, the control and the process noises are considered as a combined process model as:

$$P^-_k = J_{A,k}\, P^+_{k-1} J^T_{A,k} + J_{V,k}\, Q_K\, J_{V,k} \tag{4.24}$$

The computation of the Kalman gain is made as follows:

$$K_k = P_k^- J_{H,k}^T \left( J_{H,k} P_k^- J_{H,k}^T + J_{\nu,k} R_k J_{\nu,k}^T \right)^{-1} \tag{4.25}$$

The state is then updated with the measurements and the Kalman gain:

$$\hat{\mathbf{x}}_k^+ = \hat{\mathbf{x}}_k^- + K_k \left( \mathbf{z}_k - h(\hat{\mathbf{x}}_k^-, 0) \right) \tag{4.26}$$

with the associated covariance of the state given by:

$$P_k^+ = (I - K_k J_{H,k}) P_k^- \tag{4.27}$$

Although the EKF inherits many advantages of the LKF such as limited computational costs and clear filtering structure, the performance of the estimator strongly depends on the validity of the linearized model assumption and the filter can become inaccurate or even unstable if these assumptions are violated [13].

### 4.1.2 Unscented Kalman Filter

Despite EKF being considered the standard approach for tracking and other nonlinear estimation problems, it holds some well-known drawbacks:

1. The provided solution is only reliable for those systems that are almost linear on the time scale of the update intervals (e.g. integration time within the inertial mechanization).

2. Linearisation can produce highly unstable filters if the assumptions of local linearity are violated.

3. The derivation of the Jacobian matrices are nontrivial in most applications and often lead to significant implementation difficulties. As well as, EKF could have some problems with functional dependencies which are not differentiable (i.e., dependencies given as generating rules).

The UKF, which is a derivative-free alternative to EKF, overcomes the nonlinearity problem by using a deterministic sampling approach. It is *founded on the intuition that it is easier to approximate a probability distribution that it is to approximate an arbitrary nonlinear function or transformation* [23]. The state distribution is represented using a minimal set of carefully chosen sample points, called *sigma points*, which are propagated through the original nonlinear functions for the process and measurement models. Although this method bares a superficial resemblance to Monte Carlo-type methods, there is a fundamental difference: the samples are not drawn at random but rather according to a specific, deterministic algorithm [63]. The mean and covariance of the state are then reconstructed back from the sigma points, as can be seen in the figure 4.4.

The basic algorithm for UKF is explained next Alg. 1, adapted from [46]:

**Algorithm 1** Unscented Kalman Filter

Initialization:
$\hat{\mathbf{x}}_0 = E[x_0]$, $P_0^+ = E\left[(x_0 - \hat{\mathbf{x}}_0)(x_0 - \hat{\mathbf{x}}_0)^T\right]$, $v_k \sim \mathcal{N}(0, Q_k)$, $\nu_k \sim \mathcal{N}(0, R_k)$.

For $k = 1, \ldots, \infty$ :

1. Calculate $\sigma$-points:

$$\mathcal{X}_k \equiv \begin{cases} \hat{\mathbf{x}}_{k-1}^+ \\ \hat{\mathbf{x}}_{k-1}^+ + \gamma\sqrt{P_{k-1}^+} \\ \hat{\mathbf{x}}_{k-1}^+ - \gamma\sqrt{P_{k-1}^+} \end{cases} \tag{4.28}$$

2. Time-update with the nonlinear function $f$ of the process model:

$$\mathcal{X}_k^- = f(\mathcal{X}_{k-1}^+, u_k), \tag{4.29}$$

$$\hat{\mathbf{x}}_k^- = \sum_{i=0}^{2n} w_m^{[i]} \mathcal{X}_k^{-,[i]}, \tag{4.30}$$

$$\mathbf{P}_k^- = \sum_{i=0}^{2n} w_c^{[i]} \left(\mathcal{X}_k^{-,[i]} - \hat{\mathbf{x}}_k^-\right)\left(\mathcal{X}_k^{-,[i]} - \hat{\mathbf{x}}_k^-\right)^T + Q_k, \tag{4.31}$$

where the notation $(\cdot)^{[i]}$ - means $i$-th column of the matrix.

3. Recalculate $\sigma$-points about the predicted state $\hat{\mathbf{x}}_k^-$

$$\mathcal{X}_k^- = \left[\begin{array}{ccc} \hat{\mathbf{x}}_k^- & \hat{\mathbf{x}}_k^- + \gamma\sqrt{P_k^-} & \hat{\mathbf{x}}_k^- - \gamma\sqrt{P_k^-} \end{array}\right], \tag{4.32}$$

4. Measurement update equations with the measurement model $h$:

$$\mathcal{Z}_k = h\left(\mathcal{X}_k^-\right), \tag{4.33}$$

$$\hat{\mathbf{z}}_k = \sum_{i=0}^{2n} w_m^{[i]} \mathcal{Z}_k^{[i]}, \tag{4.34}$$

$$P_{zz,k} = \sum_{i=0}^{2n} w_c^{[i]} \left(\mathcal{Z}_k^{[i]} - \hat{\mathbf{z}}_k\right)\left(\mathcal{Z}_k^{[i]} - \hat{\mathbf{z}}_k\right)^T + R, \tag{4.35}$$

$$P_{xz,k} = \sum_{i=0}^{2n} w_c^{[i]} \left(\mathcal{X}_k^{-,[i]} - \hat{\mathbf{x}}_k^-\right)\left(\mathcal{Z}_k^{[i]} - \hat{\mathbf{z}}_k\right)^T, \tag{4.36}$$

$$K_k = P_{xz,k}\, P_{zz,k}^{-1}, \tag{4.37}$$

$$\hat{\mathbf{x}}_k^+ = \hat{\mathbf{x}}_k^- + K_k\left(\mathbf{z}_k - \hat{\mathbf{z}}_k\right), \tag{4.38}$$

$$P_k^+ = P_k^- - K_k P_{zz,k} K_k^T. \tag{4.39}$$

In the expressions above the parameter $\gamma = \sqrt{n + \lambda}$ and the corresponding weights are:

$$w_m^{[0]} = \frac{\lambda}{n + \lambda}, \tag{4.40}$$

$$w_c^{[0]} = \frac{\lambda}{n + \lambda} + \left(1 - \alpha^2 + \beta\right), \tag{4.41}$$

$$w_m^{[i]} = w_c^{[i]} = \frac{1}{2(n + \lambda)}, \tag{4.42}$$

for $i = 1, \ldots, 2n$, $\lambda = \alpha^2(n + \kappa) - n$ being the compound scaling parameter, $0 < \alpha \leq 1$ being the primary scaling parameter that determines how far the $\sigma$-points are spread from the mean, and $\beta$ is the secondary scaling factor used to emphasize the weighting on the zeroth $\sigma$-point for the posterior covariance calculation and can be used to minimize certain higher-order error terms based on known moments of the prior random variable. For Gaussian priors $\beta = 2$ is optimal. The tertiary scaling factor $\kappa$ is usually set to 0. Note that in general the optimal values of these parameters are problem specific. Finally $\sqrt{\cdot}$ is the matrix square-root using lower triangular Cholesky decomposition and $n$ is the dimension of the original state vector $x_k$.

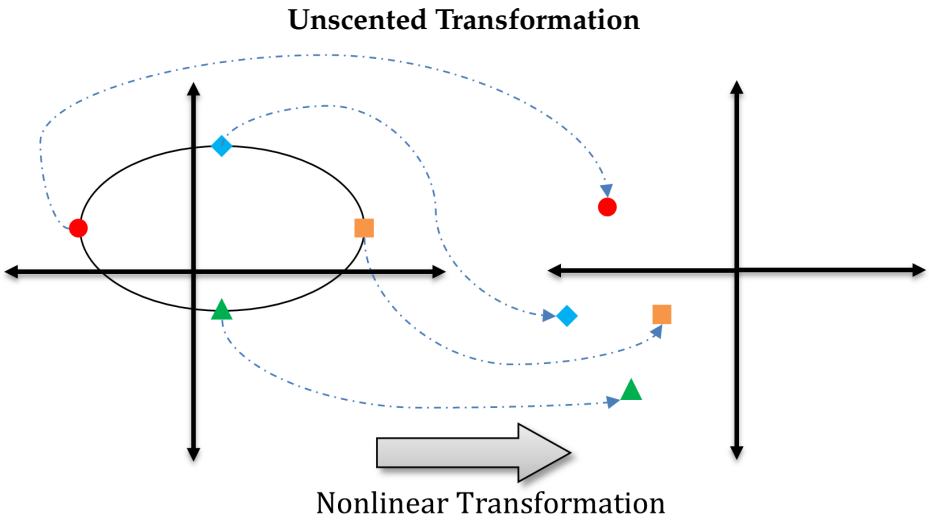


FIGURE 4.4: The principle of the unscented transformation.

Chapter 5

# Robust Estimation

GNSS positioning problems are generally solved by applying least squares estimation and Kalman filtering techniques, as discussed in the previous sections of this work. In order to perform optimally, these methods work under the assumption that the noises of the system are Gaussian. Despite this being justified under regular conditions, real measurements often contain unexpectedly large errors, which do not fit to the assumption of the Gaussianity of the noise. In GNSS, the source of this kind of errors is very diverse: multipath and reflection of the signals are two very common problems in urban scenarios, where building are responsible for non-line-of-sights and shadowing; also atmospheric phenomena, such as ionospheric storms, influence the coverage and quality of the radio signals. Before digging into the topic, it is important to provide the definition of some key terms:

- *Residuals* $r$ are defined as the difference between the estimated values of the observations and the corresponding measured values:

$$r = \mathbf{y} - G\mathbf{x} \tag{5.1}$$

  where **y**, **G** and **x** are defined in 3.8 and represent the difference between the pseudorange and the distance from the receiver and the corresponding satellite, for the case of code-based positioning.

- *Outliers* are observations that appear unusually large or small and "out of place" when compared with the rest of the data values of the set.

- *Breakdown point* $\epsilon^*$ is the smallest percentage of contaminated data that can cause the estimator take on arbitrarily large aberrant values [51].

- *Redundancy* $n - p$ is the difference between the number of available measurements $n$ and the amount of unknowns $p$ of the system.

- *Cost or objective function*, it is the function that seeks minimizing the residuals (e.g., in the least squares regression, the objective function is minimize $\sum_{i=1}^{n} r_i^2$ ).

- *Gaussian Efficiency*, also called *asymptotic efficiency*, refers to the similarity of the performance of a method with the classical least squares under Gaussian conditions.

The classical least squares method used for positioning consists of minimizing the sum of the squared residuals. This technique is quite sensitive to *outliers*, as one single outlier can drive to aberrant gross errors in the estimation solution [51]. In Fig. 5.1, one can find an example of much classical LS is affected by outliers in a linear regression problem proposed

by [50]. Overpassing these limitations of the LS for regression has been a concern for mathematicians and engineers for years. Initially, many authors proposed robust alternatives to the LS by changing the cost function, i.e., Edgeworth [8] introduced the *least absolute values* or *L1* criterion as:

$$\min \sum_{i=1}^{n} |r_i| \tag{5.2}$$

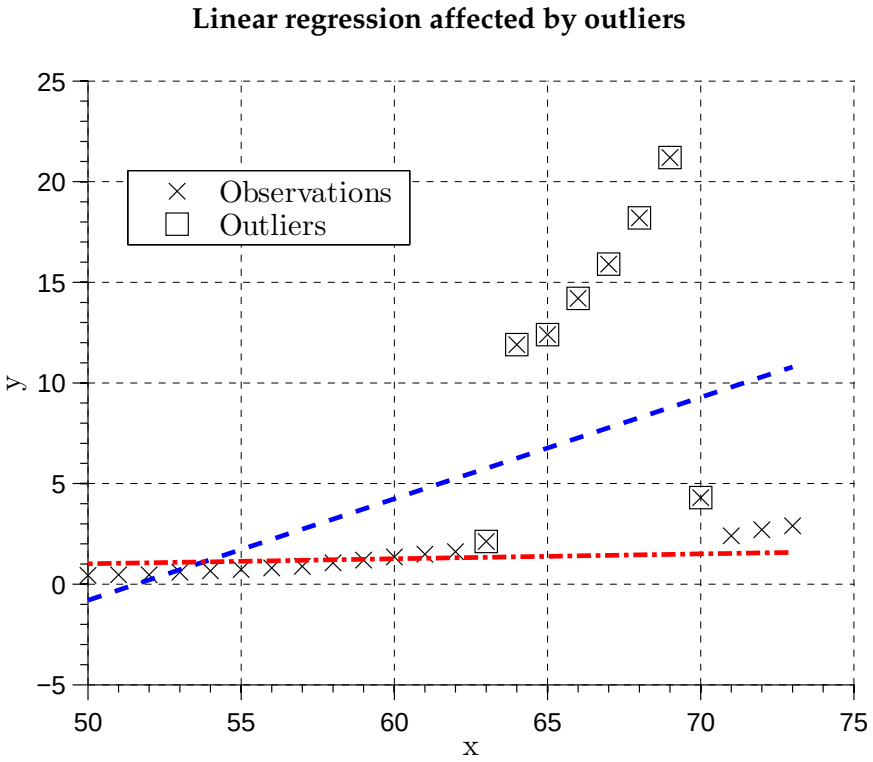


FIGURE 5.1: Least squares solution for a linear regression problem. The blue line represents the solution using the whole set of observations, while for the red line solution the outliers are removed.

Despite the *L1* criterion offering some additional protection against outlying observations, this regression methods yields the same breakdown point $\epsilon^*$ as a classical LS. There are different ways to classify the robust methods that we will present hereafter, however we find that for our application (exclude and/or mitigate the effects of faulty satellite pseudoranges) the most convenient classification for robust methods is based on to their implementation: iteratively reweighted least squares (IRLS) and best subset selection.

Those methods whose implementation is based on the IRLS, use the whole set of observations to compute a solution for the position problem. Then, the cost functions of the different robust methods make use of the residuals observations to weight them. This way, observations having large residuals will get downweighted and the other way around for observations with very small residuals. According to [43], the IRLS algorithm has only first degree convergence and needs a good initial estimate to have a fast convergence. However, these methods are also appealing due to the simplicity of the implementation and its likelihood with the regular LS algorithm.

On the other hand, we have the "*Best subset selection*" group of algorithms. In this case, from the available $n$ measurements it will be made $k = \binom{n}{p} = \frac{n!}{p!(n-p)!}$ subsets, where $p$ represents the number of unknowns (in our case $p = 4$, 3-dimensional position/velocity and clock offset/clock offset rate). We can estimate a solution from the combination of $p$ observations of each of the $k$ subsets, and from the said solutions we obtain the residuals.The

**Algorithm 2** IRLS algorithm

Set initial estimate of the solution (position and clockoffset rate) $\mathbf{x}$
Set error tolerance $\epsilon$ and the maximum number of iterations $N$
**for** $k := 1, 2, \ldots N$ **do**
    $r = \mathbf{y} - G\,\mathbf{x}^{(k-1)}$
    $w_i = \psi\left(r_i/\hat{\sigma}\right) / \left(r_i/\hat{\sigma}\right)$
    $W = \text{diag}\left[w_1, \ldots, w_n\right]$
    $\mathbf{x}^{(k)} = \left(G^T W G\right)^{-1} G^T W \mathbf{y}$
    **if** $\|\mathbf{x}^{(k)} - \mathbf{x}^{(k-1)}\| < \epsilon$ **then**
        Stop
    **end if**
**end for**

residuals are only associated to the $m - n$ measurements which did not take part in the solution, judging the quality of the solution with external observations. Finally, we select as the best solution the one whose residuals minimize the cost function of the corresponding robust method.

## 5.1 M - Estimation

After the proposal of least absolute values, the next step in the direction of robust estimation was made by Huber in 1973, with his *M estimator*. The basic idea would be to replace from the minimization cost the sum of the residuals to the square $r_i^2$ by $\rho(r_i)$. $\rho$ is an even - symmetric about the y-axis - function with an unique minimum at zero:

$$\min \sum_{i=1}^{n} \rho\left(\frac{r_i}{\hat{\sigma}}\right) \tag{5.3}$$

As it can be seen in the cost function, the M estimator is not invariant with respect to a magnification of the error scale. Therefore, the scale parameter has to be calculated simultaneously as:

$$\sum_{i=1}^{n} \psi(r_i/\hat{\sigma})\mathbf{x} = 0 \tag{5.4}$$

$$\sum_{i=1}^{n} \chi(r_i/\hat{\sigma}) = 0 \tag{5.5}$$

Finding the simultaneous solution of this system of equations is not trivial, and in practice one uses an iteration scheme based on reweighted least squares [51], as it is described in 2. In the previous equations, $\psi$ is the derivative of $\rho$ and $\chi$ is a symmetric function. The scale $\hat{\sigma}$ is a previously known or estimated parameter. Rousseeuw [52] makes an intensive discussion on different alternatives that could be used as this scale factor, however the most commonly used is the *Median Absolute Deviation* (MAD):

$$\hat{\sigma} \equiv MAD = 1.48\text{med}\left(|\mathbf{r} - \text{med}(\mathbf{r})|\right) \tag{5.6}$$

There have been several different proposals for the $\rho$ function. The original $\rho$ function, also called "Huber function", was monotone and based on the idea of using absolute residuals instead of squared residuals when the residuals are large. This function has a *tuning*

*parameter* $c$ which distinguishes small from large residuals: for residuals smaller than $c$, the ordinary LS is applied, while for residuals larger than $c$ the criterion becomes the $L1$ norm, as seen in the figure 5.2:

$$\rho(x) = \begin{cases} \frac{1}{2}x^2, & \text{if } |x| \leq c, \\ c\left(|x| - \frac{c}{2}\right), & \text{if } |x| > c \end{cases} \implies w_i = \begin{cases} 1, & \text{if } |r_i/\hat{\sigma}| < c \\ \frac{c\,\hat{\sigma}}{|r_i|}, & \text{if } |r_i/\hat{\sigma}| \geq c \end{cases} \tag{5.7}$$

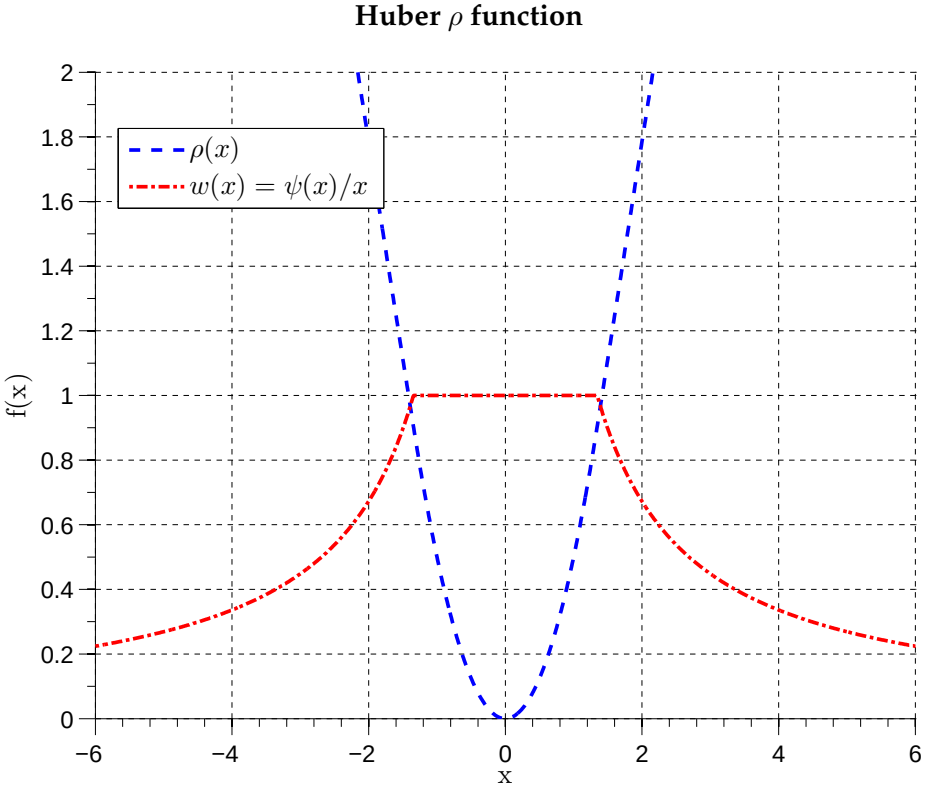


FIGURE 5.2: Huber $\rho$ function, tuning parameter $c = 1.345$.

It is noticeable that with this loss function, the weights are always between 0 and 1. A convenient property of the Huber function is that its derivative function $\psi$ is monotonic. This property implies that the Huber function is convex and therefore after the convergence of the algorithm the global minimum is reached [65]. The functions which were latter proposed are redescenders which are not convex, so the global minimum is not necessarily attained after convergence.

Tukey's bisquare function was another early proposal for the M-estimators [1]. As it happens with the Huber function, it consists of two parts: one part defines the function for the small residuals and the other is constant for the large residuals.

$$\rho(x) = \begin{cases} \frac{c^2}{6}\left(1 - \left(1 - \left(\frac{x}{c}\right)^2\right)^3\right), & \text{if } |x| \leq c, \\ 1/6\left(|x| - \frac{c}{2}\right), & \text{if } |x| > c \end{cases} \tag{5.8}$$

$$w_i = \begin{cases} \left(1 - \left(\frac{r_i}{\hat{\sigma}c}\right)^2\right)^2, & \text{if } |r_i/\hat{\sigma}| < c \\ 0, & \text{if } |r_i/\hat{\sigma}| \geq c \end{cases} \tag{5.9}$$

For residuals with absolute values larger than $c$ there is no further increase of the loss, so

the influence of the residuals is said to be bounded. For this property, Tukey's function is labelled as *hard redescending* function. The tuning parameter $c$ are used to adjust the efficiency of the resulting estimators for specific distribution [20]. The *bisquare* function is normally applied in M-estimation with a value $c = 4.685$ and also often used in S-estimation with a parameter $c = 1.548$.
Finally, it is presented another $\psi$-function for robust estimation, proposed by Welsh and receiving his name [20]. Being also redescender, Welsh function does not directly suppress the large residuals, as Tukey's function does, but instead it heavily downweights observations with large residuals using a negative exponential function, as can be seen in the figures for the respective $\rho$ functions in 5.3 and 5.4. Contrary to the other two functions previously presented, Welsh does not consist of two parts:

$$\rho(x) = \frac{c^2}{6}\left[1 - \exp\left(-\left(\frac{x}{c}\right)^2\right)\right] \tag{5.10}$$

$$w_i = \exp\left(-\left(\frac{r_i}{c\hat{\sigma}}\right)^2\right) \tag{5.11}$$

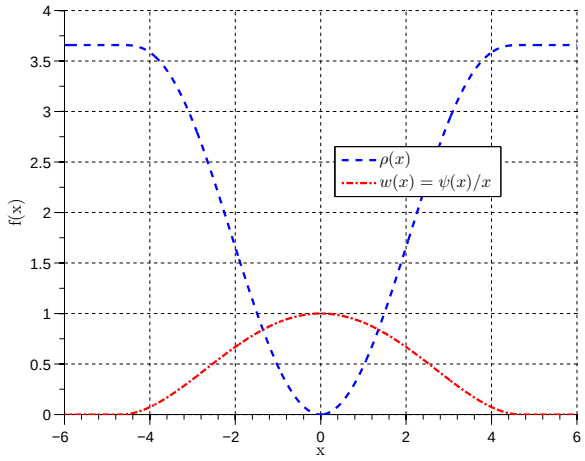


FIGURE 5.3: Tukey $\rho$ bisquare function, $c = 4.685$.

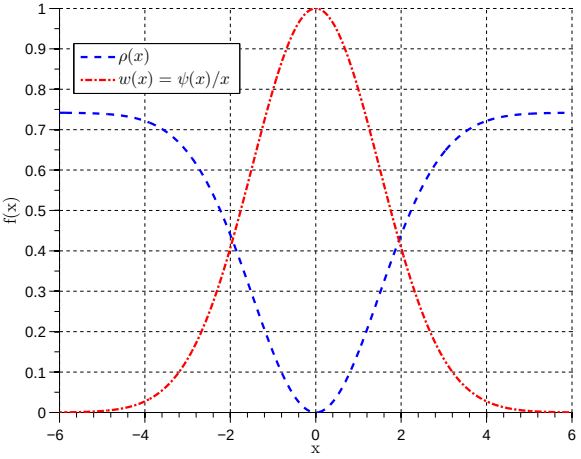


FIGURE 5.4: Welsh $\rho$ function, $c = 2.11$.

The tuning constant $c$ for the Welsh function is normally set to 2.11 for M-estimation and to 0.577 for the S-estimator, which will be presented later in this section.

Despite being statistically more efficient than $L1$ for models which assume the inclusion of Gaussian noise, the M-estimators presents a breakdown point $\epsilon^* = 0$, as it is not possible to include leverage of the measurements, which means it is not possible to augment the method to include the a priori measurement quality information such as the GNSS range measurement quality indicators.

## 5.2 GM - Estimation

When talking about measurements leverage, one refers to the *prior* knowledge about that one may have regarding the reliability of a measurement. In the area of application of this work, fusion of satellite and inertial positioning systems, the most usual way to leverage the observations is either based on the elevation of the satellite or on the carrier-to-noise ratio ($C/N_0$). $C/N_0$ is a measure of the signal strength and represents current signal power conditions. Despite not being a proper tool for outlier detection, the stronger a received signal has been proved to reduce the mean error of the estimated position in satellite navigation.

Due to the lack of measurements' leverage in the M-estimators, Mallows [35] proposed the *generalised M estimators* (GM-estimators). For that, he replaced equation 5.4 with:

$$\sum_{i=0}^{n} w(r_i)\psi\left(\frac{r_i}{\hat{\sigma}w(r_i)}\right) r_i = 0 \tag{5.12}$$

The leverage of the observations are based on their *reliability number* [28], a parameter which combines the *prior* knowledge of the measurement uncertainty with its influence on the geometry matrix of the solution $G$ as:

$$T = R^{-1} - G\left(G^T R G\right)^{-1} G^T \tag{5.13}$$

where $R = \text{diag}\left[\sigma_1^2, \ldots, \sigma_n^2\right]$ corresponds to the covariance matrix of the measurements. The matrix $T$ is denoted as cofactor matrix for various authors [32, 27], and it is used to determine the reliability number of each measurement:

$$\text{reliability}_i \equiv g_i = \left(\sqrt{T\,R}\right)_{ii} \tag{5.14}$$

where the indexing $(\cdot)_{ii}$ stands for the values of the diagonal matrix. The reliability number is only valid for GM-estimators when the observations are uncorrelated [27]. The weighting function that this method uses in the iteratively reweighted LS becomes:

$$w_i = \begin{cases} g_i, & \text{if } |r_i|/\hat{\sigma} g_i \leq c \\ g_i\, c\, \hat{\sigma}/|r_i|, & \text{if } |r_i|/\hat{\sigma} g_i > c \end{cases} \tag{5.15}$$

Despite incorporating measurements leverage, GM estimator yields a breakdown point $\epsilon^* = 1/(p+1)$, which is still not the highest possible. For our application, with $4$ unknowns to be estimated, this method is theoretically supposed to deal with a maximum of $20\%$ of contaminated data.

## 5.3 Least Median of Squares

Historically, most of the estimators proposed for robust regression consisted of replacing the square of the residuals from the original LS by another cost function. In 1984, Rousseeuw [51] proposed replacing the summation sign by a median, which can be considered as a robust statistic itself. The least median of squares (LMS) is represented as:

$$\min \text{med}\, r_i^2 \tag{5.16}$$

This estimator achieves a breakdown point $\epsilon^* = 0.50$. As a clear drawback, this method has a very low efficiency. This technique is based on the construction of subsets of $p$ parameters from the $n$ observations, and the use of the LS to obtain a solution from each of the subsets. Then, the estimated solutions are judged by observing how much they fit to the observations that were not used to get the aforementioned solutions, getting a total amount of $n - p$ residuals assigned to each of the subsets. The final estimated solution is that one whose median is the minimum among all the possible subsets.
Of course, the determination of $\binom{n}{p}$ solution requires an intensive computation power. For that reason, in [53] it is proposed to randomly select which subsets to use. In order to estimate the minimum number of randomly selected subsets that can represent the whole amount of possible combinations, $a$ as the probability that all selected observations in a subset are inliers which equals to the ratio $w$ between the number of inliers and the total amount of observations. Of course, this information is unknown, and it is a tuning parameter of the

LMS implementation. The minimum number of subsets $k$ is found as:

$$k = \frac{\log(1-a)}{\log\left(1-w^n\right)} \tag{5.17}$$

An important advantage presented in LMS is that the leverage of the measurements is possible, by applying a weighted LS as shown in equation 3.14, where the weight matrix $\mathbf{W} = R_k = \text{diag}\left[\sigma_{k,1}^2, \ldots, \sigma_{k,p}^2\right]$ is used to compute the solution for each subset.

In order to overpass the lack of efficiency of the LMS due to its convergence $n^{-1/3}$, Rousseeuw also proposed the **Least Trimmed Squares** (LTS), which has a convergence of $n^{-1/2}$. It is based on the minimization of the sum of the first quartile $h$ (or a bigger portion, up to $h = n/2$) of the residuals to the square:

$$\min \sum_{i=1}^{h} \left(r^2\right)_{i:n} \tag{5.18}$$

where $\left(r^2\right)_{1:n} \leq \cdots \leq \left(r^2\right)_{n:n}$ are the ordered squared residuals. The main disadvantage of the LTS compared to the LMS is that the objective function requires sorting the residuals, which takes $O(n \log n)$ operations compared to only $O(n)$ operations required for the median [51].

## 5.4 S - Estimation

The S estimation, proposed by Rousseeuw and Yohai [50], is based on residual scale. It is derived from a scale statistic in an implicit way:

$$\min \sigma(r_1, \ldots, r_n) \tag{5.19}$$

This method uses the residual standard deviation to overcome the weaknesses of median [60].

**Algorithm 3** S-estimator algorithm

1: Compute an initial solution **x** with a LS
2: Estimate the scale of the residuals as

$$\hat{\sigma}_i = \begin{cases} 1.48\text{med}\left(|r_i - \text{med}(r_i)|\right), & \text{iteration } = 1, \\ \sqrt{\frac{1}{nK}\sum_{i=1}^{n} w_i r_i^2}, & \text{iteration } > 1 \end{cases} \tag{5.20}$$

with $K = 0.20$.
3: Calculate $w_i$

$$w_i = \begin{cases} \begin{cases} \left(1 - \left(\frac{r_i}{c\hat{\sigma}_i}\right)^2\right)^2, & \text{if } |r_i/\hat{\sigma}_i| \leq c \\ 0, & \text{if } |r_i/\hat{\sigma}_i| > c \end{cases}, & \text{iteration} = 1, \\ \rho(r_i/\hat{\sigma}_i)\hat{\sigma}_i^2/r_i^2, & \text{iteration} > 1 \end{cases} \tag{5.21}$$

4: Calculate a new solution **x** with a weighted LS using the weights $w_i$ from the previous step
5: Repeat till convergence is reached

As it can be seen in algorithm 3, in step 3 we use a $\rho$ function, normally Tukey's bisquare presented previously and with a $c = 1.548$ parameter. This method is computationally much more efficient than the other high breakdown point methods, as it skips the estimation of the solution for the different randomly-selected subsets. As a drawback, this method has not the maximum breakdown point $\epsilon^* = 0.5$ as LMS or LTS. Instead, it is given by:

$$\epsilon^* = \left(\frac{n}{2} - p + 2\right)/n \tag{5.22}$$

In next Fig. 5.5, it is shown how the breakdown point evolves with the number of measurements for the application (with a minimum number of 5 measurements and with $p = 4$, as described before). In a typical scenario, there is an average of 10 to 12 visible satellites, the breakdown point of the S-estimator is relatively high ($\sim 33\%$). However, this method has a problem in common with the M-estimator which is that it is not possible to include leverage for the observations. To overcome this problem, the *Generalised* S estimator was presented in [6]. This algorithm shares the same procedure than the regular S-estimator, with the exception that the $\rho$ function and the initial weights are obtained using the reliability number of the measurements, in the same manner as in the GM estimation.


FIGURE 5.5: Evolution of the breakdown point of the S-estimator with the number of observations $n$.

## 5.5 Danish method

The Danish method was proposed by Krarup [30] and is purely heuristic with no rigorous statistical theory. Nonetheless, it became popular for some geodetic applications and has also received the attention from other areas, according to [31]. The method works by carrying out a least squares adjustment using the a priori weight matrix. Then the process is

repeated iteratively altering the weight matrix [27], as:

$$\sigma_i^2 = \sigma_{i,0}^2 \begin{cases} 1, & \text{if } \bar{w}_i/\hat{\sigma} \leq c \\ \exp\left(\bar{w}_i/\hat{\sigma}c\right), & \text{if } \bar{w}_i/\hat{\sigma} > c \end{cases} \tag{5.23}$$

where $\sigma_i^2$ is the a priori variance of the measured pseudorange (from the carrier-to-noise or elevation of the satellite model) and $\bar{w}_i$ is the absolute normalized residual using the cofactor matrix of the measurement presented in equation 5.13:

$$\bar{w}_i = \left| \frac{r_i}{\sqrt{T_{ii}}} \right| \tag{5.24}$$

The estimated $\sigma_i^2$ from 5.23 is set as the covariance matrix for the measurements, and can be integrated as the weight matrix to perform a weighted LS adjustment

$$W = P^{-1} = \text{diag}\left[\sigma_1^2, \ldots, \sigma_n^2\right] \tag{5.25}$$

The process continues until convergence is achieved. This way, outliers are given a low weight (due to the negative exponential function) and the size of the residuals represents the magnitude of the outlier. As discussed before, this method is not based on any formal statistic although it presents some likelihood to the GM-estimator in the way the weights are estimated. Although some authors [31] claim that the Danish method has a high breakdown point, this value is not specified.

## 5.6 RANdom SAmple Consensus

RANdom Sample Consensus (RANSAC), proposed initially by Fischler [10], is a robust method to estimate the parameters of a certain model starting from a set of data contaminated by large amounts of outliers [71]. Widely used for computer vision and image processing applications to smooth and interpret data, this algorithm also attracted the attention of several authors for GNSS positioning [5, 56].

In a similar manner as LMS or LTS, RANSAC generates subsets with the minimal number $p$ of observations to estimate solutions. After these solutions are generated, RANSAC proceeds to enlarge the number of observations for those subsets. To achieve this, the residuals corresponding to the non-used measurements are compared to a threshold: if a residual is below that threshold, it is labelled as an inlier for the corresponding subset, otherwise it is discarded. There have been different approaches to define the inlier test:

- In [5], the threshold corresponds to the abscissa value from the standard normal distribution with a $(1-\alpha)$ probability, where $\alpha$ is defined as the false alarm probability:

$$\text{if } |r_i| \leq \mathbf{n}_{1-\alpha}, \quad \text{observation}_i \Longleftarrow \text{inlier} \tag{5.26}$$

- In [56], the authors propose the use of a multiple $b$ (normally between 1 and 2.5) of the expected residual standard deviation $\sigma_{r_i}$. Thus, the variance of the residual is given by the sum of the variances of the position estimations and the pseudoranges as:

$$\sigma_{r_i} = \sqrt{g_i \left(G_k^T W_k G_k\right)^{-1} g_i^T + \sigma_i^2}, \tag{5.27}$$

$$\text{if } |r_i| \leq b\sigma_{r_i}, \quad \text{observation}_i \Longleftarrow \text{inlier} \tag{5.28}$$

where $g_i$ is the row corresponding to the geometry matrix of the $i$th observation, $G_k$ is the geometry matrix of the $k$th subset and $\sigma_i$ is the expected variance of the pseudorange of the $i$th observation. This way, the degree of discrepancy depends on both the expected noise deviation and the geometry of the subset.

Unlike LMS and LTS, the criterion used in RANSAC to select the best subset is not the minimization of any loss function, but the maximization of the number of inliers used in the final solution. Doing so, the best subset is the one whose solution fits to the largest amount of observations. Once one subset is selected as the best candidate, the final solution must be recalculated using all the observations considered as inliers within a classical LS adjustment.

Chapter 6

# Experimental Setup

This study was supported by the department of Nautical Systems, which is part of the Institute of Communication and Navigation of the German Aerospace Center (DLR) [7]. Thus, the algorithms studied in the previous Chapters were evaluated with respect to the challenges of maritime applications, such as inland waterways. Nevertheless, these algorithms are applicable to several positioning and navigation applications: automotive, pedestrian, aerospace, etc. Of course, depending on which auxiliary sensors are available.

With the aim of performing an automatic detection and mitigation of errors in satellite signals, the proposed algorithms are tested in two different scenarios. This chapter is devoted to describe the hardware setup for the vessels, as well as the challenges of each scenario. The following scenarios were selected for performance evaluation and testing:

**Maritime scenario: Port of Rostock.** This scenario is characterized by a very good availability and quality of the satellite signals, with an absence of large position errors due to the lack of multipath or NLOS effects affecting the satellite signals. This allows to have an accurate positioning, so the signals are artificially contaminated with random noise to study the performance of the robust techniques in well controlled conditions.

**Inland Waterway scenario: Moselle River.** This scenario covers a challenging track of a vessel on an inland waterway. This measurement campaign took place in the city of Koblenz, concretely on the inland waterway constituted by the Moselle River. During the test, the vessel had to pass three bridges twice, on her way out of and back in to the harbour. In combination with the high structures surrounding the shores of the river, these bridges lead to severe multipath effects in the satellite messages. For those reasons, this scenario results specially convenient to test the performance of the robust schemes.



## 6.1 Maritime Scenario: Port of Rostock

With multiple liner services, the seaport of Rostock is a core for international cargo traffic in the Baltic Sea, with over $60,000$ trailers and almost 2 billion tons cargo exchanged only in the last year [49]. This measurement campaign took place on the 01/09/2014 with the multi-purpose research and diving vessel BALTIC TAUCHER II (whose dimensions are 29 m length, beam 6.7m, draught 2.8 m and 146 tons of gross tonnage). The measurement campaign started with the vessel moored at its home port and lasted until the vessel left the Port of Rostock and entered the Baltic Sea, as can be seen in Fig. 6.1.

The sensor setup for the BALTIC TAUCHER II consisted of three dual frequency GPS antennas and receivers (Javad Delta), a tactical FOG, MEMS IMU, a Doppler Velocity Log (DVL) and a gyrocompass. The vessel and the location of the sensors is shown in figure 6.3.

FIGURE 6.1: Trajectory of the BALTIC TAUCHER II (approx. 15 minutes) recorded during the measurement campaign in Rostock.

During the evaluated time, only soft wind and minor waves were observed, so the motion of the vessel is not affected by atmospheric phenomenons. Out of the three antennas, the data received from the one in the center of the ship was used during the test of the algorithms. The DVL sensor, located on the bottom of the vessel, emits sound waves which are reflected at the bottom of the sea, and based on the Doppler effect, allows to estimate the velocity for the axis $x$ and $y$ of the body frame. There are several advantages to the use of this sensor, as it is self-contained and directly measures the velocity of the target. On the other hand, its accuracy is slowed down when the sea is at rough conditions, as well as for deep seas or oceans. In that case, the velocity of the current of the water is measured instead. Its working principle is illustrated in Fig. 6.2. The device sends out a 3-beam "ping" that measures the resulting response in terms of frequency shift (Doppler shift), which can then be translated as the velocity of the ground with respect to the transmitter. The velocity (for the 1D case) is obtained from:

$$f_d = \frac{2 f_t v \cos(\theta)}{c} \tag{6.1}$$

where $f_d$ is the Doppler frequency shift, $f_t$ is the transmitted frequency, $\theta$ is the angle of incidence with the ground, $c$ is the speed of sound in the water and $v$ is the velocity of the target.

In order to have an accurate ground truth as reference for the vessel trajectory, the technique Real Time Kinematics (RTK) positioning solution is used. RTK uses the carrier phase measurements and the transmission of corrections from a close base station and can provide accuracy of centimetre magnitude [45]. In this applicatino, the RTK solution has been obtained using the open source GNSS-processing software RTKLIB [62]. Note that this method can only be applied in the vicinity of a base station, but that requirement is fulfilled in the Port of Rostock.

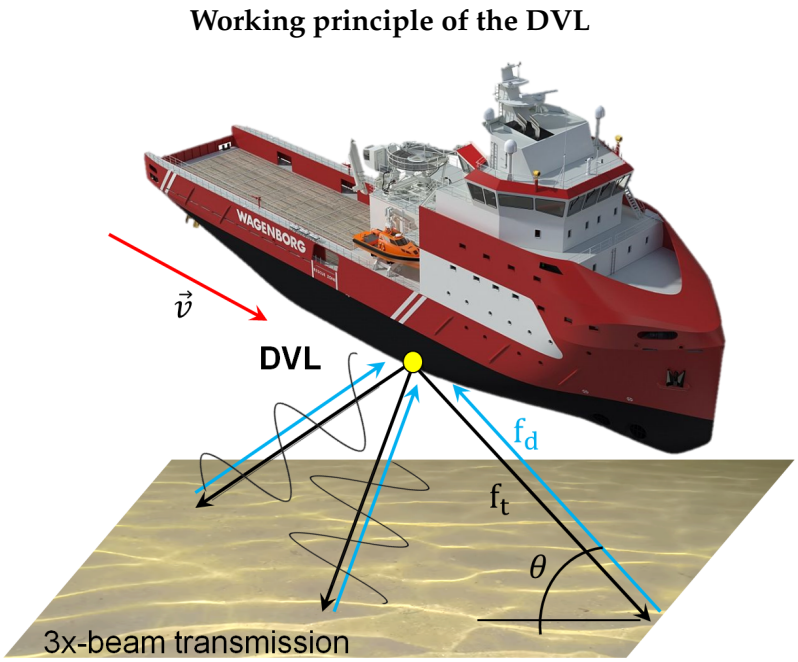


FIGURE 6.2: Working principle of the DVL: three beams are sent from to bottom of the vessel at a frequency $f_d$ and reflect back from the ground of the sea at a frequency $f_t$.


FIGURE 6.3: BALTIC TAUCHER II vessel. Red circles represent the position of the GPS antennas, while the yellow rectangle stands for the IMU placement. Image from [11].

In consequence to the perfect weather conditions and open sky, there is no motivation to test the robust methods in this scenario. However, due to such ideal conditions and the pseudoranges of the satellite being almost error-free[1], this scenario can be used as a text example to check the performance of the robust techniques against artificially added noise to the measurements. In order to do so, random noise is systematically added, following a normal standard distribution of different magnitudes to a given number of satellites: between one and three satellites will be affected. As most of the robust regression methods are proposed and tested for linear regression problems, this experiment will be used to evaluate the actual performance of different schemes for an actual GNSS positioning. Then, this evaluation will be cross-checked on the second scenario, where the radio signals from the satellites will be affected by actual multipath or NLOS effects.

## 6.2 Inland Waterway Scenario: Moselle River

The performance of the developed methods has also been evaluated using real observations from the measurement campaign conducted on 25th March 2014 (DOY 084, UTC 13:00-14.00) near Koblenz (Germany) on the Moselle river. The demonstration area covers several challenging scenarios for inland water navigation, as can be seen in Fig. 6.4. With approximately 11,500 ship passages in 2010, the Moselle river can be considered as one of the busiest waterways in Germany. Sailing downstream, a lock bounds the demonstration area 3km before the confluence with Rhine river [17]. After the lock, three bridges of different height and width span the river in a relatively short distance ('B' and 'C' in Fig. 6.4) of only 2km making a reliable and continuous positioning using pure GNSS information rather challenging. The first bridge starting from the West is a 4-lane car bridge "Europabruecke" with a width of 40 meters and clearance height of 13.9 meters. The next bridge is the railway bridge, which is 25 meters wide with a relatively low clearance of only 10.2 meters and oval clearance profile. The last one is the 'Balduinbruecke' with a width of 10 meters and a height of 12.1 meters and, therefore, is relatively small in comparison with the other two. The vessel travelled on an 8-shaped trajectory (total duration 1 hour) with several passes under the bridges and the lock ('A' in Fig 3) in order to ensure that the GNSS signals are strongly affected by the shadowing from bridges and buildings [17].

The sensor system onboard the vessel "MS Bingen" (see Fig 6.6) consisted of three geodetic GNSS antennas and receivers as well as a commercial FOG IMU. The setup of three GNSS antennas allows the system to determine the attitude of the vessels using the methods of GNSS compassing, where the baseline observations (max 3x) are used to constrain the attitude drift (this is only used in hybrid IMU/GNSS Kalman filter). The FOG IMU is used to bridge possible GNSS outages when used within a KF-based IMU/GNSS fusion, although true GNSS outages have not been observed as almost always at least four satellites have been visible. This is, probably, a result of the fact that the bridges can be still considered as relatively narrow objects and, thus the strength of some signals was not dropping below the acquisition threshold of the receiver. The availability of a higher performance IMU also allows to test a performance of an integrated IMU/GNSS solution, where the explicit dynamics assumptions of non-inertial KF are replaced by accurate tracking of the vessel motion using strapdown inertial mechanization. For the position performance analysis below only the data from the main GNSS antenna have been used (antenna in the center of the vessel), although some of the discussed robust methods can be easily scaled up to work with multiple antenna. The measurement rates are 2Hz for the GNSS receivers and 200Hz for the FOG IMU. Additionally, a Maritime Ground Based Augmentation System (MGBAS) station provided GPS code and phase corrections with 2 Hz update data for L1 and L2 frequencies. This data is employed to estimate an accurate post processed RTK. The ionosphere

[1] Maybe with the exception of some minor issues related to shadowing of the signals due to the mast.

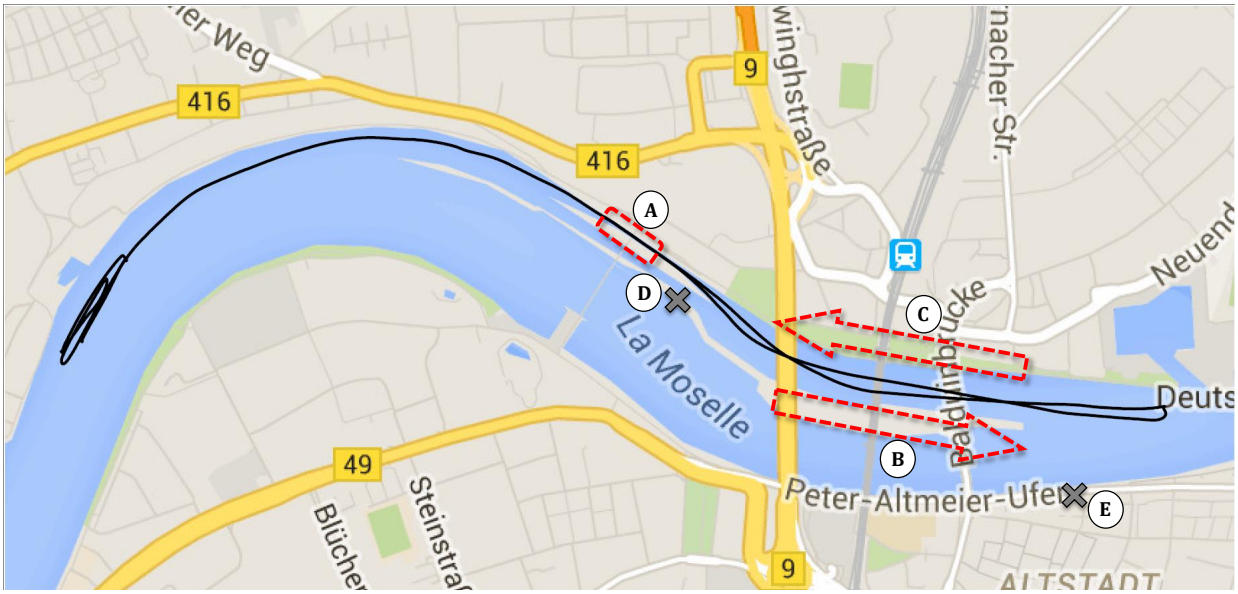


FIGURE 6.4: Measurement area on the river Moselle near Koblenz (Germany). Reference path (black line) and several challenging segments including the lock (A), and 3-bridge segments (B) and (C). Total trajectory duration - 1 hour.

propagation delay corrections have been applied using classical Klobuchar model and the corresponding troposphere delay corrections in order to provide the results representative of user equipment without ground-based correction information.

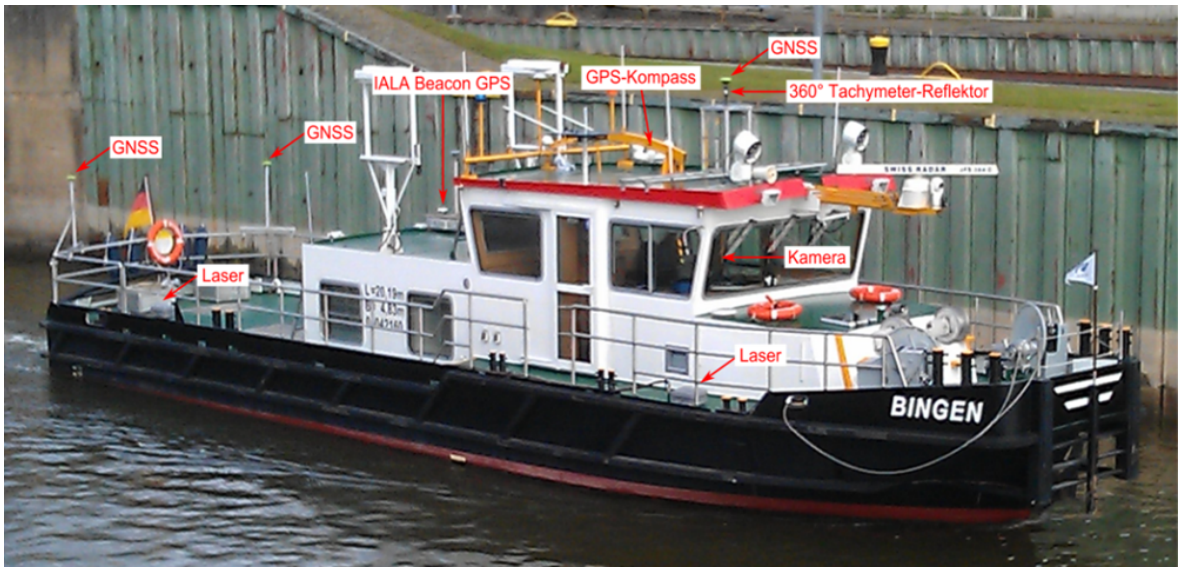


FIGURE 6.5: Research vessel "MS Bingen" used in the measurement campaign. The setup includes 3x GNSS antennas, IMU, IALA beacon GPS, IMU (not shown) and GPS compass. The total station reflector was used to produce the reference path.

In order to track accurately the position of the vessel independently from the GNSS information, two geodetic total stations have been placed on the shores of the river (see 'D' and 'E' in Fig. 6.4). As the total stations combine the use of angle and distance measurements in order to determine only the horizontal position, the vertical error accuracy is not addressed. The coordinates of the tracked object are given relative to a known reference point and are determined using trigonometry and triangulation as long as a direct LOS is

maintained between the two points. With the use of two total stations the availability of the reference trajectory is ensured even in the problematic areas where GNSS failed. After the reference 1Hz position information is obtained, the post-processing and adjustment of the measurements ensure an accuracy better than 2cm for the presented evaluation path. Note, that although the phase information is available for accurate position calculation, evaluation of the robust methods for phase-based GNSS positioning was out of the scope of this work. The RTK velocity solution was used as velocity reference, as from the total stations reference we could only extract a 2D velocity approximation.

### 6.2.1 Variance model for pseudorange observations

As was discussed previously, the weighted least squares adjustment is a well known and often used technique in satellite-based navigation. There are different variance models to leverage the quality of the observed pseudoranges. In this study, the performance of three of these models is compared. The method with the best performance will be applied as the weighting scheme for the rest of the work.

1. *Elevation-based measurement model*. It has been proven that the possible errors for the observed pseudoranges increase with low elevation satellites [67]. As the navigation message covers a longer distance through the ionospheric layer, it is deeply affected. On top of that, the signals are more likely to get reflected compared to the signal coming from a satellite with a high elevation. For this approach, two models are presented:

   - Classical approach (*Simple El* in Fig. 6.8), the variance of the $i$th measurement is inversely proportional to the sine of its elevation angle $\theta$:

   $$\sigma_i^2 = 1/\sin^2(\theta_i) \tag{6.2}$$

   - Variance model using elevation angle (*Groves El* in Fig. 6.8), suggested by Groves in [16]:

   $$\sigma_i = a + b \cdot \exp\left(-\theta_i/c\right) \tag{6.3}$$

   where $a = 0.13$, $b = 0.56$ and $c = 0.175$.

2. *Carrier-to-noise ratio based measurement model*. Carrier-to-noise ratio $C/N_0$ is a measure of signal strength and represents current signal power conditions independent of receiver implementation [31]. The model adopted is given by:

   $$\sigma_i^2 = a + b \cdot 10^{-\frac{C/N_0 - c}{10}} \tag{6.4}$$

   where the parameters are chosen according to the environment and the user equipment. In this study, the parameters have been found as $a = 0.60$, $b = 50.64$ and $c = 33.84$, which roughly fit to the receiver correlator noise baseline in a previous work [33].

In figure 6.7 we can see the skyplot of the satellites in line of sight during the one hour of measurement campaign in Moselle River. As expected, the signals from low elevation satellites have weak signal power and therefore low value for the $C/N_0$ values. On the other hand, the signals from satellites with a high elevation angle have a high value for the $C/N_0$ as well.

The three adaptive noise models were applied to a regular Single Point Positioning (SPP) using a Weighted Least Squares adjustment, as explained in Eq. 3.14. In Fig. 6.8 the cumulative distribution function (CDF) of the horizontal position error (HPE) of the SPP and a comparison of the previously presented methods is shown. All three models dramatically

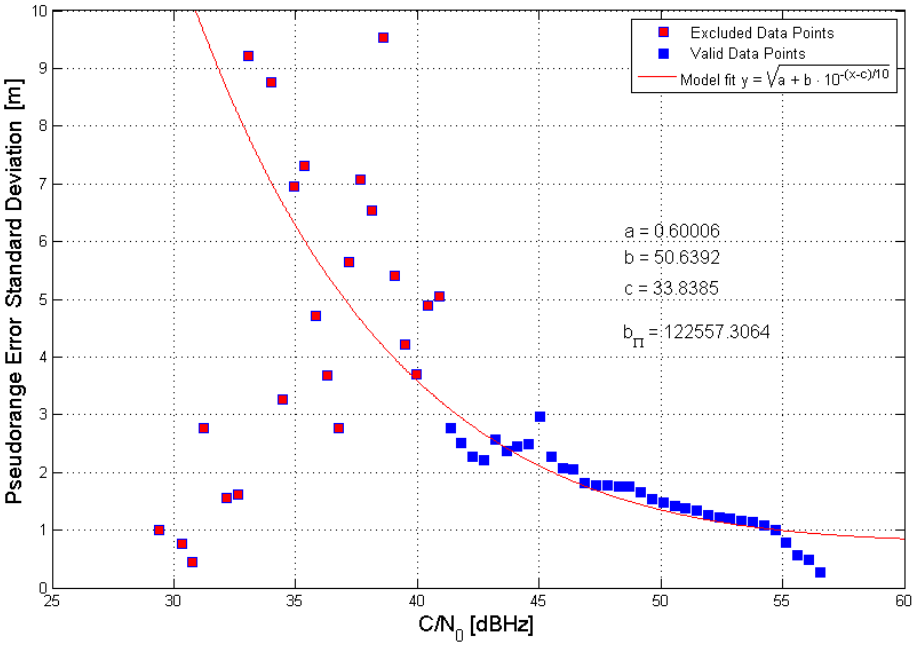


FIGURE 6.6: Experimental data for pseudorange noise model and model fit results. Image from [33]

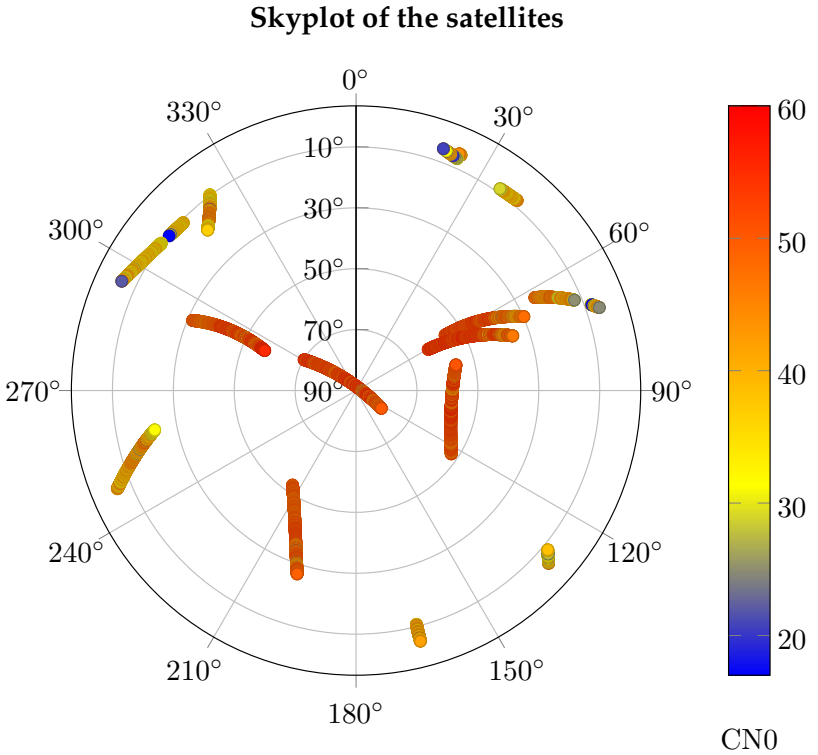


FIGURE 6.7: Skyplot for the Moselle River test scenario with the color encoding of the associated $C/N_0$ value.

reduce the mean horizontal error by at least one meter, compared to the non-weighted LS of the "classical" SPP. However, it is important to note that the largest position errors are still present and none of the variance models show any kind of improvement in this regard. Groves made a discussion on this in [22], claiming that the variance models are not appropriate to mitigate the large errors due to outlying observations. With respect to $C/N_0$, NLOS signals (those radio signals which are not directly received by the receiver but only via reflections) can be nearly as strong as the directly received signals, but also quite weak, which implies that the $C/N_0$ values are not fully representative of the quality of the received pseudorange. In case of the elevation angle based models, there are some maximum errors which are even much larger than the regular SPP. This is due to the interaction of the signals with the bridges. Under these structures, high elevation satellites still have higher $C/N_0$ than low elevation satellites, but their signals are highly contaminated by NLOS effects. On the other hand, low elevation angle satellites have lower strength but do not get to the receiver as NLOS signals.

As can be seen from Fig. 6.8, the variance model based in $C/N_0$ is the best performing among the variance models presented. Therefore, it will be the one used for further experiments in the next Chapter 7. The models based on the elevation angle of the satellites will not be considered any longer.

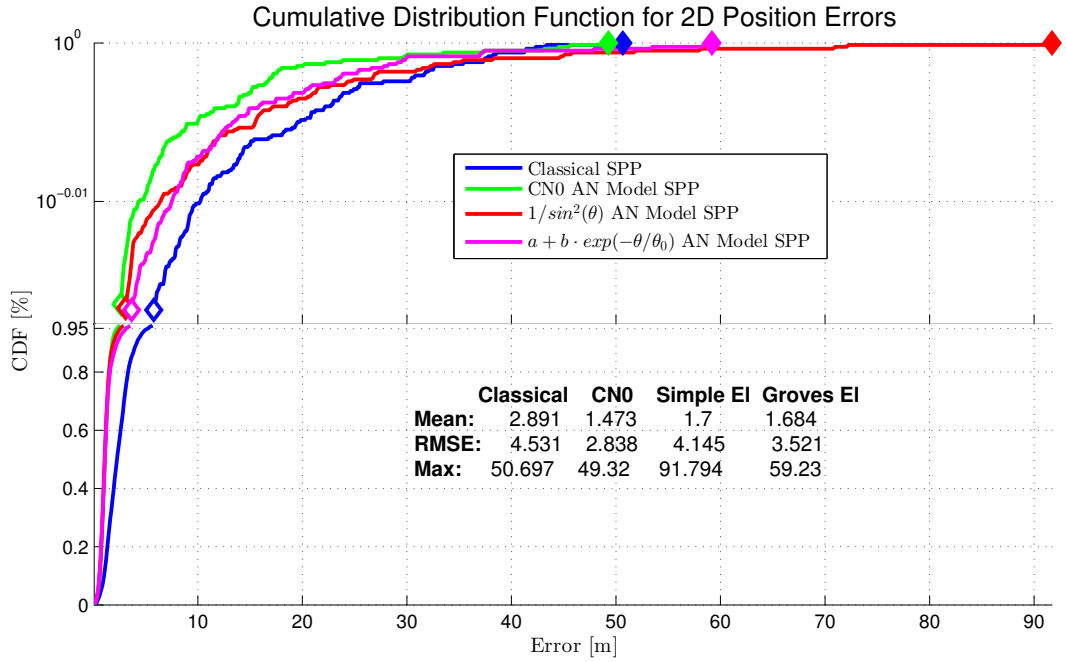


FIGURE 6.8: Cumulative Distribution Function (CDF) of the horizontal position error, as well as some statistics on the performance of the models.

Chapter 7

# Results on Satellite Positioning

In this chapter, it is presented a comparison on the performance of the robust techniques previously presented in 5. As discussed before, the developed schemes are tested with satellite signals with induced artificial in the Port of Rostock and real severe multipath effects for the measurement campaign in Koblenz.

## 7.1 Port of Rostock

This experiment takes place in the port of Rostock. Given the lack of errors in the satellite signals, the SPP reaches a mean position error of less than 2 meters (compared with a post processed RTK solution), and a maximum error of just 16 meters. For this, we can consider this scenario as ideal in terms of quality of the signals.

As the scope of the presented work is the development of robust methods to detect outlying errors for satellite-based navigation, this scenario is used as benchmark for the robust methods performance. For that, it is added random noise to the pseudoranges observed to study the position solutions of the said techniques against the regular SPP.

In order to achieve this, Three satellites available throughput the whole measurement campaign are selected. Then, random noise following a standard normal distribution is added to the pseudoranges observed in those satellites to be contaminated. Moreover, different magnitudes of the errors are tested, in order to check the sensitivity of the different methods against this contaminated data. In order to be representative, a Monte Carlo simulation is executed, repeating the proposed experiments a total of 100 times. Each of the simulations consist of the combination of 6 experiments: one, two and three satellites contaminated and two magnitudes for the errors for each of them. The noise amplitude is 8 and 20 $\sigma$, where $\sigma$ is the expected error of the pseudorange under regular conditions and be considered to be 2 meters. This means, error between 16 to 40 meters is added. In Fig. 7.1, it can be seen the estimated position from the SPP, having three contaminated satellites with errors of 40 meters, which is the worst case scenario among the proposed experiments.

Before studying the results of the Monte Carlo simulation, the asymptotic efficiency of the methods is tested by checking the performance without the addition of any kind of noise to the observed pseudoranges. Table 7.1 summarizes the performance and gathers the statistics on the results obtained.

The asymptotic efficiency refers to the likelihood of a method to the classical LS adjustment under Gaussian conditions of the errors. While M estimator has a high efficiency, as its output is very similar to the regular SPP, LMS is much worse performing, with a mean position error more than 50 centimetres higher than SPP. This is the well known problem of LMS, as already described in the seminal article [51], which is having a very low asymptotic efficiency.


FIGURE 7.1: Trajectory reference and the estimated position from regular SPP within the experiment, where a noise of 40 meters was simultaneously added to three of the LOS satellites.

**Results without contamination**

| **Method** | Mean [m] | RMS[m] | 95% CDF [m] |
|---|---|---|---|
| SPP | 1.72 | 2.234 | 4.83 |
| M | 1.72 | 2.20 | 4.66 |
| GM | 1.78 | 2.20 | 4.65 |
| S | 1.78 | 2.26 | 4.55 |
| LMS | 2.31 | 3.01 | 6.36 |

TABLE 7.1: Statistics on the performance of different robust methods without the addition of noise to the measurements.

**Experiment #1: One single satellite is contaminated**

| Method | $8 \cdot \sigma$ Mean [m] | $8 \cdot \sigma$ RMS[m] | $8 \cdot \sigma$ 95% CDF [m] | $20 \cdot \sigma$ Mean [m] | $20 \cdot \sigma$ RMS [m] | $20 \cdot \sigma$ 95% CDF [m] |
|---|---|---|---|---|---|---|
| SPP | 7.05 | 8.28 | 15.49 | 14.29 | 16.69 | 30.84 |
| M | 6.35 | 7.72 | 14.91 | 11.83 | 14.76 | 29.32 |
| GM | 5.58 | 6.75 | 13.00 | 9.43 | 11.96 | 24.40 |
| S | 6.30 | 7.68 | 14.84 | 11.70 | 14.65 | 29.19 |
| LMS | 5.30 | 6.53 | 12.77 | 8.37 | 11.14 | 23.59 |

TABLE 7.2: Statistics on the performance of different robust methods when single satellite is contaminated with random noise of different magnitude.

The results from contaminating one single satellite during the whole measurement campaign are shown in table 7.2. It is observed how the mean error of the regular SPP went from less than 2 meters to slightly higher than 7, just by contaminating one single satellite. In principle, this is the case scenario for which the robust methods should exhibit theoretically great performance as their breakdown point is enough to detect and mitigate one single faulty measurement (with the exception of the M estimator, whose breakdown point $\epsilon^* = 0$). However, the table shows how none of the methods is able to perform a complete exclusion of this faulty measurement, and despite all of them showing a better performance, they do not reach the accuracy of about 2 meters of mean position error that could be reached in the absence of outliers. The explanation lies in the fact that solving the positioning problem is not a linear regression problem, in which the influence of the outliers and their exclusion is very clear. Instead, this problem is represented by a non-linear system of equations composed by 4 unknowns, with a much higher complexity than the toy problems presented by the classical authors in order to check the performance of the robust schemes. Furthermore, the error is not added as a constant, but as random noise, so all the errors cannot be expected to be eliminated.

**Experiment #2: Two satellites are contaminated**

| Method | $8 \cdot \sigma$ Mean [m] | $8 \cdot \sigma$ RMS[m] | $8 \cdot \sigma$ 95% CDF [m] | $20 \cdot \sigma$ Mean [m] | $20 \cdot \sigma$ RMS [m] | $20 \cdot \sigma$ 95% CDF [m] |
|---|---|---|---|---|---|---|
| SPP | 11.98 | 14.70 | 28.85 | 29.18 | 36.23 | 71.63 |
| M | 11.58 | 14.59 | 29.13 | 27.82 | 35.94 | 72.66 |
| GM | 8.64 | 10.93 | 22.10 | 17.63 | 24.11 | 51.87 |
| S | 11.53 | 14.56 | 29.09 | 27.62 | 35.75 | 72.35 |
| LMS | 6.87 | 9.22 | 19.61 | 11.68 | 18.42 | 40.81 |

TABLE 7.3: Statistics on the performance of different robust methods when two satellites are contaminated with random noise of different magnitude.

In this second experiment, it becomes more evident how much better the performance of the LMS is, in comparison with the rest of the methods. Also, the generalised M estimator, GM estimator, has a notable performance, scaling down the mean error in the position by half, for the case of contamination of large magnitude $20 \cdot \sigma$. On the other hand, the performance of the M and S estimators is not satisfying at all, as the improvement is marginal against the regular SPP.

**Experiment #3: Three satellites are contaminated**

| Method | $8 \cdot \sigma$ Mean [m] | $8 \cdot \sigma$ RMS[m] | $8 \cdot \sigma$ 95% CDF [m] | $20 \cdot \sigma$ Mean [m] | $20 \cdot \sigma$ RMS [m] | $20 \cdot \sigma$ 95% CDF [m] |
|---|---|---|---|---|---|---|
| SPP | 12.50 | 15.09 | 29.30 | 30.62 | 37.14 | 71.61 |
| M | 11.77 | 14.79 | 29.65 | 28.34 | 36.35 | 72.82 |
| GM | 9.22 | 11.74 | 23.92 | 19.51 | 26.82 | 57.80 |
| S | 11.73 | 14.76 | 29.64 | 28.19 | 36.24 | 72.32 |
| LMS | 7.84 | 10.61 | 22.62 | 16.09 | 24.38 | 54.69 |

TABLE 7.4: Statistics on the performance of different robust methods when three satellites are contaminated with random noise of different magnitude.

Finally, in the third scenario there are three satellites which present artificially induced errors in their pseudorange observations. Obviously, one expects the estimated solution for the regular SPP to be extremely poor, as there are multiple errors of very large magnitude. While one could expect some methods with a high breakdown point to completely deal with these kind of outliers, even with the simulated outliers it can be observed that this is not feasible given that the character of the positioning problem is much more complex than the framework of linear regression in which all robust methods were postulated. Another two remarkable facts which might be related to the poor performance of methods such as M or S estimators is that all the robust schemes are designed under the assumption that the number of measurements $n$ is very large and that the amount of unknowns parameters $p$ is very small, or at least very small compared to $n$. Next figure 7.2, shows a boxplot with the statistics of the tested methods.

As it can be seen, the mean error for the position solution is improved by LMS in almost 15 meters against classical SPP. On top of that, one can see how the $3^{\text{rd}}$ quartile for the LMS error is still smaller than the mean error position of SPP. After checking the performance of the four robust methods tested for this scenario, the results are summarized as follows:

- *M estimator*. Despite having the same breakdown point $\epsilon^* = 0$ as the classical LS, the cost function is still more resilient than the classical sum of squared residuals in LS. However, it can be seen how using artificially contaminated data with large outliers, the performance is very similar to the one in SPP.

- *GM estimator*. This method showed a great performance within all the experiments, proving that under simulated conditions, it can deal with high percentage of contaminated data of different orders of magnitude.

- *S estimator*. Despite having a high breakdown point and the highest among the schemes based on an IRLS procedure, the S estimator has shown to have a very poor performance in this simulation. As it happened with the M estimator, the improvement is just marginal.

- *LMS estimator*. This method has proven to have an outstanding performance under conditions of large contamination for multiple satellites. However, it is well known that the weakest spot of this method is its low asymptotic efficiency, which means that under regular conditions, the overall performance could decrease.

This Monte Carlo simulation was used as a tool to check the performance of the methods with artificially induced errors, as well as cross checking if the results matched with the theoretical characteristics of each of the methods. With the exception of the poor performance

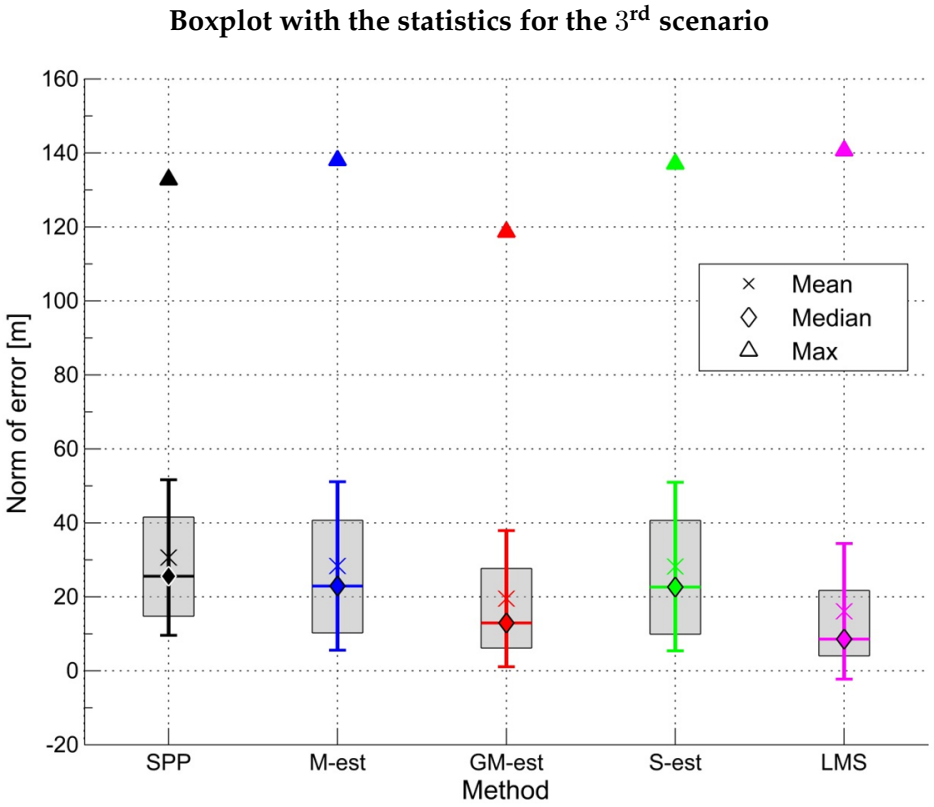


FIGURE 7.2: Results for the third experiment, in which there are a total of three contaminated satellites with a magnitude of the error of $20 \cdot \sigma$, the equivalents of random errors of 40 meters in average.

of the S estimator, the results of this simulation agree with the characteristics of the methods presented in Chapter 5. Nevertheless, the outliers in this experiments are induced, which seems to be a common practice in the community [5, 56, 27]. In the next section, it is explored the performance of the methods in a real challenging scenario, in which the satellite signals are heavily affected by multipath and NLOS effects.

## 7.2 Moselle River

As described in the previous chapter, the waterway of the Moselle River presents several challenges for the satellite navigation. The three bridges create a severe disruption of the radio signals, as under these structures the satellites are not in LOS. Accurate positioning problem increases its difficulty, as the receiver gets a mixture of direct clean LOS signals, multipath contaminated and NLOS signals due to reflection and diffraction of the signals on the water or on the surrounding constructions.

### 7.2.1 Robust Methods without Variance Models

On first place, in Fig. 7.3 we observe that the position solution from non-weighted SPP against the reference from the total stations which followed the exact position of the vessel. As it can be seen, the estimated position suffers from jumps not only in the lock and under the bridges, but also in the vicinity of those, with horizontal position errors (HPE) being as high as 50 meters.

With the exception of the vicinity of the bridges, the satellite positioning performance can be considered to be acceptable, with less that 3 meters error. Under limited visibility

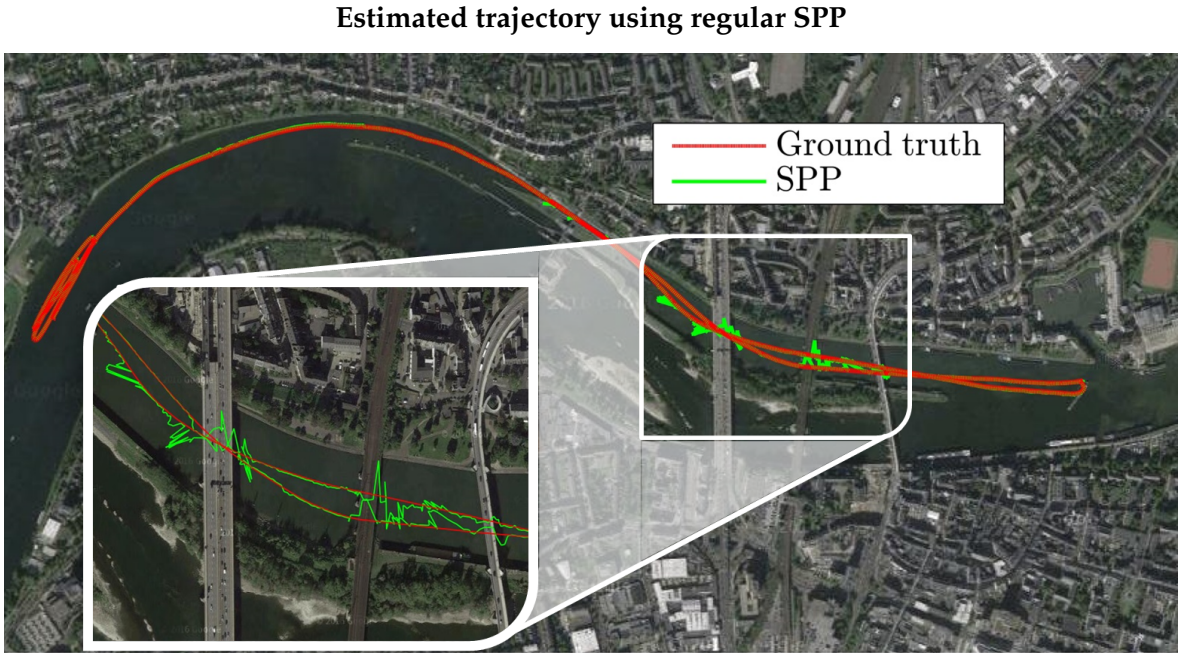


FIGURE 7.3: Trajectory reference and the estimated position for the non-weighted SPP during one hour of measurement campaign in the Moselle River.

conditions, where the captain needs to trust the output of the positioning systems his boat is equipped with, a failure of 50 meters in the river may lead to a collision with the pillars of a bridge or even with the shore of the river, under conditions of low visibility.

In figure 7.4, it is shown the number of visible satellites over time. As there were always at least five satellites, the position solution from a regular SPP solver was always available. In the same figure, one can see how the position error rapidly increases in the areas marked as "B" and "C" (see figure 6.4 to remember the scenario already presented in the previous Chapter 6), having several peaks of more than 40 meters. HDOP is a parameter which gives, based on the geometry of the satellites taking on the solution, an idea on the quality of the solution. This is not a valid indicator, as during the time interval between 1000 and 2000 seconds, the performance of the SPP is supposed to be worse than around 2500 seconds, when the vessel passes under the bridge. The sudden changes in the HDOP are related to a new satellite being in LOS or another being out of sight for the receiver.

Within the context of this work, the main goal is not to decrease the mean error for the estimated position, but to avoid very large position errors as a consequence of faulty satellite signals. In this section, it is shown the results from the most promising robust methods presented in 5. Firstly, table 7.5 summarizes the performance of all the methods based on the statistics of the error.

Despite all the robust methods improving the position estimated compared with regular SPP, there are some distinctions among them. As a disclaimer, the discussion on the results of the robust methods cannot be taken as direct claims regarding the efficiency or the performance of the algorithms as this is a particular mathematical problem (GNSS positioning), as one scenario is not representative enough ,the measurement campaign lasts for just one hour, and the errors in the satellite signals and thus in the performance of the robust methods is associated to a particular geometry of the satellites in LOS.

- *M estimator*. Despite having a breakdown point $\epsilon^* = 0$, one can see than the mean error is reduced by almost 40 centimetres. As well as, the rest of the statistics are improved and they are able to compete with the rest of the robust schemes. Nonetheless, within

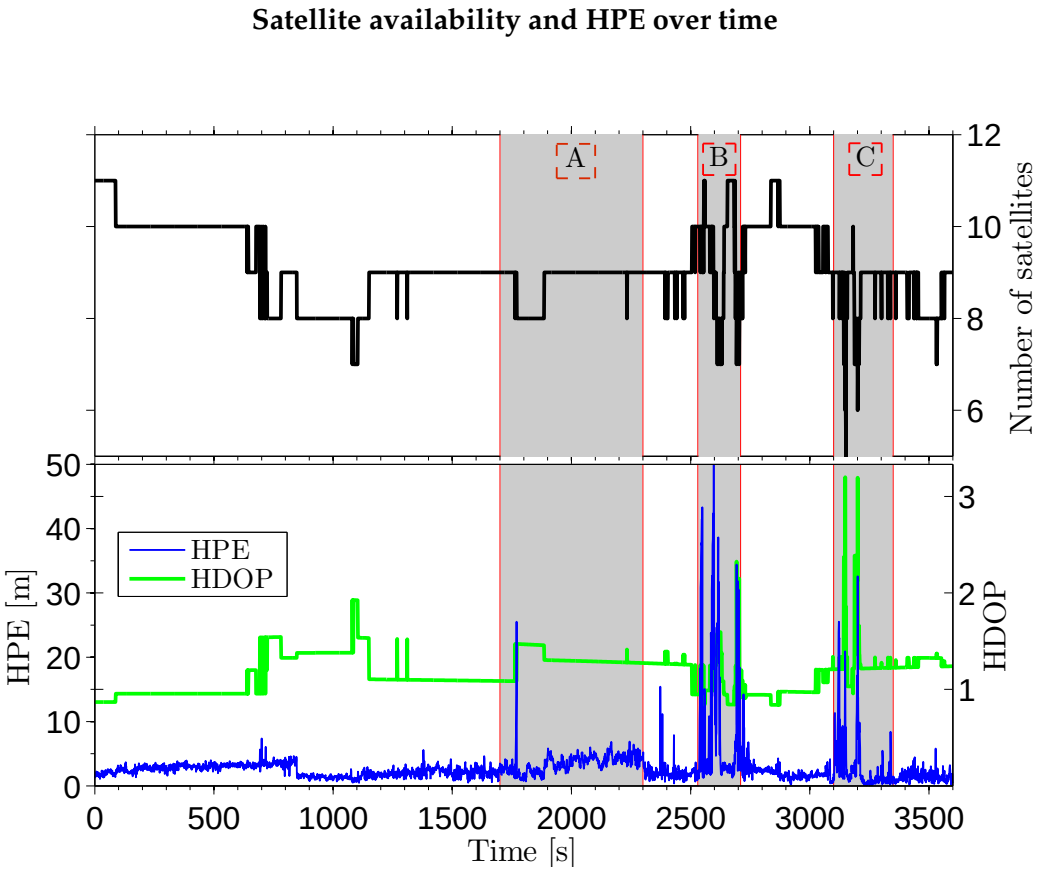


FIGURE 7.4: Satellite availability plot during the scenario (black line), corresponding HDOP as a reference of the uncertainty for the horizontal position estimation (green line) and the horizontal position error (HPE) for classical non-weighted SPP (blue line).

**Statics on the Robust Methods performance**

| **Method** | Mean [m] | RMS [m] | 95% CDF [m] | Max [m] |
|---|---|---|---|---|
| SPP | 2.89 | 4.53 | 5.30 | 50.70 |
| M | 2.52 | 3.54 | 4.30 | 36.77 |
| S | 2.38 | 3.38 | 4.19 | 34.04 |
| GM | 2.30 | 3.23 | 4.36 | 34.98 |
| LMS | 2.41 | 3.38 | 4.86 | 34.90 |
| LTS | 2.52 | 3.50 | 4.95 | 34.90 |
| Danish | 2.45 | 3.59 | 6.48 | 40.28 |
| RAIM | 2.48 | 3.40 | 3.91 | 45.40 |
| RANSAC | 2.57 | 3.52 | 4.61 | 34.91 |

TABLE 7.5: Statistics on the performance of the robust methods without using variance models for the pseudorange measurements. Green colour indicates a significant improvement against SPP, while red colour is used to remark a worse result compared to SPP.

this method it would not even be possible to use the variance models for the observations, which penalizes this method and would exclude it from further discussions.

- *S estimator*. The scale estimator shows an excellent performance, being the 95% CDF and maximum HPE the best among the other robust schemes. This method, which is performed as an Iteratively Reweighted LS (as S and GM estimators), presents also the advantage of being computationally less demanding and, in other words, being computed faster than methods which require subset selection (LMS, LTS, etc.).

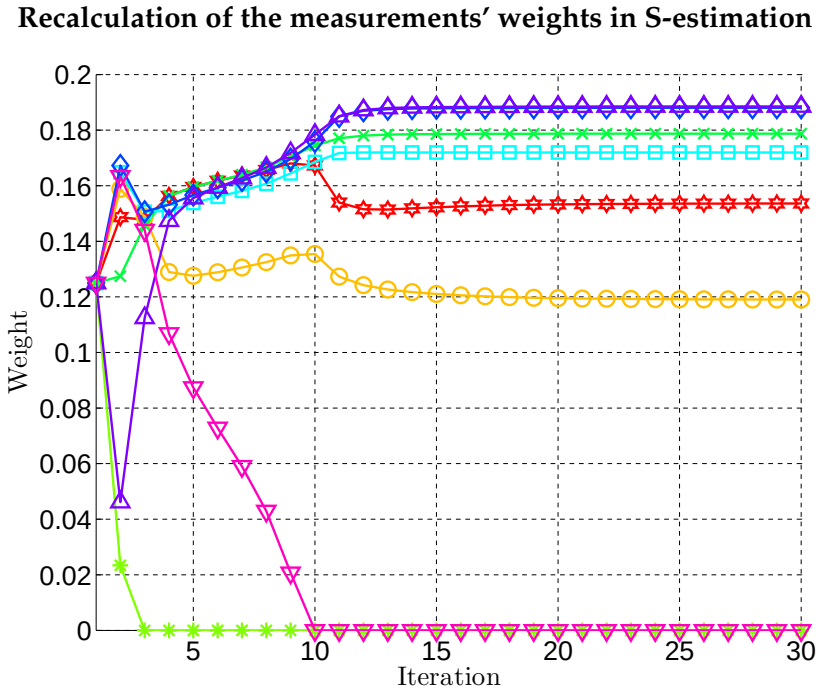


FIGURE 7.5: Change of the weights over iterations within a single epoch of S-estimator position solver.

In Fig. 7.5, it is shown an example of the weights recalculation of the measurements. This example has been selected for one of the challenging trajectory segments, where the regular SPP solution results in a HPE of 32 meters, while the S-estimator presents a HPE of approximately 2 meters. One can clearly see that the S-estimator sets the weights of two measurements to zeros, while the rest six measurements are slightly re-weighted while computing the final positioning solution.

- *GM estimator*. This method has a theoretical breakdown point $\epsilon^* = 1/(p+1)$ and shows a performance very similar to that of S estimator, in the sense that is computationally not as demanding as LMS or LTS and still has excellent statistics. Furthermore, it reaches the lowest value for the mean and root mean square (RMS), beating the classical SPP estimation by 60 centimetres and 1.30 metres respectively. The weights assigned are based on a redescender function $\rho$ (defined in section 5) which takes into account not only the residuals of the measurements but also their influence in the geometry matrix. This method is also appealing as it allows to leverage measurements, unlike the S estimator.

- *Least Median of Squares (LMS)*. This method is claimed to be low asymptotic efficient, which means that in the absence of outliers or under regular conditions, it might differ from the least squares adjustment, which is optimal under the assumption of Gaussian noise. Nevertheless, the mean and RMS of the HPE reflect that there are unexpectedly large errors in regular conditions. As mentioned previously, all subset-selection based

methods present the drawback of the computation power required, as one must estimate a solution for each of the possible subsets, or at least for a representative amount of them (given by the equation 5.17). This means that, despite being the ones with the highest breakdown point among all the different robust schemes, they might be scalable with the future of the GNSS positioning. Currently, multiconstellation-based positioning system is already fully operative (GLONASS and GPS are already available worldwide and the European Space Agency (ESA) has the launch of new satellites for the Galileo among the objetives for the next years). This would mean having more than 30 satellites in LOS, and thus one would need to compute the solution for $k = \binom{n}{p}$ different subsets (with $p = 4 + a$, where $a$ is the number of constellations different to GPS added to the solution, as the clock offset of the receiver would be different for each of them [1]).

- *Receiver Autonomous Integrity Monitoring (RAIM)*. This technique has been the standard tool to detect failures on the GNSS positioning in aerospace and other advanced applications. However, the failure detection and isolation performed with this method is occasionally limited as it was primarily proposed to handle only single failures on the signals. In this work, it is checked that the Chi-squares test might not suffice in scenarios where there are multiple simultaneous signals deeply affected by multipath effects, or at least not as good as other robust methods.

In figure 7.6, it is shown the CDF for the HPE for three different robust schemes. It includes only the best performing methods among their categories: best subset selection (S estimator), iteratively reweighted least squares (LMS) and RAIM as example of classical integrity monitoring. One can see that the 95% CDF is reached for the robust methods with a smaller value than for the regular SPP. Regarding the largest values due to faulty signals affected by multipath, generally under the bridge, are overpassed much better for the three alternatives to classical SPP.

As well as for estimating the solution position, the robust schemes can also the applied to the velocity estimation. The velocity calculation is also based on a LS adjustment, which implies that large error can come into the solution as a consequence of faulty measurements on the Doppler shift from the satellites. Nonetheless, this error is not as heavily affected by multipath and NLOS of sight effects as it is for pseudorange observations. Unlike the position calculation, the system of equations for velocity estimation is linear (further details on these equations were given in the Methods section of this work 3), so the method is not iterative. All the iterations coming from the IRLS methods, such as M, GM or S estimator, are solely to exclude or down-weigh the influence of the measurements.

One can see that the errors are not as easily detected as for the case of position estimation. In general, all methods have a performance very similar to the regular LS for velocity estimation, with just marginal improvements. For velocity calculation, the low efficiency of the LMS becomes even more remarkable, getting a considerably much worse performance. The most probable reason for this unexpected behaviour is that after selecting the best subset among the subsets with the minimum number of measurements, the incorporation into the final solution of additional measurements is not achieved, and thus the solution only comes from the minimal amount of subsets (using low amount of measurements under good conditions results in a severe disrupt of the solution, as can be seen in the table 7.6). The procedure to label new measurements are inliers is as next: those observations whose residuals pass a test based on the results from the best subset will be included in the subset and will take part on the estimation of the final solution. The test is done as follows:

$$r_i^2 \leq a\,\hat{\sigma}^2, \qquad i\text{th observation} \longleftarrow \text{inlier}$$

[1] In principle, Galileo time would be synchronized to the GPS time, so Galileo constellation would not increase the number of unknowns to estimate.

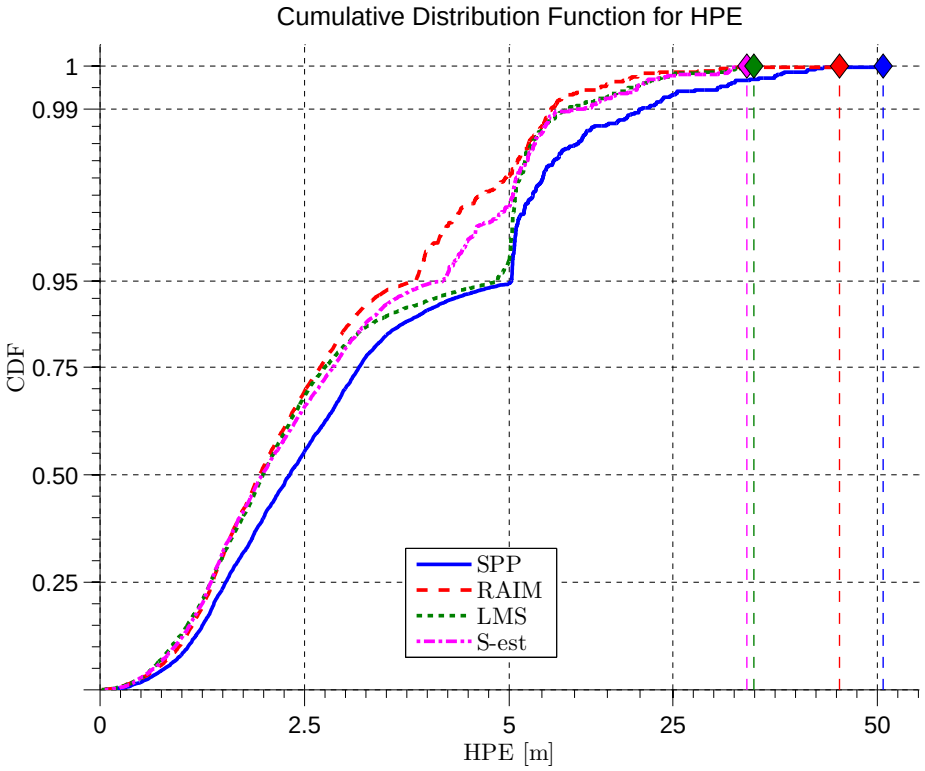


FIGURE 7.6: Cumulative distribution of HPE for SPP several robust estimation schemes (all using non-weighted measurements).

**Statistics for Velocity Estimation**

| Method | Mean [m/s] | RMS [m/s] | 95% CDF [m/s] | Max [m/s] |
|---|---|---|---|---|
| SPP | 0.052 | 0.19 | 0.22 | 3.71 |
| M | 0.051 | 0.19 | 0.22 | 3.60 |
| GM | 0.052 | 0.18 | 0.22 | 3.44 |
| S | 0.051 | 0.18 | 0.22 | 3.52 |
| LMS | 0.074 | 0.39 | 0.26 | 7.57 |

TABLE 7.6: Performance results of the snapshot velocity calculation for robust methods.

where $a$ is the parameter to control how relaxed is the test. The parameter $a = 2.5$ is set to be the same for both position and velocity estimation, just to make it fair. However we can see how this might be the main reason why LMS is performing much worse than other robust methods and even than regular LS for velocity estimation.

The analysis continues showing the segment of the trajectory during the time in which the vessel is moving down river, going the first two bridges. It is observed a clear improvement in comparison with regular SPP. However, there are still some jumps in the position navigation, as the rate of faulty pseudorange measurements is too high. This implies that there might not be possible way to compute a better estimation for the position using single frequency radio signals. In order to overpass these difficulties, it would be necessary to use phase measurements, augment the system with the corrections in the position of the ground stations (only in areas in which this technical support is available) or finally make of algorithms with memory for the state and uncertainty of the system (as a reminder, all SPP are memoryless: they use only the current information coming from the satellite navigation).

**Details on the estimated trajectory with robust methods**

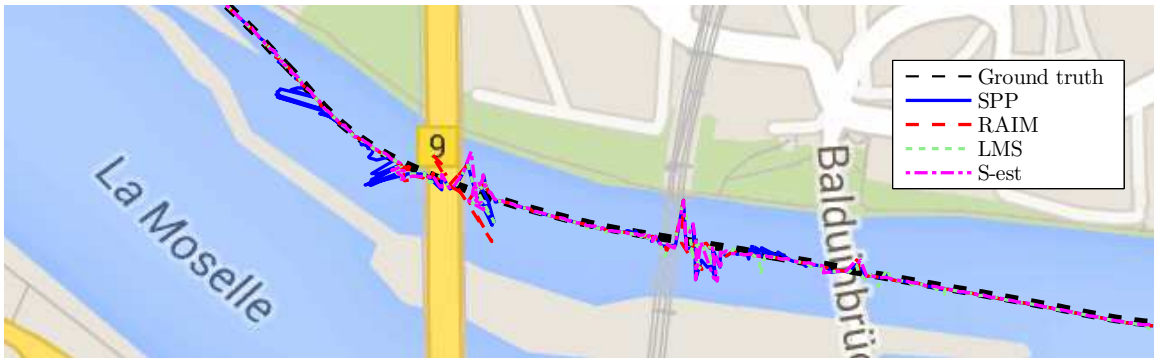


FIGURE 7.7: Positioning performance of the SPP, RAIM and some of the robust estimation schemes, without using the variance model for weighting the quality of the pseudoranges.

As a consequence of looking forward for further improvements to be done within the framework of robust algorithms, we explored whether the error in the position solution are correlated or not among the different estimators. If so, we could claim that there is not a better solution supported by robust statistics. Otherwise, we could think that the estimators have complementary properties, and it would be possible to create a decision matrix which allows to choose among their estimated positions for the target, with a criterion based on the likelihood between them or the estimated uncertainty of the solution. As it can be seen in Fig. 7.8, during the time immediately previous to pass under the first bridge down river, while LMS solution has some spare bad estimations (from 3020 to 3080 seconds), probably due to the low asymptotic efficiency of the solution while S estimato provides the solution with the lowest error. On the other hand, we see how during a time gap of about 10 seconds ($\sim 3120$ seconds into the simulation), the solution estimated by the S estimator is equivalent to the one from regular SPP with an error of more than 15 m, while RAIM and LMS are able to mitigate the errors by excluding some faulty satellites. Being able to distinguish which is the best among the robust schemes drive to an excellent position solution, with practically no outlying position estimations. The main problem here is that the robust methods often do not have any solution quality indicator (e.g. compared to KF covariance or integrity ifnromation from RAIM) and therefore one needs to develop a methodology on how actually to choose between the methods.

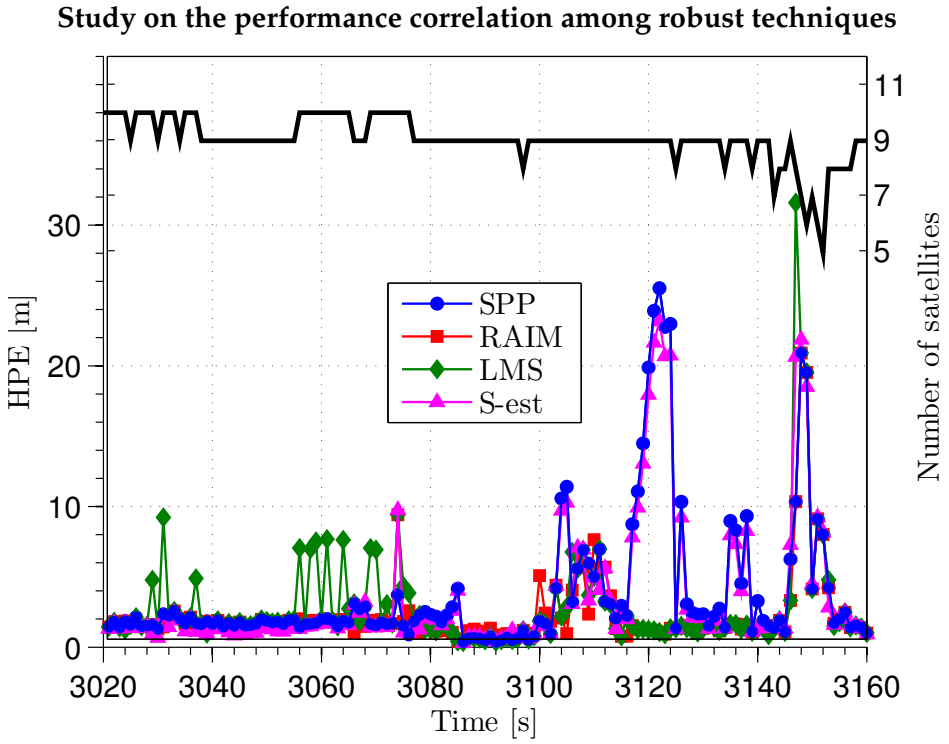


FIGURE 7.8: Detail on the HPE corresponding to the vicinity to the first bridge for regular SPP and some of the robust estimators (without using the variance model for the pseudoranges).

### 7.2.2 Robust Methods using Variance Models

In this section the robust methods will include the variance model explained in 6.2.1, and it was shown why the carrier-to-noise density $C/N_0$ model will be used to leverage the pseudorange observations. In Fig. 7.9, we can observe the values for $C/N_0$ of all satellites during the whole hour of measurement campaign. These measurements are interpreted in a way that, the higher the value of $C/N_0$ is, the more reliable the signal for that satellite is considered to be. One could confirm this by looking at the figure during the times in which the vessel goes under the bridges, having sudden changes in the strength of the signal and thus, a lower value of $C/N_0$.

However, as already stated by some authors [16], [22], the variance models are very good in order to achieve a much better estimation of the mean position error but $C/N_0$ is not a good indicator of NLOS or multipath effects, which are expected to be exactly the reasons for the largest errors, as can be seen in table 7.7.

The bad performance of the robust methods when using variance models for the pseudorange can be attributed to give naturally more weights to those measurements coming from stronger radio signals, when these are the ones which suffer larger errors related to multipath and NLOS. Nonotheless, having a good visibility and open sky conditions, the use of variance models bring a lot of benefits.

As brief summary on the performance of the robust methods applied to GNSS positioning:

- The presented schemes result convenient for dealing with faulty measurements, drastically reducing the impact of the outliers on the final position estimation.
- Subset based methods like LMS or LTS are computationally much more demanding than the methods following a IRLS procedure. On top of that, their low asymptotic efficiency becomes an important factor, as their performance is heavily degraded under

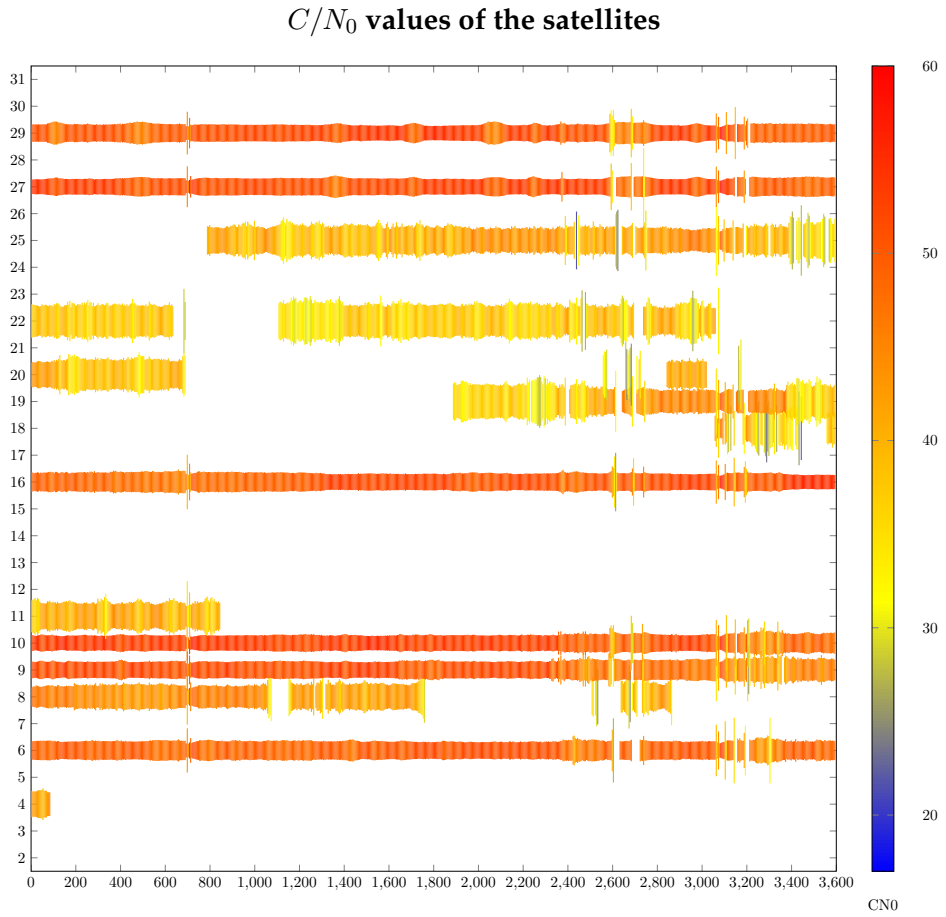


FIGURE 7.9: Satellite visibility during the test scenario. The line color and width encode the GNSS signal quality in terms of $C/N_0$ (the wider the line, the lower the $C/N_0$ values).

**Statistics on the Robust Methods using Variance Model**

| Method | Mean [m] | RMS[m] | 95% CDF | Max[m] |
|---|---|---|---|---|
| SPP | 1.47 | 2.84 | 2.31 | 49.3 |
| GM | 1.69 | 2.84 | 3.33 | 48.9 |
| GS | 1.95 | 3.01 | 4.22 | 46.2 |
| LMS | 1.64 | 2.97 | 3.20 | 45.6 |
| LTS | 1.60 | 2.95 | 3.00 | 45.6 |
| Danish | 1.78 | 3.35 | 4.92 | 49.3 |
| RAIM | 1.62 | 3.30 | 2.71 | 83.90 |
| RANSAC | 1.48 | 2.89 | 2.29 | 50.9 |

TABLE 7.7: Performance results of the robust positioning methods: weighted approaches.

regular Gaussian conditions.

- Traditional RAIM, used as standard in GNSS navigation to perform fault mitigation of the signals, is not as effective as the robust methods under challenging scenarios in which there are multiple simultaneous failures.
- Despite being very appropriate to reduce the average mean error, the use of variance models affects the performance of the robust methods negatively.

Chapter 8

# Results on GPS/IMU Navigation

This chapter is devoted to discuss the results on the navigation fusing inertial and satellite information. The core of the required hardware for this system consists of an IMU (3-axis accelerometer and gyroscope) and a GNSS receiver. The inertial navigation systems use onboard sensors which are immune to jamming and can track both fast and subtle motion models, as well as to bridge short GNSS outages and smooth the noise of the navigation solution. The information from the IMU and the GNSS can be integrated synergistically, obtaining the short term performance of the IMU and long term stability of the GNSS within the hybrid system. To assess the performance of the proposed schemes in integrated navigation systems, the output of the robust regression estimators is fused with the data from onboard IMU within an Unscented Kalman Filter (UKF) using quaternion attitude parametrization.

## 8.1 Filter Description

We propose two different schemes for the Kalman filter: tightly and loosely coupled architectures. While in the tightly coupled filter the measurement model is fed directly with the reading from the satellites (pseudoranges and Doppler shift), in the loosely coupled the measurement model uses the solution for position, velocity and the baselines of three GPS antennas (for the attitude solution) coming from an external solver. The discrepancies between them are very clear:

- The tightly coupled architecture can make use of the information from the satellites even when the number of satellites is below 4, which is the minimum amount of measurements necessary to obtain the position (and hence the attitude) and velocity solution. This means that during a GNSS outage, we can still impose some constraints on the natural drift of the inertial navigation, as long as there is at least one satellite observation. On the other hand, the loosely coupled architecture needs an external snapshot solver to provide the measurement model inputs and, therefore, the measurements from four or more satellites have to be available.

- The complexity of the measurement model in the tightly coupled architecture is much higher than the one in the loosely coupled, as the inclusion of the raw measurements from the satellite make the measurement model equations way more complicated. Also, the state and covariance matrix of the tightly coupled filter is bigger than the one in the loosely coupled one, as it needs to include the clock offset and clock offset rate of the receiver in the state.

- The higher complexity of the measurement model could drive to convergence issues [47], and result in some numerical issues, especially for higher dimensional problems

with full noise augmentation (process and measurement noises to be considered as a part of the state).

**State for the Loosely Coupled Architecture UKF**

| State | Covariance | Variable | Symbol | Coordinate System |
|---|---|---|---|---|
| 1:4 | 1:3 | Attitude Quaternion | $q$ | From B-frame to ECEF |
| 5:7 | 4:6 | Velocity | $v$ | ECEF |
| 8:10 | 7:9 | Position | $p$ | ECEF |
| 11:13 | 10:12 | Gyroscope Offset | $b_\omega$ | B-frame |
| 14:16 | 13:15 | Accelerometer Offset | $b_a$ | B-frame |

TABLE 8.1: Full-state UKF: loosely-coupled INS/GNSS integration.

**State for the Tightly Coupled Architecture UKF**

| State | Covariance | Variable | Symbol | Coordinate System |
|---|---|---|---|---|
| 1:4 | 1:3 | Attitude Quaternion | $q$ | From B-frame to ECEF |
| 5:7 | 4:6 | Velocity | $v$ | ECEF |
| 8:10 | 7:9 | Position | $p$ | ECEF |
| 11:13 | 10:12 | Gyroscope Offset | $b_\omega$ | B-frame |
| 14:16 | 13:15 | Accelerometer Offset | $b_a$ | B-frame |
| 17 | 16 | Clock offset | $c\delta t$ | - |
| 18 | 17 | Clock rate | $c\dot{\delta} t$ | - |

TABLE 8.2: Full-state UKF: tightly-coupled IMU/GNSS integration.

The process models of both architectures follow a classical strapdown mechanization, summarized in the Fig. 8.1. In the case of the tightly coupled architecture, the process model is augmented to include the update the clock offset and clock offset rate of the receiver. All the equations for the process and measurement models were explained in the third chapter on this work, in the inertial 4 and satellite navigation sections, respectively. Apart from these equations, for higher performance systems it is necessary to include lever arm compensation for the position and the velocity. This is important as position solution from the GNSS measurements is related to the centre of the antenna, while in the inertial mechanization the position is formulated for the IMU centre.

## 8.2 Port of Rostock

As we commented previously, the satellite visibility during the measurement campaign in the Port of Rostock were excellent, in terms of absence of multipath and NLOS effects. This implies that the overall improvement of the Kalman Filter over regular satellite-based navigation is just marginal: the mean position error is reduced less than one meter and the maximum error is reduced from 16 to 8 meters.

Due to the lack of "inconvenients" or challenges within this scenario, we designed a new experiment consisting on the induction of a GNSS outage. This is an artificial experiment as, even in case of jamming or spoofing of the signals, the satellite navigation messages do not suddenly disappear simultaneously, or at least they get heavily damaged before the visibility is lost. Nevertheless, this experiment shows how is the performance of the Kalman filter, and how fast the position solution drifts within time due to the triple integration of the sensors biases and inherent errors.

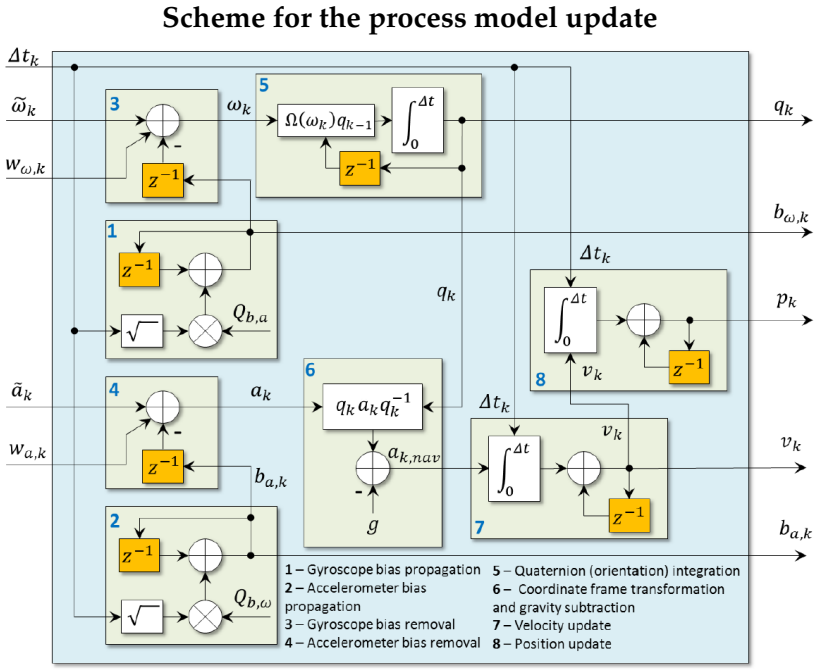


FIGURE 8.1: Details on the integration of the inertial sensors for the update of the state during the process model of the loosely and tightly coupled (only the clock offset and clock offset rate of the receiver are missing) UKF. Image from [48].

Additionally to the IMUs and the three antennas receivers, the Baltic Taucher is equipped with an additional sensors, the Doppler Velocity Log (DVL), which will be used in the measurement process to correct the velocity in the $x$ and $y$ axis. There are clear advantages on the use of this sensor, as it is self-contained and directly measures the velocity of the target. On the other hand, its reliability is slowed down for rough conditions of the sea, as well as for deep seas or oceans, as in that case the velocity of the current of the water is measured instead. However, it results really helpful in case of GNSS outages, as it allows the filter to drift linearly in time, instead of cubically in time due to the control of the velocity estimation. Next figure 8.2 illustrates the great difference, in terms of position drift, between the use ir not of the DVL sensor.

As we can see in Fig. 8.2, the estimated position from the Kalman filter can drift very rapidly in the absence of external reference. This is due to the triple integration of the sensors' biases and inherent noises, which completely destroy the position solution even in a very short period of time. On the other hand, we can see how beneficial it results the use of the DVL sensor (from $\sim$ 650 to $\sim$ 16 meters maximum position drift). As it constraints the error on the velocity the position error no longer grows cubically within time, but only linearly.

As mentioned in the experimental setup chapter 4, the "Baltic Taucher II" is equipped with two different gyroscopes: one is an expensive high performing FOG, while the second one is a relatively inexpensive MEMS. In Fig. 8.3, it is shown a performance comparison between the Kalman filter using the FOG and the MEMS gyroscopes, as well as the DVL sensor presented previously. The goal of this experiment is quantify how much of an impact the selection and the price of the hardware can influence the performance of the Kalman Filter.

In principle, both loosely and tightly coupled architecture presents almost an identical performance given the lack of position correction for the GPS. This is something to be expected, as the process models are almost identical with the exception of tightly coupled

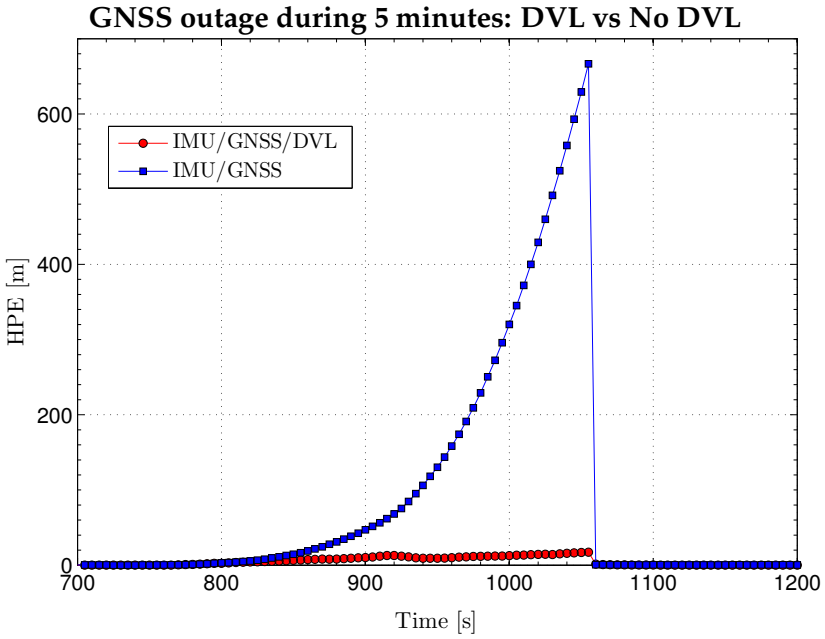


FIGURE 8.2: This figure illustrates the HPE of the different KF architecture, as well as the different sensor setup during an artificial GNSS outage of five minutes.

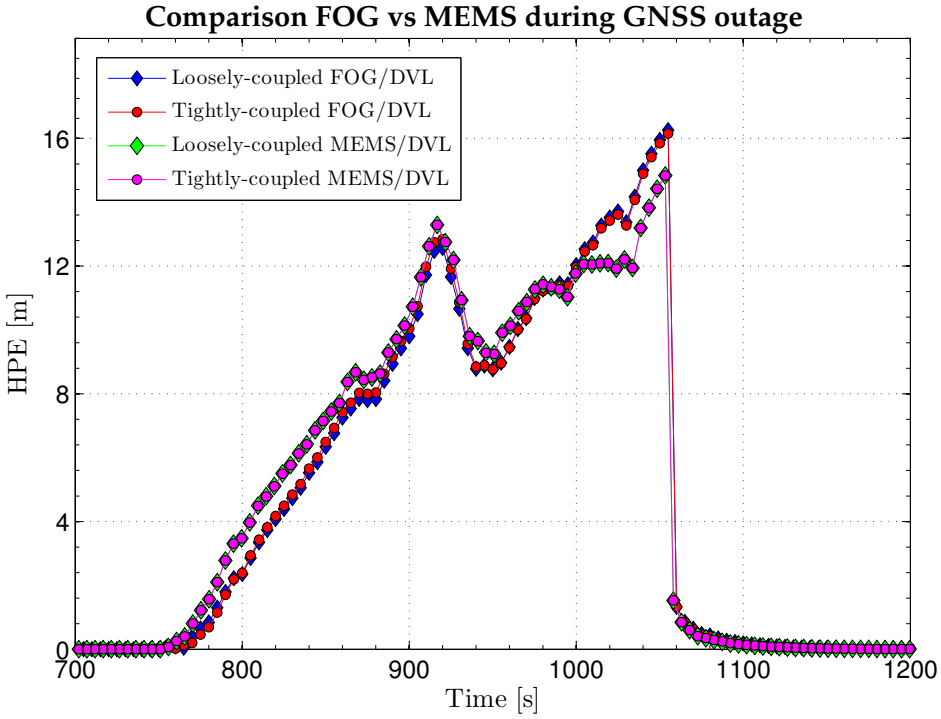


FIGURE 8.3: This figure illustrates the HPE of the different KF architecture, as well as the different sensor setup during an artificial GNSS outage of five minutes.

having its state slightly augmented to include clock offset and clock offset rate. Regarding the differences in performance between the KF using FOG or MEMS, we can see that the drift is very similar, and even more, the KF using the MEMS has around one meter less of position drift. This means that our Kalman Filter design could be implemented in vessel without adding the constraint of investing a large amount of money on a high performance IMU, as the difference in the performance of the hardware does not play such an important role for the final position estimation. However, this claim is only valid while having the velocity corrections from the DVL available. Without DVL, the GNSS outage is solely based on inertial integration and there the quality of the inertial sensor starts playing a more significant role.

## 8.3 Moselle River

Within this scenario it is explored the multiple advantages on the use of Kalman filtering for navigation. Due to the natural smoothing made in a well designed KF, the abrupt "jumps" that we obtain having regular SPP, and even with the robust methods, are avoided or compensated in the solution provided by the Kalman filter.

In this section it is compared the performance offered by three different configuration of our Unscented Kalman filter:

1. Tightly coupled UKF + GPS signals + baselines for the three antennas.
2. Loosely coupled UKF + position and velocity from regular SPP and baselines for the three antennas.
3. Loosely coupled UKF + position and velocity from the S-estimator and baselines for the three antennas.

For the KF approaches the measurement noises are set as follows: $\sigma_{PR} = 2\text{m}$, $\sigma_{RR} = 0.2\text{m/s}$ and the clock rate process noise $\sigma_{c\dot{\delta}t} = 0.1\text{m/s}^2$ with equivalent solution covariances calculated for the associated loosely-coupled strategies. The performance results of both RBE strategies are shown in Tables 8.3 and 8.4. In both tables LC- stands for the loosely-coupled approach and TC stands for tightly-coupled architecture. Finally, LC-S and LC-GS stands for the loosely-coupled approach where the outputs of the robust S- or GS-estimator are fed into the KF as the measurements. Moreover, in Fig. 8.4, it is shown the CDF with the HPE of the different non-weighted KF.

**Non-weighted UKF performance**

| **Method** | Mean [m] | RMS [m] | 95% CDF | Max [m] |
|---|---|---|---|---|
| SPP | 2.89 | 4.53 | 5.30 | 50.70 |
| TC UKF | 3.03 | 3.82 | 6.25 | 18.33 |
| LC UKF | 2.98 | 3.70 | 6.25 | 17.02 |
| LC-GS UKF | 2.50 | 2.87 | 5.39 | 9.47 |

TABLE 8.3: Performance results of the robust positioning methods using KF approaches: non-weighted approaches.

Although both weighted and non-weighted approaches we observe no mean HPE improvement except of the robust approach for the non-weighted strategy, the maximum HPEs are significantly improved when compared to memoryless snapshot algorithms. In all the

**Weighted UKF performance**

| Method | Mean [m] | RMS [m] | 95% CDF | Max [m] |
|---|---|---|---|---|
| SPP | 1.47 | 2.84 | 2.31 | 49.30 |
| TC UKF | 3.02 | 3.83 | 6.25 | 18.31 |
| LC UKF | 2.99 | 3.70 | 6.17 | 17.02 |
| LC-GS UKF | 2.52 | 2.87 | 5.43 | 9.42 |

TABLE 8.4: Performance results of the robust positioning methods using KF approaches: weighted approaches.

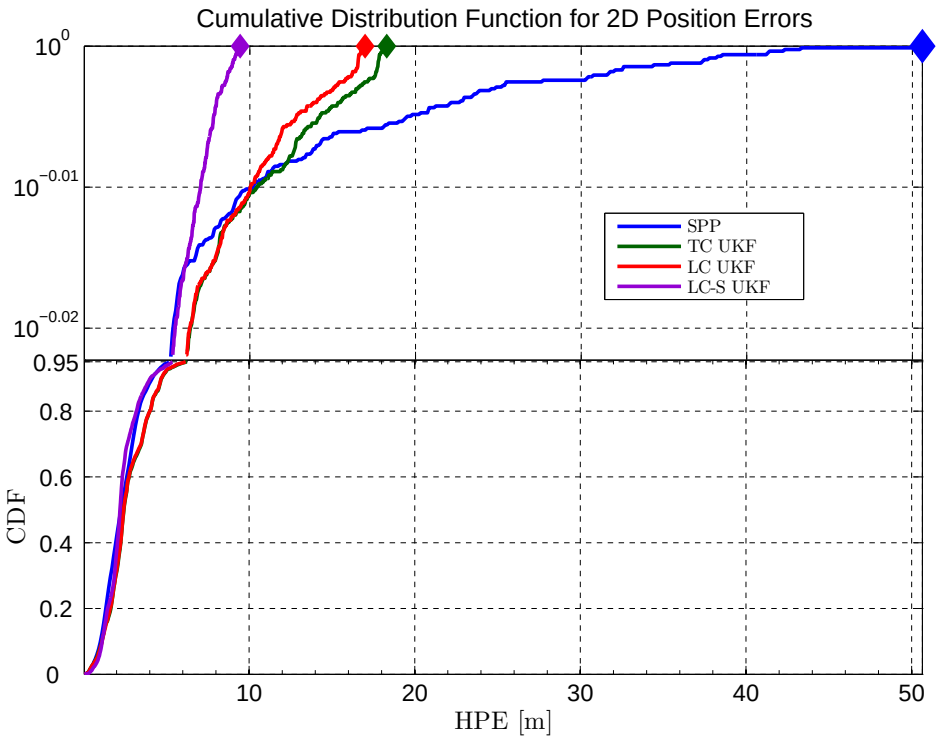


FIGURE 8.4: Cumulative distribution of HPE for SPP different implementations of Kalman filters.

cases a significant improvement in the maximum HPE value can be attributed to the generic RBE structure, where one relies not only on the available measurements, but also on the a priori assumed or, in the case of strapdown inertial mechanization, actually measured dynamics for the target. Note that almost no change can be seen for LC-GS UKF when compared to non-robust UKF schemes which is consistent with the performance of the robust weighted schemes in Table 7.7.

The positioning performance of the RBE methods during the bridge passage is shown in Fig. 8.5. As expected, due to inertial mechanization used in these approaches, the estimation results are far less sensitive to single GNSS positioning failures. Still, for strong GNSS position failures the trajectory is slightly deformed, although the deviation from the reference path is significantly smaller when compared to snapshot approaches and could be even further improved by fine tuning of the related filter parameters.

**Detail on the estimated trajectory from different KF**

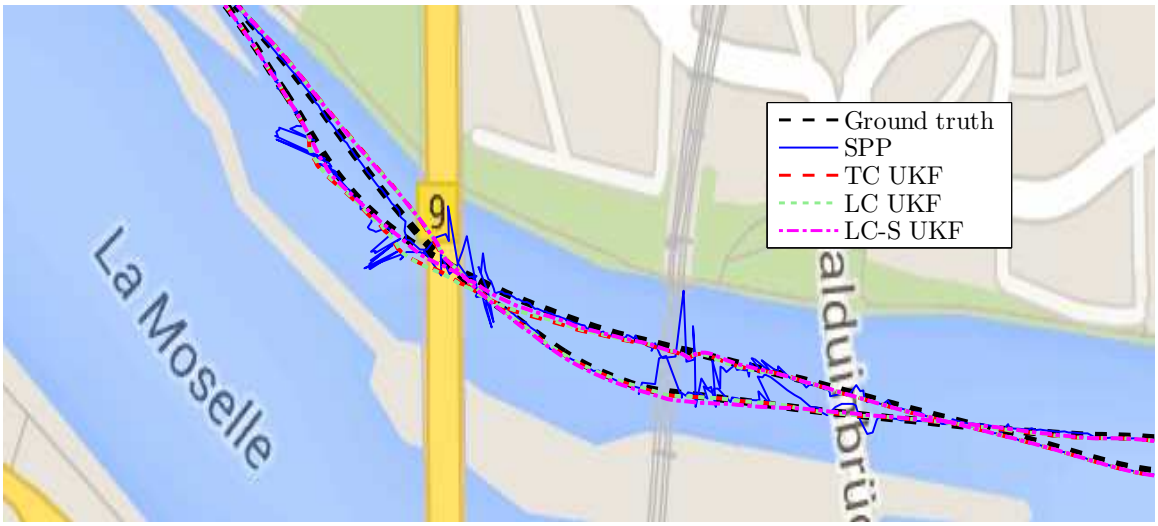


FIGURE 8.5: Positioning estimation of SPP and three configurations for UKF corresponding to the period in which the vessel passes under two bridges.

Chapter 9

# Conclusions and Future Work

The work has assessed an ability of the robust estimation schemes to improve the GNSS and combined IMU/GNSS positioning for challenging inland water scenarios with multiple GNSS outliers. The work had clearly demonstrated the superior performance of robust schemes for snapshot GNSS positioning and provided an extension of the methods for $C/N_0$ based weighting schemes. The proposed methods have been systematically evaluated both in terms of mean and maximum horizontal position errors and compared to those of modern subset consistency evaluation methods as well as RAIM-like techniques. An extension of the methods for snapshot velocity solution has been also suggested and several representative methods have been evaluated. An advantage of the proposed techniques for integrated navigation system has been demonstrated by designing a corresponding IMU/GNSS UKF.

As demonstrated in this work, the robust estimation constitutes an appropriate framework in order to reduce the largest position errors in navigation. Despite the proposed schemes are not able to completely handle the presence of several simultaneous faulty measurements, still having spare gross errors for the position solution, there is a clear improvement against classical SPP. Moreover, by integrating the robust techniques within a Kalman filter which fuses satellite and inertial-based navigation, this study has proven that the navigation solution is not only very accurate but also barely sensitive to the effect of multipath and NLOS effects on the GNSS signals.

While traditional RAIM methods are able to provide an upper bound of the position errors considering a given remaining integrity risk by means of so called protection levels, the robust methods are still lacking the equivalent solution integrity concept. Therefore, a new conceptual framework is needed for the GNSS integrity or quality control, when robust estimation is applied. Further work is planned on extension of the methods for MMM (multi-constellation, multi-frequency, multi-antenna). The latter extension is important as due to increased number of visible satellites, the probability of multiple simultaneous failures is also automatically increased. Applicability of the discussed techniques for phase measurements is also important for higher performance applications [69]. Also, further work is required on extending the methods to tightly-coupled KF using Robust KF or similar approaches and a more systematic analysis is definitely necessary including different application scenarios such as urban navigation, etc. Finally, the complementary characteristics of the robust methods can be exploited by having several of these robust methods running in parallel to provide a PVT solution. A decision matrix would then select the best solution among the different schemes to feed a KF, which is also receiving the information from the rest of the sensors: IMU, GNSS compass or other sensors (such as DVL, radar information or map of the environment). Kalman filter output would be the best Position Navigation, Timing and Integrity. Fig. 9.1 illustrates this system proposal as part of the future work.

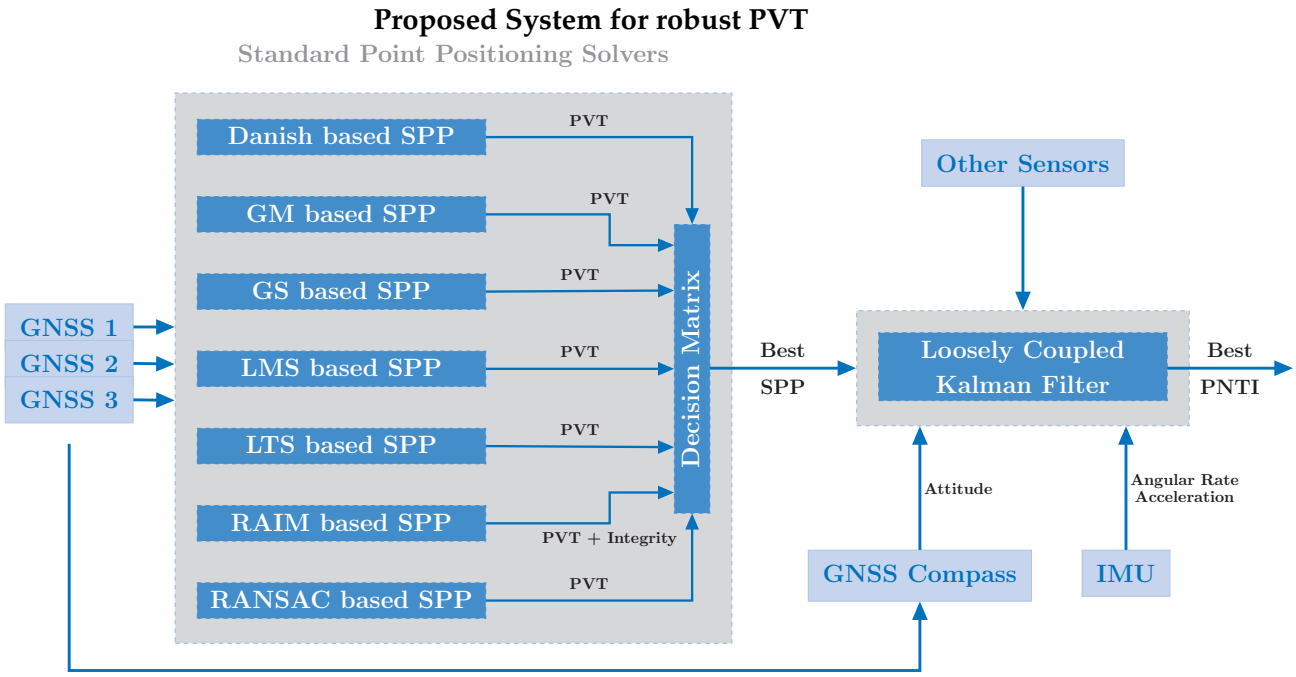


FIGURE 9.1: The SPP solver receive the GNSS signals from multiple constellation to obtain a PVT solution. The decision matrix is in charge to select the best solution, which is then fed to the KF. KF fuses the information of multiple sensors, apart from receiving the best solution among the robust methods, and gets the best solution for Positioning, Navigation, Timing and Integrity.

Appendix A

# Quaternions and Orientation Representation

A quaternion is a four dimensional hyper-complex number that is often used to represent the orientation of a rigid body or an associated coordinate frame in a 3D space. Quaternions were introduced in 1843 by Hamilton as a result of the search for higher dimensional generalization of the complex numbers. Soon after this, it was proven that quaternions can represent rotations and orientations in three dimensions and they are currently applied in a wide variety of areas such as computer graphics, robotics, navigation, molecular dynamics, etc.

Differently from Euler Angles, the quaternions are not subject to the phenomenon called "gimbal lock", which is an effect preventing the Euler angles to be used when the pitch angle approaches $\pm 90^{\circ}$. Yet another alternative attitude parametrization in form of rotation matrices results in a difficult re-normalization procedure and computational inefficiency (rotation matrix has 9 non-trivial terms). Unfortunately, the quaternions have different algebraic properties from conventional 4D vectors and have to be carefully considered when adopted for filter design.

## A.1 Quaternion Algebra

We will use $i, j$, and $k$ to represent the standard orthonormal basis for 3 dimensional space $\mathbb{R}^3$:

$$i = (1,\ 0,\ 0) \tag{A.1}$$
$$j = (0,\ 1,\ 0) \tag{A.2}$$
$$k = (0,\ 0,\ 1) \tag{A.3}$$

which have the following properties:

$$ij = k = -ji \tag{A.4}$$
$$jk = i = -kj \tag{A.5}$$
$$ki = j = -ik \tag{A.6}$$
$$i^2 = j^2 = k^2 = ijk \equiv -1 \tag{A.7}$$

A quaternion is represented is a 4-tuple of real numbers, $q \in \mathbb{R}^4$. It is formed by a scalar $q_0$ and a vector part $\vec{q} \in \mathbb{R}^3$ as:

$$q = (q_0,\ q_1,\ q_2,\ q_3) = q_0 + \vec{q} = q_0 + iq_1 + jq_2 + kq_3 \tag{A.8}$$

Next, we will present the basic quaternion arithmetic operations:

**Addition** The sum or difference of two quaternion $q,\ p$ is another quaternion:

$$q \pm p = (q_0 + p_0) + i\,(q_1 + p_1) + j\,(q_2 + p_2) + k\,(q_3 + p_3) \tag{A.9}$$

**Conjugate**

$$q^* = [\ q_0,\ -\vec{q}\ ] \tag{A.10}$$

**Norm**

$$|q| = N(q) = \sqrt{q^20 + q^21 + q^22 + q^23} \tag{A.11}$$

**Inverse**

$$q^{-1} = \frac{q^*}{|q|^2} = q^* \tag{A.12}$$

**Identity** When involving multiplication is $[1,\ (0,\ 0,\ 0)]$, and when involving addition/subtraction $[0,\ (0,\ 0,\ 0)]$

**Multiplication** The quaternion product is not commutative, i.e., $q \otimes p \neq p \otimes q$, except in the case that vector parts of the quaternion are parallel $\vec{q} \times \vec{p} = 0$

$$p \otimes q = \begin{bmatrix} q_0 & -q_1 & -q_2 & -q_3 \\ q_1 & q_0 & -q_3 & q_2 \\ q_2 & q_3 & q_0 & -q_1 \\ q_3 & -q_2 & q_1 & q_0 \end{bmatrix} \cdot \begin{bmatrix} p_0 \\ p_1 \\ p_2 \\ p_3 \end{bmatrix} \tag{A.13}$$

expressed with a different formulation:

$$p \otimes q = \begin{bmatrix} q_0 & -\vec{q}^T \\ \vec{q} & q_0\, I_{3\times3} - \lfloor \vec{q}\times \rfloor \end{bmatrix} \begin{bmatrix} p_0 \\ \vec{p} \end{bmatrix} \tag{A.14}$$

with $\lfloor \vec{q}\times \rfloor$ as the skew-symmetric matrix operator, defined as:

$$\lfloor \vec{q}\times \rfloor = \begin{bmatrix} 0 & -q_3 & q_2 \\ q_3 & 0 & -q_1 \\ -q_2 & q_1 & 0 \end{bmatrix} \tag{A.15}$$

## A.2 Quaternion Differential Equations

Being $q_t$ the orientation quaternion at time $t$, and $q_{t+\Delta t}$ the orientation quaternion at the next time sample $t + \Delta t$. The relation between said quaternions is given by:

$$q_{t+\Delta t} = \delta q \otimes q_t \tag{A.16}$$

where $\delta q$ defines the rotation performed from consecutive time frames $t$ to $t + \Delta t$. In case $\delta q$ defines a very small angle, we can use the small angle approximation as next:

$$\delta t = \begin{bmatrix} cos\,(\delta\theta/2) \\ \vec{u}\ sin\,(\delta\theta/2) \end{bmatrix} \approx \begin{bmatrix} 1 \\ \frac{\delta\theta}{2} \end{bmatrix} \tag{A.17}$$

Diving the angle of the rotation by the time elapsed $\Delta t$ in the limit, we get the angular rate:

$$\omega = \lim_{\Delta t \to 0} \frac{\delta\theta}{\Delta t} \tag{A.18}$$

The derivative of the quaternion is given by:

$$\dot{q} = \lim_{\Delta t \to 0} \frac{q_{t+\Delta t} - q_t}{\Delta t} = \lim_{\Delta t \to 0} \frac{\delta q \otimes q_t - q_t}{\Delta t} \tag{A.19}$$

Making use of the expression A.14, we can formulate the numerator of the previous limit as:

$$\delta q \otimes q_t - q_t = \begin{bmatrix} 1 & -\frac{1}{2}\delta\theta^T \\ \frac{1}{2}\delta\theta & I_{3\times 3} + \lfloor \frac{1}{2}\delta\theta \times \rfloor \end{bmatrix} \begin{bmatrix} q_0 \\ \vec{q} \end{bmatrix} - \begin{bmatrix} q_0 \\ \vec{q} \end{bmatrix} \tag{A.20}$$

$$\delta q \otimes q_t - q_t = \frac{1}{2} \begin{bmatrix} 0 & -\delta\theta^T \\ \Delta\theta & \lfloor \delta\theta \times \rfloor \end{bmatrix} \begin{bmatrix} q_0 \\ \vec{q} \end{bmatrix} \tag{A.21}$$

The limit definition of the derivative then becomes:

$$\dot{q} = \lim_{\Delta t \to 0} \frac{1}{\Delta t} \left( \frac{1}{2} \begin{bmatrix} 0 & -\delta\theta^T \\ \Delta\theta & \lfloor \delta\theta \times \rfloor \end{bmatrix} \begin{bmatrix} q_0 \\ \vec{q} \end{bmatrix} \right), \qquad \text{where } \omega = \frac{\delta\theta}{\Delta t} \tag{A.22}$$

$$\dot{q} = \frac{1}{2} \begin{bmatrix} 0 & -\omega^T \\ \omega & \lfloor \omega \times \rfloor \end{bmatrix} \begin{bmatrix} q_0 \\ \vec{q} \end{bmatrix}, \tag{A.23}$$

to finally obtain the expression:

$$\dot{q} = \frac{1}{2} \Omega(\omega)\ q(t) \tag{A.24}$$

with $\Omega(\omega)$ as the skew-symmetric matrix:

$$\Omega(\omega) = \begin{bmatrix} 0 & \omega_z & -\omega_y & \omega_x \\ -\omega_z & 0 & \omega_x & \omega_y \\ \omega_y & -\omega_x & 0 & \omega_z \\ -\omega_x & -\omega_y & -\omega_z & 0 \end{bmatrix} \tag{A.25}$$

### Quaternion integration

In a similar fashion, the integration of a quaternion requires solving the first order differential equation A.24:

$$\dot{q}(t) = \frac{1}{2} \Omega(\omega)\, q(t) \tag{A.26}$$

And the general solution to the above equation is given by:

$$q(t) = \Theta(t, t_k)\, q(t_k) \tag{A.27}$$

The governing equation for $\Theta(t_k, t_k)$ is found by differentiation and substitution:

$$\dot{q}(t) = \dot{\Theta}(t, t_k) q(t) \tag{A.28}$$

$$\frac{1}{2} \Omega(\omega)\, q(t) = \dot{\Theta}(t, t_k) q(t) \tag{A.29}$$

$$\frac{1}{2} \Omega(\omega)\ \Theta(t, t_k) q(t) = \dot{\Theta}(t, t_k) q(t_k) \tag{A.30}$$

$$\tag{A.31}$$

Eliminating the term $q(t_k)$, we can express $\dot{\Theta}(t, t_k)$ as:

$$\dot{\Theta}(t, t_k) = \frac{1}{2}\,\Omega\,(\omega)\;\;\Theta(t, t_k) \tag{A.32}$$

with the initial condition $\Theta(t, t_k) = I_{3\times 3}$. If we assume the angular rate $\omega$ to be invariant during the integration time $\Delta t = t_{k+1} - t_k$, then the matrix $\Omega$ does not depend on time as well.

$$\Theta(t_{k+1}, t_k) = \Theta(\Delta t) = \exp\left(\frac{1}{2}\,\Omega(\omega)\Delta t\right) \tag{A.33}$$

This matrix exponential can be rewritten using Taylor series expansion [1] in order to get the next expression:

$$q(t_{k+1}) = \begin{bmatrix} \cos\left(\frac{|\omega|}{2}\Delta t\right) \\ \frac{\omega}{|\omega|}\cdot \sin\left(\frac{|\omega|}{2}\Delta t\right) \end{bmatrix} \otimes q(t_k) \tag{A.34}$$

The above expression can cause numerical instability for very small values of the angular rate $\omega$, as its norm $|\omega|$ appears as denominator. This integration method is known as the *Zeroth Order Quaternion Integration*, due to the assumption of $\omega(t) = \omega$. In [64], we can find also the *First Order Quaternion Integrator*, in which $\omega$ is assumed to change linearly within time.

## A.3 Quaternion Relationship to Rotations

In the 3-dimensional space, any rotation or sequence of rotations from the coordinate frame $A$ to another $B$ can be expressed as a single rotation $\theta$ about the axis $\vec{u}$. Unit quaternion can expressed said rotation as next:

$$q_A^B = \begin{bmatrix} \cos\left(\frac{\theta}{2}\right) \\ \vec{u}\sin\left(\frac{\theta}{2}\right) \end{bmatrix} \tag{A.35}$$

In order to be valid, a orientation quaternion has to have a unity norm. Either way, there would be an infinite number of quaternions expressing the same rotation (by multiplying the quaternion by a scalar). However, as multiplying a quaternion by $-1$ we still have a valid unit quaternion, a common assumption is having a positive value as scalar part of the quaternion in order to avoid ambiguity. Note that if the rotation axis and the angle are defined in the opposite frame (B instead of A), the quaternion has to be replaced by its conjugate, meaning:

$$q_A^B = \left(q_B^A\right)^* \tag{A.36}$$

It is possible to change the coordinate system of a rotation using the conjugation operation of a quaternion:

$$q \otimes p \otimes q = q \otimes (p_0 + \vec{p}) \otimes q^{-1} = q \otimes p_0 \otimes q^{-1} + q \otimes \vec{p} \otimes q^{-1} \tag{A.37}$$

$$p_0\; q \otimes q^{-1} + q \otimes \vec{p} \otimes q^{-1} = p_0 + q \otimes \vec{p} \otimes q^{-1} \tag{A.38}$$

Notive that, while the scalar part remains unchanged, the vector part is rotated. This way, the angle of the quaternion has not changed but the axis has been rotated. This property has been widely exploited in navigation systems: sensors attached to the target provide their measurements into the body frame, while the user is interested in having said measurements in the inertial frame. For example, let $\vec{a}^{\,b}$ be the acceleration provided by the accelerometer

[1] This expasion is shown and further explained in [64]

in the body frame:

$$\vec{a}^{\,b} = \begin{bmatrix} a_x \\ a_y \\ a_z \end{bmatrix} \tag{A.39}$$

The corresponding vector with the acceleration in the inertial frame $\vec{a}^{\,i}$ is estimated as next:

$$\begin{bmatrix} 0 \\ \vec{a}^{\,i} \end{bmatrix} = q \otimes \begin{bmatrix} 0 \\ \vec{a}^{\,b} \end{bmatrix} \otimes q^{-1} \tag{A.40}$$

It is widely well known the procedure to rotate one vector from one frame to another by using the rotation matrix:

$$\vec{v}^{\,i} = R_b^i(q)\ \vec{v}^{\,b} \tag{A.41}$$

In [46] it has been shown the relationship between quaternion and rotation matrix:

$$R_b^i(q) = \left(q_0^2 - \vec{q}^{\,T}\vec{q}\right) I_{3\times 3} + 2\left(\vec{q}\,\vec{q}^{\,T} - q_0 \lfloor \vec{q}\times \rfloor\right) \tag{A.42}$$

# Bibliography


[1] D. F. Andrews and F. R. Hampel. *Robust estimates of location: survey and advances*. Princeton University Press, 2015.

[2] M. Bevis et al. "GPS meteorology: Mapping zenith wet delays onto precipitable water". In: *Journal of applied meteorology* 33.3 (1994), pp. 379–386.

[3] H. D. Black. "A passive system for determining the attitude of a satellite". In: *AIAA Journal* 2.7 (1964), pp. 1350–1351.

[4] G. Cai, B. M. Chen, and T. H. Lee. *Unmanned rotorcraft systems*. Springer Science & Business Media, 2011.

[5] G. Castaldo et al. "P-RANSAC: an Integrity monitoring approach for GNSS signal degraded scenario". In: *International Journal of Navigation and Observation* 2014 (2014).

[6] O. H. Christophe Croux Peter J. Rousseeuw. "Generalized S-Estimators". In: *Journal of the American Statistical Association* 89.428 (1994), pp. 1271–1281. ISSN: 01621459. URL: http://www.jstor.org/stable/2290990.

[7] DLR. *Nautical Systems Department Institute of Communication and Navigation, DLR*. URL: http://www.dlr.de/kn/en/desktopdefault.aspx/tabid-2204/ (visited on 01/27/2016).

[8] F. Y. Edgeworth. "On observations relating to several quantities". In: *Hermathena* 6.13 (1887), pp. 279–285.

[9] N. El-Sheimy, E.-H. Shin, and X. Niu. "Kalman Filter Face-Off: Extended vs. Unscented Kalman Filters for Integrated GPS and MEMS Inertial". In: *Inside GNSS* (2006).

[10] M. A. Fischler and R. C. Bolles. "Random sample consensus: a paradigm for model fitting with applications to image analysis and automated cartography". In: *Communications of the ACM* 24.6 (1981), pp. 381–395.

[11] *FleetMon*. URL: https://www.fleetmon.com/vessels/baltic-taucher-ii_9096387_52487/photos/1053575/ (visited on 01/27/2016).

[12] T. Ford et al. *GPS/MEMS Inertial Integration Methodology and Results*. Tech. rep. NovaTel, 2004.

[13] D. Fox, W. Burgard, and S. Thrun. *Probabilistic Robotics. Intelligent Robotics and Autonomous Agents*. 2005.

[14] P. D. Groves. *Principles of GNSS, inertial, and multisensor integrated navigation systems*. Artech house, 2013.

[15] P. D. Groves and Z. Jiang. "Height Aiding, $C/N_0$ weighting and consistency checking for GNSS NLOS and multipath mitigation in urban areas". In: *The Journal of Navigation* 66.653-669 (2013).

[16] P. D. Groves et al. “A portfolio approach to NLOS and multipath mitigation in dense urban areas”. In: (2013).

[17] A Heßelbarth et al. “Paper 22–Reliable Height Determination for an Efficient Bridge Collision Warning System on Inland Waterways”. In: ().

[18] A. Heßelbarth et al. “Reliable Height Determination for an Efficient Bridge Collision Warning System on Inland Waterways”. In: *Smart Rivers Conference*. Ed. by W. A. for Waterborne Transport Infrastructure. Buenos Aires, Argentina, 2015.

[19] B. Hofmann-Wellenhof, H. Lichtenegger, and E. Wasle. *GNSS–global navigation satellite systems: GPS, GLONASS, Galileo, and more*. Springer Science & Business Media, 2007.

[20] P. W. Holland and R. E. Welsch. “Robust regression using iteratively reweighted least-squares”. In: *Communications in Statistics-theory and Methods* 6.9 (1977), pp. 813–827.

[21] J. Humpherys, P. Redd, and J. West. “A fresh look at the Kalman filter”. In: *SIAM review* 54.4 (2012), pp. 801–823.

[22] Z. Jiang and P. D. Groves. “GNSS NLOS and multipath error mitigation using advanced multi-constellation consistency checking with height aiding”. In: (2012).

[23] S. J. Julier and J. K. Uhlmann. “New extension of the Kalman filter to nonlinear systems”. In: *AeroSense'97*. International Society for Optics and Photonics. 1997, pp. 182–193.

[24] E. D. Kaplan, J. Leva, and M. Pavloff. “Fundamentals of satellite navigation”. In: *Understanding GPS- Principles and applications(A 96-41027 11-17), Norwood, MA, Artech House, 1996*, (1996), pp. 15–57.

[25] R. J. Kelly. “The linear model, RNP, and the near-optimum fault detection and exclusion algorithm”. In: *Global positioning system* 5 (1998), pp. 227–259.

[26] N. L. Knight and J. Wang. “A Comparison of Outlier Detection Procedures and Robust Estimation Methods in GPS Positioning”. In: *Journal of Navigation* 62 (04 Oct. 2009), pp. 699–709. ISSN: 1469-7785.

[27] N. L. Knight and J. Wang. “A comparison of outlier detection procedures and robust estimation methods in GPS positioning”. In: *Journal of Navigation* 62.04 (2009), pp. 699–709.

[28] K.-R. Koch. *Parameter estimation and hypothesis testing in linear models*. Springer Science & Business Media, 1999.

[29] E. Kraft. “A quaternion-based unscented Kalman filter for orientation tracking”. In: *Information Fusion, 2003. Proceedings of the Sixth International Conference of*. Vol. 1. 2003, pp. 47–54. DOI: 10.1109/ICIF.2003.177425.

[30] T. Krarup, J Juhl, and K Kubik. “Gotterdammerung over least squares adjustment”. In: *International archives of photogrammetry* (1980), pp. 369–378.

[31] H. Kuusniemi. *User-level reliability and quality monitoring in satellite-based personal navigation*. 2005.

[32] H. Kuusniemi et al. “User-level reliability monitoring in urban personal satellite-navigation”. In: *Aerospace and Electronic Systems, IEEE Transactions on* 43.4 (2007), pp. 1305–1318.

[33] L. Lança, M. Romanovas, and R. Ziebold. “INTEGRITY MONITORING IN SNAPSHOT AND RECURSIVE ESTIMATION ALGORITHMS FOR MARITIME APPLICATIONS”. In: ().

[34] Y. C. Lee and D. G. O'Laughlin. “A Performance Analysis of a Tightly Coupled GPS/Inertial System for Two Integrity Monitoring Method”. In: *Navigation* 47.3 (2000), pp. 175–189. ISSN: 2161-4296.

[35] C. L. Mallows. “On some topics in robustness”. In: *Unpublished memorandum, Bell Telephone Laboratories, Murray Hill, NJ* (1975).

[36] F. L. Markley and D. Mortari. “How to estimate attitude from vector observations”. In: *Proceedings of the AAS/AIAA Astrodynamics Specialist Conference*. Vol. 103. 3. 1999, pp. 1979–1996.

[37] L Markley. “Attitude determination using two vector measurements”. In: *NASA CONFERENCE PUBLICATION*. NASA. 1999, pp. 39–52.

[38] D. L. Massart et al. “Least median of squares: a robust method for outlier and model error detection in regression and calibration”. In: *Analytica Chimica Acta* 187 (1986), pp. 171 –179.

[39] J. McMillan. “MINS-B II: a marine integrated navigation system”. In: *Position Location and Navigation Symposium, 1988. Record. Navigation into the 21st Century. IEEE PLANS '88., IEEE*. 1988, pp. 499–508. DOI: 10.1109/PLANS.1988.195525.

[40] L. Meski. “Shipping accidents in the Baltic Sea in 2012”. In:

[41] T. Moore et al. “The Potential Impact of GNSS/INS Integration on Maritime Navigation”. In: *The Journal of Navigation* 61 (2008), 221–237.

[42] P. Najman and T. Kos. “Performance Analysis of Empirical Ionosphere Models by Comparison with CODE Vertical TEC Maps”. In: (2014).

[43] H. Pesonen. “Robust estimation techniques for GNSS positioning”. In: *Proceedings of NAV07-The Navigation Conference and Exhibition, 31.10.-1.11. 2007, London, England*. 2007.

[44] M. Petovello. *GNSS solutions: Carrier phase and its measurements for GNSS. InsideGNSS, July/August 2010*.

[45] A. Rietdorf, C. Daub, and P. Loef. “Precise Positioning in Real-Time using Navigation Satellites and Telecommunication”. In: *Proceedings of The 3rd Workshop on Positioning and Communication (WPNC'06)*. 2006.

[46] M Romanovas. *Methods for Pedestrian Localization and Motion Tracking Using Inertial MEMS Sensors [Ph. D. thesis]*. 2016.

[47] M. Romanovas, R. Ziebold, and L. Lanca. “A method for IMU/GNSS/Doppler Velocity Log integration in marine applications”. In: *Navigation World Congress (IAIN), 2015 International Association of Institutes of*. IEEE. 2015, pp. 1–8.

[48] M. Romanovas et al. “A study on indoor pedestrian localization algorithms with foot-mounted sensors”. In: *Indoor Positioning and Indoor Navigation (IPIN), 2012 International Conference on*. IEEE. 2012, pp. 1–10.

[49] *Rostock Port Website*. URL: http://www.rostock-port.de/en/shipping/combined-cargo/statistics.html (visited on 01/27/2016).

[50] P. Rousseeuw and V. Yohai. “Robust regression by means of S-estimators”. In: *Robust and nonlinear time series analysis*. Springer, 1984, pp. 256–272.

[51] P. J. Rousseeuw. “Least median of squares regression”. In: *Journal of the American statistical association* 79.388 (1984), pp. 871–880.

[52] P. J. Rousseeuw and C. Croux. “Alternatives to the median absolute deviation”. In: *Journal of the American Statistical association* 88.424 (1993), pp. 1273–1283.

[53] P. J. Rousseeuw and A. M. Leroy. *Robust regression and outlier detection*. Vol. 589. John Wiley & Sons, 2005.

[54] J Sanz, J Juan, and M Hernández-Pajares. *GNSS Data Processing, Vol. I: Fundamentals and Algorithms. Noordwijk, the Netherlands: ESA Communications*. Tech. rep. ESTEC TM-23/1, 2013.

[55] G. Schroth et al. “Enhancements of the Range Consensus Algorithm (RANCO)”. In: *Proceedings of the 21st International Technical Meeting of the Satellite Division of The Institute of Navigation (ION GNSS 2008)*. Savannah, GA, 2008, pp. 93–103.

[56] G. Schroth et al. “Enhancements of the range consensus algorithm (RANCO)”. In: *ION GNSS 2008* (2008), pp. 16–19.

[57] G. Schroth et al. “Failure Detection and Exclusion via Range Consensus”. In: *European Navigation Conference 2008 (ENC GNSS 2008)*. Toulouse, France, 2008.

[58] M. D. Shuster. “The quest for better attitudes”. In: *The Journal of the Astronautical Sciences* 54.3-4 (2006), pp. 657–683.

[59] M. D. Shuster and S. Oh. “Three-axis attitude determination from vector observations”. In: *Journal of Guidance, Control, and Dynamics* 4.1 (1981), pp. 70–77.

[60] Y Susanti, H Pratiwi, et al. “M ESTIMATION, S ESTIMATION, AND MM ESTIMATION IN ROBUST REGRESSION”. In: *International Journal of Pure and Applied Mathematics* 91.3 (2014), pp. 349–360.

[61] Y. Susanti, S. Pratiwi H. andSulistijowati, and T. Liana. “M eestimation S estimation, and MM estimation in robust regression”. In: *International Journal of Pure and Applied Mathematics* 91.3 (2014), pp. 349–360.

[62] T. Takasu and A. Yasuda. “Development of the low-cost RTK-GPS receiver with an open source program package RTKLIB”. In: *international symposium on GPS/GNSS*. International Convention Centre Jeju, Korea. 2009, pp. 4–6.

[63] G. A. Terejanu. “Unscented Kalman filter tutorial”. In: *University at Buffalo, Buffalo* (2011).

[64] N. Trawny and S. I. Roumeliotis. “Indirect Kalman filter for 3D attitude estimation”. In: *University of Minnesota, Dept. of Comp. Sci. & Eng., Tech. Rep* 2 (2005).

[65] P. Verboon. *Majorization with iteratively reweighted least squares: a general approach to optimize a class of resistant loss functions*. University of Leiden, 1990.

[66] G. Wahba. “A least squares estimate of satellite attitude”. In: *SIAM review* 7.3 (1965), pp. 409–409.

[67] J. Wang, M. P. Stewart, and M. Tsakiri. “Stochastic modeling for static GPS baseline data processing”. In: *Journal of Surveying Engineering* 124.4 (1998), pp. 171–181.

[68] J. Wang and J. Wang. “Mitigating the Effect of Multiple Outliers on GNSS Navigation with M-Estimation Schemes”. In: *International Global Navigation Satellite Systems Society IGNSS Symposium*. The University of New South Wales, Sydney, Australia, 2007.

[69] A. Wieser and F. K. Brunner. “Short Static GPS Sessions: Robust Estimation Results”. English. In: *GPS Solutions* 5.3 (2002), pp. 70–79. ISSN: 1080-5370. DOI: 10.1007/PL00012901. URL: http://dx.doi.org/10.1007/PL00012901.

[70] R. Ziebold, M. Romanovas, and L Lanca. “Activities in Navigation. Marine Navigation and Safety of Sea Transportation”. In: ed. by A. Weintrit. CRC Press, 2015. Chap. Evaluation of Low Cost Tactical Grade MEMS IMU for Maritime Navigation, pp. 237–246.

[71] M. Zuliani. “RANSAC for Dummies”. In: *Vision Research Lab, University of California, Santa Barbara* (2009).